Universität Zürich[UZH]

Geographisches Institut

Geomorphological mapping in high alpine environments: a case study of mass movement processes at the margins of Findel Glacier, Swiss Alps

ESS 511 Master's Thesis

Author: Michael Alfred Czaderski-Forchmann, 21-726-047

Supervised by: Dr. Isabelle Gärtner-Roer

Faculty representative: Prof. Dr. Andreas Vieli

24.06.2026

Abstract

Alpine glaciers are retreating at an accelerating rate, exposing new slopes and bedrock to atmospheric and hydrological processes. This activates previously stable sediment deposition and erodes glacial landforms. In these paraglacial environments, mass movements are frequently involved in the processes and actively reshape these alpine valleys. However, the rate and type of mass movements remain difficult to predict. This thesis investigates mass movement dynamics at the margins of Findel glacier, Valais, Switzerland, using high-resolution airborne digital surface models (DSMs) and digital ortho photos (DOP) acquired between 2012 and 2024 to quantify changes. Two slopes were selected for an in-depth analysis with geomorphology mapping, elevation changes and feature tracking to detect changes and underlying processes. The findings showed that in addition to the massive thinning of the glacier at the margins of the glacier, many mass movements were observed. At the Innere Rimpfischwäng slope a potential deep-seated gravitational slope deformation showed episodic acceleration phases. The second investigated slope was located further down the glacier and exhibited a rockslide that originated in a periglacial environment and, during the study period, reached the valley floor and buried part of the glacier. Furthermore, a scarp in the slope head could led to the collapse of part of the moraine. These two slopes show that, although they are spatially close to each other, very different mass movements can be observed, and they are not related to each other. Therefore, this study demonstrates that not a single driver was dominant in the release of the mass movements, but rather that mass movement processes in high mountain environments are driven by a complex interplay of factors that are highly site-specific. It is unlikely that glacier retreat is the only destabilization factor, as the presence of geological structures and permafrost can prepare slope instabilities.

This study demonstrated that multi-temporal remote sensing data can successfully be used to analyse geomorphic features in remote alpine regions. It underlines the benefit of the continuous effort to monitor the evolution of the landscape to prevent natural hazards in the changing environment of the alpine forefield under climate change.

Acknowledgments

First, I would like to thank my master thesis supervisor Dr. Isabelle Gärtner-Roer for her advice, support and helpful discussions in the creation. Additionally, Prof. Dr. Andreas Vieli added valuable feedback for this work. I also want to thank Ataullah Raza Khan for supporting me in the data homogenization and pre-processing. Furthermore, Elias Hodel and the VAW shared their data of the Findel Glacier and made this thesis possible.

My dear colleagues Antonia, Kathrin, Shelby, and Sonja helped with mental support and with their opinions about visualization and questions about my thesis and made the writing and working of this thesis more enjoyable.

A special thanks goes to my family and my fiance Zoé-Naida, who supported me throughout the whole thesis. Without their support this thesis wouldn't be possible.

Contents

List of figures vi

List of tables xiii

List of abbreviations xiv

1 Introduction 1

1.1 Research questions . . . 2

2 Theoretical background 3

2.1 Geomorphological environments . . . 3

2.1.1 Glacial environments . . . 5

2.1.2 Periglacial environments . . . 5

2.1.3 Paraglacial environments . . . 8

2.2 Mass movements . . . 8

2.2.1 Solifluction . . . 10

2.2.2 Debris flow . . . 11

2.2.3 Rock avalanche . . . 12

2.2.4 Rockfalls . . . 13

2.2.5 Rockslides . . . 14

2.2.6 Gravitational slope deformations . . . 15

2.3 Slope controlling variables . . . 18

2.3.1 External factors . . . 18

2.3.2 Interal factors . . . 20

3 Study site 24

3.1 Findel valley and glacier . . . 24

3.2 Slopes . . . 26

3.2.1 Innere Rimpfischwäng slope . . . 28

3.2.2 Tripfen slope . . . 30

3.2.3 Geology at study slopes . . . 31

4 Methods **34**

4.1 Data. . . . 34

4.2 Pre-processing and uncertainty . . . 36

4.2.1 Pre-processing . . . 36

4.2.2 Co-registration . . . 38

4.2.3 Uncertainties. . . . 39

4.3 Spatial analysis . . . 43

4.3.1 Geomorphological mapping . . . 44

4.3.2 DEM of difference . . . 46

4.3.3 DEM transects . . . 47

4.3.4 Point tracking . . . 47

5 Results **49**

5.1 Geomorphological overview . . . 49

5.2 Findel Glacier . . . 52

5.3 Innere Rimpfischwäng slope . . . 55

5.3.1 Spatial analysis . . . 55

5.3.2 Temporal analysis . . . 57

5.4 Tripfen slope . . . 64

5.4.1 Spatial analysis . . . 64

5.4.2 Temporal changes. . . . 68

6 Discussion **74**

6.1 Quantifying changes in high alpine environments . . . 74

6.1.1 Subsurface ice . . . 74

6.1.2 Hazard potential . . . 76

6.1.3 Mass movement dynamics . . . 76

6.2 Drivers of slope instability . . . 79

6.2.1 Geology . . . 79

6.2.2 Permafrost thawing . . . 81

6.2.3 Glacier debuttressing . . . 83

6.2.4 Meteorological conditions 85
6.2.5 Classification of mass movements 89
6.3 Limitations and outlook 92

7 Conclusion **94**

References **96**

Appendix **107**

Personal declaration **116**

List of Figures

2.1 Sketch showing the geomorphological evolution of the glacier forefield and its margins after the glacier's retreat. Depending on the retreating stage, different processes act on the landscape (Cossart and Fort, 2008) 4

2.2 The temporal evolution of moraines depending on glacier advance and retreat phases (Lukas et al., 2012) 6

2.3 Periglacial concept by French (2017) showing the distribution of permafrost and snow and Ice 7

2.4 Visualisation of the 6 different mass movement as defined by Varnes (1978) (Shanmugam and Wang, 2015) 9

2.5 Solifluction lobe bound by vegetation at Meretschialp, Valais, Switzerland (Dikau et al., 2019).. 10

2.6 A debris flow at the lower section of Illgraben(Image: WSL) (Michael Keller, 2021). 11

2.7 The bulging Birch glacier covered a rock avalanche before the glacier collapsed under the load of the rock masses (Image: KEYSTONE / Jean-Christophe Bott) on 23 May 2025 (Florian Meyer, 2025) 12

2.8 Rockfall at Mel de la Niva captured by Ludwig Haas, canton Valais. (Institut für Schnee- und Lawinenforschung SLF, 2025) 13

2.9 A rotational slide involving Cretaceous shale, overlain by sandstone. Liard Plateau, Canada (Photo by O. Hungr)(Hungr et al., 2014) 14

2.10 "Examples of frequently occurring modes of DSGSDs from various types of landscapes. A. Ridge-top graben affecting granodiorites of the Salatín Mt. (Tatra Mts., Slovakia). B. Asymmetric sagging (ridge displacement to the left) affecting SE part of the Salatín ridge (Tatra Mts, Slovakia). Cases A and B are examples of DSGSDs situated in mountains that were heavily glaciated during the Late Pleistocene (final deglaciation about 11 ka; Makos et al., 2014) C. Nearly 3 km long double ridge on non-glaciated flysch terrain (Mt. Barigazzo, Northern Apennines, Italy; photo courtesy: G. Bertolini). D. Series of uphill-facing scarps at the Gilette Pass (Alaska, USA) produced by the 2002 Denali Fault earthquake. (Photo courtesy: U.S. Geological Survey/photo by Peter Haeussle.)" (Pánek and Klimeš, 2016) 16

2.11 Borehole measurement which showed movement pattern of slope and the rupture surface (Yamamoto et al., 2023) 17

2.12 “Rock slope with potential slope failure being buttressed. A toe-of-slope buttress provides external support to a slope by adding a vertical load surcharge to the toe (A) and by providing additional sliding (shear) resistance (B). The buttress counterbalances the forces driving landslide displacement“ (McColl et al., 2010) 18

2.13 ”Thermophysical model of permafrost of a periglacial environment and associated terms used to describe the ground temperature relative to 0 °C, after van Everdigen (1998), with changes” (Dobinski, 2011) 21

2.14 Factor of safety shows the evaluation of slope on time scale and processes which occur in this time (Mihail E. Popescu, 2002) 22

2.15 Geological Strength Index (GSI) chart, based on block size and joint condition (Hoek et al., 2000) 23

3.1 Findel Glacier comparison 1990–2025 24

3.2 Findel Glacier cumulative length changes over the last century measured by GLAMOS (2026) and published by WGMS (2025) 25

3.3 Findel Glacier mass balance (glaciological method) over the last 20 years measured by GLAMOS (2026) and published by WGMS (2025). 25

3.4 Elevation changes (DoD 2012–2021) across the Findel Glacier and its margins. Negative values (red) indicate surface lowering dominated by glacier thinning, reaching up to -87 m on the glacier tongue. Positive values (blue) reflect local accumulation. The two study slopes (Tripfen and Innere Rimpfischwäng) are labelled.. 27

3.5 Aerial view of the Innere Rimpfischwäng slope in late September 2025 (field observation). 28

3.6 Innere Rimpfischwäng slope extent and scarp at the slope head. Spatial extent of the Innere Rimpfischwäng (IR) slope (green polygon) and scarp (dark green). The scarp marks the upper boundary of the unstable slope body.. . . . 29

3.7 Tripfen slope in 2025 from field observation (Michael Czaderski). The rockslide (green) migrated over the years (breached the moraine and reached the valley floor). The Tripfen area is marked in violet. 30

3.8 Tripfen slope extent in 2012 (purple), limited by the steep rock wall at the top and a buffer around the rockslide body (green/yellowish) at the bottom. 31

3.9 Geological overview of the Findel Glacier forefield and adjacent slopes, based on the Geological Atlas of Switzerland (Bearth, 1953). The two study slopes are the Innere Rimpfischwäng (IR) slope (light green) and the Tripfen slope (violet). The bedrock lithologies are eclogite-amphibolite (dark green) and serpentinite (olive-brown) and schist (gneiss, brown). Quaternary moraine material (beige) covers large parts of the margins of the glacier. Rockfalls, cones and debris accumulations are widespread along the valley flanks. Profile 1 (blue line) indicates the cross-sectional transect used for structural analysis (fig. 6.2). 32

3.10 Detailed geological overview of the two study slopes overlaid on the Geological Atlas of Switzerland (GA25, Swisstopo, scale 1:12 500). The two main bedrock lithologies are eclogite-amphibolite (dark green) and serpentinite (olive-brown). Quaternary moraine material (beige) covers the slope of the Tripfen slope where the rockslide originated. 33

4.1 Pre-processing workflow for aerial remote sensing data for this thesis. Highlighted in green are steps, which stored the files, processes performed in ArcGIS are red, in orange are all the used shapefiles, which were needed as input and the code used to execute operations in ArcGIS is shown in yellow (created in Miro (2025)). 37

4.2 ”Top: 2-D scheme of elevation differences induced by a DEM shift. Bottom: The scatter of elevation differences between 2 DEMs showing the relationship between the vertical deviations normalised by the slope tangent (y-axis) and terrain aspect (x-axis).” (Nuth and Kääb, 2011) 38

4.3 Uncertainty in digital elevation models (DEM). These can be defined as systematic errors and random errors and have various reasons (Hugonnet et al., 2022). 39

4.4 Slope mask showing the slope angle of each pixel. Only the first class (yellow) of the slope angle is referenced as flat terrain and therefore can be used for stable terrain. In blue are the chosen stable terrain polygons. The glacier domain was excluded. 41

4.5 Systematic and random error and the total RMSE over the time series for DOP Images. Errors and total RMSE decrease towards newer images. 43

4.6 Example of geomorphological mapping of the foreland of Skálafellsjökull, from Chandler et al. (2018). A) shows the different input products that can be used for mapping; B) the resulting geomorphological map; C) the application of the map for calculating crest-to-crest moraine spacing as a proxy for ice-margin retreat rates.. 44

4.7 Morphological classification of debris slopes by Rapp (1960); Church et al. (1979). Depending on the water available, the morphology of the slope and the deposition of rocks change, as well as the presence or absence of avalanches. 46

4.8 Transects 1–23 along the glacier and slopes of interest, spanning a total length of approximately 1400 meters. 47

4.9 Example of a tracked boulder over the study period. Each year, the locations of the boulders were extracted by marking the same point on the boulder. . . . 48

5.1 Geomorphological process domain map of the Findel Glacier forefield and adjacent slopes. Process domains, specific geomorphological features, and the glaciological and hydrological networks are mapped across the study area. 49

5.2 Geomorphological process domain at IR slope. Specific features of the slope are rockfall cones and a block field. 50

5.3 Geomorphological process domain at Tripfen slope. Specific features of the slope are the rockfall cones and the rockslide.. 51

5.4 Glacier tongue evolution over the study period at the Findel Glacier.. 52

5.5 Transect shows glacier tongue thickness evolution over the study period at Tripfen slope. 53

5.6 Transect show glacier thickness evolution over the study period at IR slope. . . 54

5.7 First identification of a main scarp at the IR slope. 55

5.8 A: DoD 2012-2016, B: DoD 2016-2020, C: DoD 2020-2024, D: Volume changes in the slope and the moraine below the slope.. 56

5.9 Location of each boulder at the IR slope. Outside scarp boulders did not show significant movement during the study period. Slope toe boulders could not be tracked due to frequent rockfall events. 57

5.10 Velocity of the different topographic zones from 2012–2024. 58

5.11 Velocities per category and grouped in low and high activity phases. Boulders outside the scrap and the slope body were used to validate movements of the slope body (compare fig. 5.9). 58

5.12 Velocity vector showing the direction of the movement per year. 59

5.13 DoD (DEM of Difference) 2017–2019 of the Innere Rimpfischwäng (IR) slope. Reddish colours indicate surface lowering, bluish colours indicate surface elevation gain [m]. The green line delineates the main scarp of the slope. 60

5.14 DoD (DEM of Difference) 2019–2020 of the Innere Rimpfischwäng (IR) slope. Reddish colours indicate surface lowering; bluish colours indicate surface elevation gain [m]. The green line delineates the main scarp of the slope. 61

5.15 DoD (DEM of Difference) 2020–2021 of the Innere Rimpfischwäng (IR) slope. Reddish colours indicate surface lowering; bluish colours indicate surface elevation gain [m]. The green line delineates the main scarp of the slope. 62

5.16 DoD (DEM of Difference) 2023–2024 of the Innere Rimpfischwäng (IR) slope. Reddish colours indicate surface lowering; bluish colours indicate surface elevation gain [m]. The green line delineates the main scarp of the slope. 63

5.17 Camera photo of the rockslide body in September 2025. Remnant glacier ice of the Findel Glacier is visible at right side of the rockslide body. 64

5.18 A: Rockslide Body in 2012, B: Rockslide body in 2024, C: DoD of the Rockslide Body. D: Aerial view of the Rockslide area and the exposed bedrock. 65

5.19 Different types of material of the rockslide body in the year 2012. 66

5.20 First identification of a scarp at the Tripfen slope in 2024. 67

5.21 DoD (DEM of Difference) 2017–2019 of the Tripfen slope. Reddish colours indicate surface lowering; bluish colours indicate surface elevation gain [m]. Rockslide extent of the year 2024. 68

5.22 Rockslide body over the study period shown in different colors. 69

5.23 Selection of boulders at the Tripfen slope. The boulder represents the movement pattern of the five topographic features. 70

5.24 Velocity of picked boulder in the diffrent categories shown in fig. 5.23. 71

5.25 Overview of all transects at the Tripfen slope and profile 2, where the moraine collapsed in the year 2024 is visible. 72

5.26 Trajectories and displacement vectors of the boulders at Tripfen slope. Color sheme show more dark red color for higher velocities. 73

6.1 Control points for Tripfen and Innere Rimpfischwäng slopes. 78

6.2 Geological cross-section along profile 1 as indicated in fig. 3.9. The profile extends from WNW (Oberrothorn) to ESE (Schwarzberggletscher), crossing the Ophiolith zone Zermatt–Saas–Fee. Red lines highlight the lithological transition zones relevant for the IR and Tripfen slopes. This zone is also known as the Zermatt-Saas ophiolite zone (ZSZ). Figure adapted from Bearth (1953). . . . 80

6.3 Serpentinite looks more disintegrated (red) than the eclogite (orange) rock formation 80

6.4 BAFU Permafrost distribution map created by Gruber, S et al. (2006). The map illustrates possible ground conditions at the study slopes (open available from BAFU (2011)). 81
6.5 SLF Permafrost distribution map for ice-rich and ice-poor permafrost map created by Kenner et al. (2019). The map illustrates possible ground conditions at the study slopes (open available from Robert Kenner (2019). 82
6.6 Evolution of glacier margins between 1864 and 2020 for transects 13 and 17 showing the lateral support loss. 84
6.7 A: IR mean slope movement, B: Tripfen rockslide movement, C: Mean temperature over study period and WMO climate reference (1996-2020), D: Mean precipitation at Findelbach station over the study period and WMO climate reference (1990-2020) 86
6.8 A: IR mean slope movement, B: Tripfen rockslide movement, C: Mean summer temperature (JJA) over study period and WMO climate reference (1996-2020), D: Mean summer precipitation at Findelbach station over the study period and WMO climate reference (1990-2020) 87
6.9 In-situ photos (a, b) of the site at different times during field study of Christine Schärer (2018). c/d show possible clay horizons. 89
6.10 Tripfen slope flank and release area in 2006 and 2009. 90
6.11 Three possible mass movement scenarios at the IR slope. 91

7.1 All picked boulders at the IR slope. Boulder symbols represent the slope topology. 107
7.2 All picked boulders at the Tripfen slope. Boulder symbols represent the slope topology. 108
7.3 Innere Rimpfischwäng slope topology and the underlying process domains. . . 109
7.4 Tripfen slope topology and the underlying process domains. 109
7.5 The main scarp filled with material in later years. 110
7.6 Velocity heatmap of each boulder picked at IR slope 111
7.7 Mean elevation at each year for transect 12-17. The elevation represents only the mean elevation from the transect from 200 to 400 meters. 112
7.8 All DoD at IR over the study periode 2012–2024. 112
7.9 All DoD at Tripfen over the study period 2012–2024. 113
7.10 Monthly temperature at Gronergrad from 2012–2024 and estimate correction for the study sites. 113

7.11 Precipitation over the study period at the Findelbach 2012–2024 114
7.12 Correlation between velocity and Temperature and Precipitation 114
7.13 The green lines indicate wet areas (darker) where water is presumably pressing through the moraine from the river and tiny lakes at the same elevation on the other side of the moraine, at Findelengletscher (VS), Switzerland (Alexander Ruff, 2015) 115

List of Tables

4.1 DSM and DOP dataset acquisition details for Findel Glacier (2012–2024). swissALTI3D was used for the DSM in 2018. 35

4.2 Co-registration performance metrics for DSM datasets (2012–2023) 41

4.3 Systematic error and random error over stable terrain 42

4.4 Remaining DOP co-registration uncertainty relative to the 2024 DOP reference. 43

7.1 Overview of auxiliary datasets used in this study. 107

7.2 Depletion and Accumulation of material in the unstable Area at IR slope. Material transported outside the area is not captured in the Accumulation material. 111

List of abbreviations

- **DSGSD** = Deep-seated gravitational slope deformation
- **IR** = Innere Rimpfischwäng
- **ZSZ** = Zermatt-Saas ophiolite zone
- **DOP** =Digital orthophotos
- **DSM** = Digital surface models
- **DEM** = Digital elevation models
- **ALS** = Airbonre laserscanner
- **MED** = Median elevation difference
- **NMAD** = Normalised median absolute deviation
- **RMSE** = Root mean square error
- **DoD** = DEM of difference
- **LIA** = Little ice age
- **SLF** = Institute for snow and avalanche
- **ERT** = Electrical resistivity tomography

Introduction

Most Swiss glaciers are projected to disappear by the end of this century (Zekollari et al., 2019; Zemp et al., 2025). As glaciers retreat, new slopes, soil and bedrock are exposed to atmospheric processes and the hydrological cycles. Beyond primary succession, mass movement is one of the dominant processes reshaping the paraglacial environment. There are many factors which affect slopes depending on elevation and topography (Benn et al., 2014). Climate change will further accelerate mass movement processes throughout this century (D'Amato et al., 2016; Ravanel and Deline, 2011; Stoffel et al., 2024) as an increasing number of intense precipitation events and rising temperatures accelerate the water cycle (IPCC, 2023; McColl and Draebing, 2019; McColl, 2012). This enhanced hydrological cycle can intensify thaw-freeze cycles, promote fracture propagation and mobilise entire slopes (Hou et al., 2025; Tan et al., 2025).

These hazards are not merely theoretical. Just last year, a mountain face collapsed in the Lötschental (a valley in Switzerland), demonstrating the destructive power of slope failure (Florian Meyer, 2025). While that was a rare event, resulting from a cascade of circumstances, it underscores the danger mass movement poses to human lives and infrastructure. Understanding, where and when such events occur, is essential for protecting lives, infrastructure and ecosystems (Huggel, 2015; Sousa et al., 2021).

However, while many engineering studies examine the slope stability around mines and roads (Hou et al., 2025; Tan et al., 2025), the specific factors driving slope instability in remote high mountain areas remain less well understood. Predicting the exact timing of rockfalls or major slope movements remains difficult. A better understanding of the processes in the paraglacial environment would improve hazard assessment in high mountain regions, particularly important in areas where human populations and infrastructure are at stake. The Findel Glacier area in Switzerland offers an ideal case study, as the glacier has undergone significant retreat over recent decades (GLAMOS, 2026), initiating the transition from a glacial to a paraglacial environment. A previously documented slope instability at the glacier margin (Alexander Ruff, 2015; Christine Schärer, 2018) provides an opportunity to examine how mass movements develop during glacier recession and which other instabilities can be observed in such settings. By using high-resolution airborne data, we can analyse the natural processes which cause slope instability and reshape the glacier forefield. This thesis focuses on (1) quantifying changes and (2) investigating the controlling factors of mass movements in the forefield and margins of Findel Glacier.

1.1 Research questions

To address these objectives, this thesis aims to answer the following research questions:

How did the Findel Glacier and the glacier forefield change during the 13-year period from 2012 and 2024?

- Which geomorphological process domain can be observed at the Findel slopes?
- How much horizontal and vertical changes did the study area experience since 2012?
- How did the slopes and glacier forefield evolve annually over the study period?

Which processes drive mass movement processes at the Findel Glacier margins and what are their controlling factors?

- Which are the main processes and factors driving changes at the study site, considering permafrost, meteorological data, debuttressing, geology, slope angle and topography?
- Do the two studied slopes share common process patterns, or do they respond differently to the same controlling factors?
- How can the identified mass movements be classified according to established typologies (Hungr et al., 2014)?

Theoretical background

This chapter introduces the scientific background relevant to this thesis. It presents the different geomorphological environmental characteristics of the study area, followed by a review of mass movement processes in high mountain areas, including their types and underlying mechanisms. Subsequently, the main factors influencing slope instability are discussed, with a particular focus on glacier retreat and debuttressing, climate controls, permafrost, and geology.

2.1 Geomorphological environments

Geomorphology is the science that classifies relief and describes processes shaping the landscape (Dikau et al., 2019). It contains many sub-disciplines, ranging from natural to anthropogenic processes. This study falls within the domain of process geomorphology, which focuses on the relationships between physical, chemical and biological processes that shape reliefs (Dikau et al., 2019).

Process geomorphology uses the concept of process domains to categorise environments in which the same dominant processes operate, regardless of their location on Earth (Dikau et al., 2019). High mountain environments are characterised by cold climates, steep terrain and snow accumulation, which create heterogeneous landforms. These landforms are also strongly influenced by climate change, leading to a shift in the dominant processes and landforms. This concept is described as paraglacial geomorphology by Cossart and Fort (2008), which describes the transition from a glacial environment to a non-glacial environment encompassing both periglacial and paraglacial stages. Depending on the stage of this transition, different forms of sediment transport and mass movement processes dominate the landscape. Which can be seen in fig. 2.1.

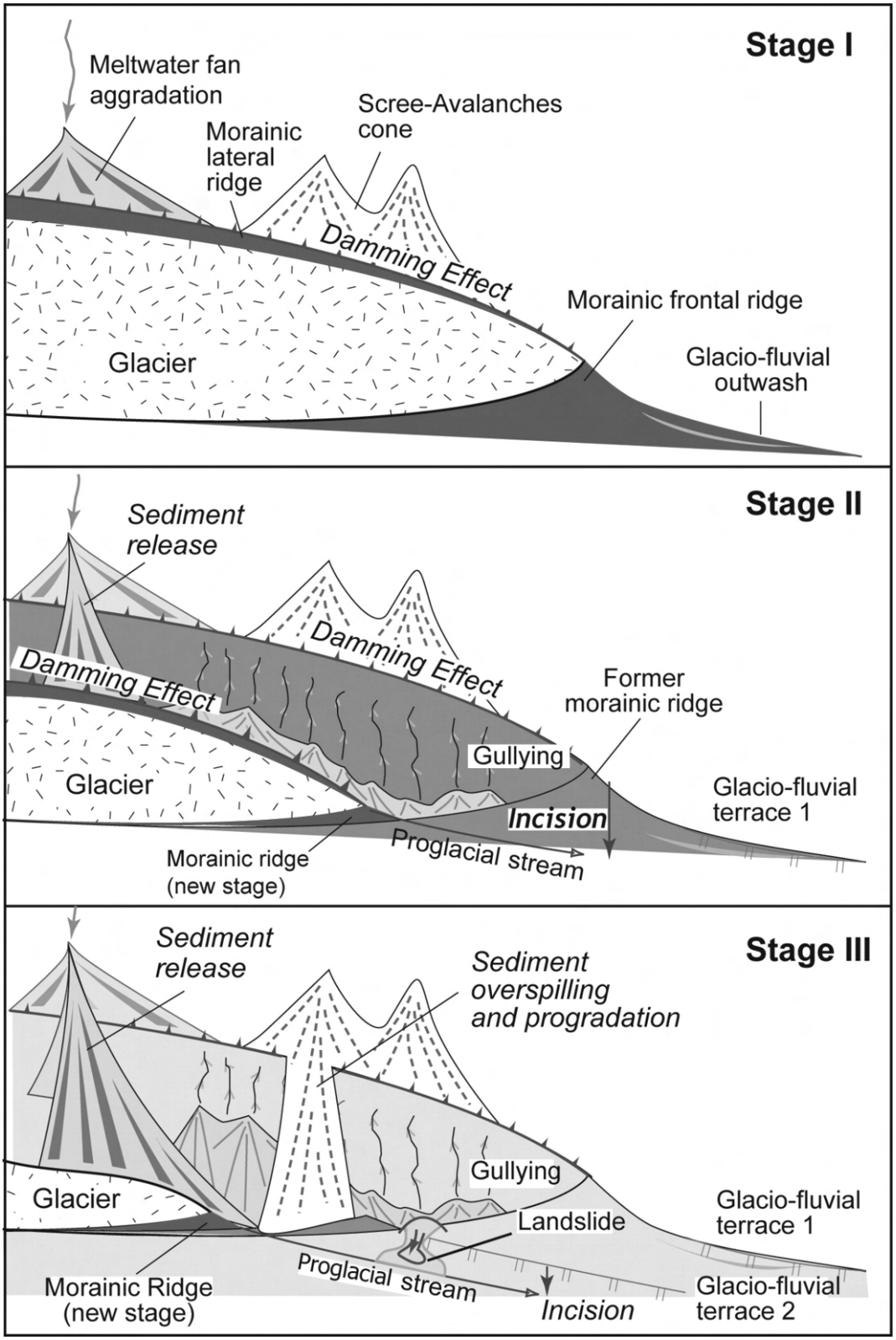

Figure 2.1: Sketch showing the geomorphological evolution of the glacier forefield and its margins after the glacier's retreat. Depending on the retreating stage, different processes act on the landscape (Cossart and Fort, 2008)

.

The Swiss Alpine regions have been transitioning from a glacial environment toward periglacial and paraglacial landscapes since the Little Ice Age (ca. 1850) (Carrivick and Heckmann, 2017). The following sections describe each of these process domains in detail.

2.1.1 Glacial environments

The glacial environment is characterised by the presence of glaciers. Glaciers are defined as "a perennial mass of ice, and possibly firn and snow, originating on the land surface by the recrystallisation of snow or other forms of solid precipitation and showing evidence of past or present flow." (Hooke, 2011; Windnagel et al., 2023). Ice and snow begin to flow under their own weight if sufficient mass has accumulated (U.S. Geological Survey, 2021). Glaciers therefore only exist in cold climates where temperature and precipitation allow snow to persist over more than one season and can be transformed into ice (Windnagel et al., 2023). Hence, many high mountain areas, such as the Alps, contain glaciers. There are many different types of glaciers, and their large mass makes them a dominant force in landscape-forming processes (Hambrey and Alean, 2016).

Glaciers have the power to erode their underlying bedrock through glacial abrasion and striation (Hambrey and Alean, 2016). Glaciers act as a conveyor belt for material transport, and mass movements, such as rockfall at the glacier margins, add additional material to the glacial system. There are three types of sediment transport: supraglacial (on the glacier surface), englacial (within the glacier) and subglacial (beneath the glacier). This material is ultimately deposited in the glacier forefield or at the glacier margins as moraines (Hambrey and Alean, 2016). Lateral moraines form along glacier margins where the glacier is not confined by bedrock. Terminal moraines, also called end moraines, form where the advancing glacier tongue pushes material forward. Moraines contain a wide variety of grain sizes and rock material textures and evolve through glacier advance and recession phases, during which ice, glacial sediment and debris are incorporated into them (see fig. 2.2).

Glaciers are one of the dominant features of alpine landscapes. Even after they disappear, their imprint remains visible in many alpine valleys, leaving relict landforms from past advance phases and overdeepened valley floors (Douglas I. Benn and David J.A. Evans, 2010; McColl, 2012). The retreat of glaciers exposes new terrain and initiates a transition towards paraglacial and periglacial conditions, which are described in the following sections.

2.1.2 Periglacial environments

The periglacial environment is described by French (2017) as a zone where cold, non-glacial conditions reign and where oscillations between freezing and thawing dominate geomorphological processes. Permafrost is a common feature, but it is not necessarily a criterion for periglacial environments.

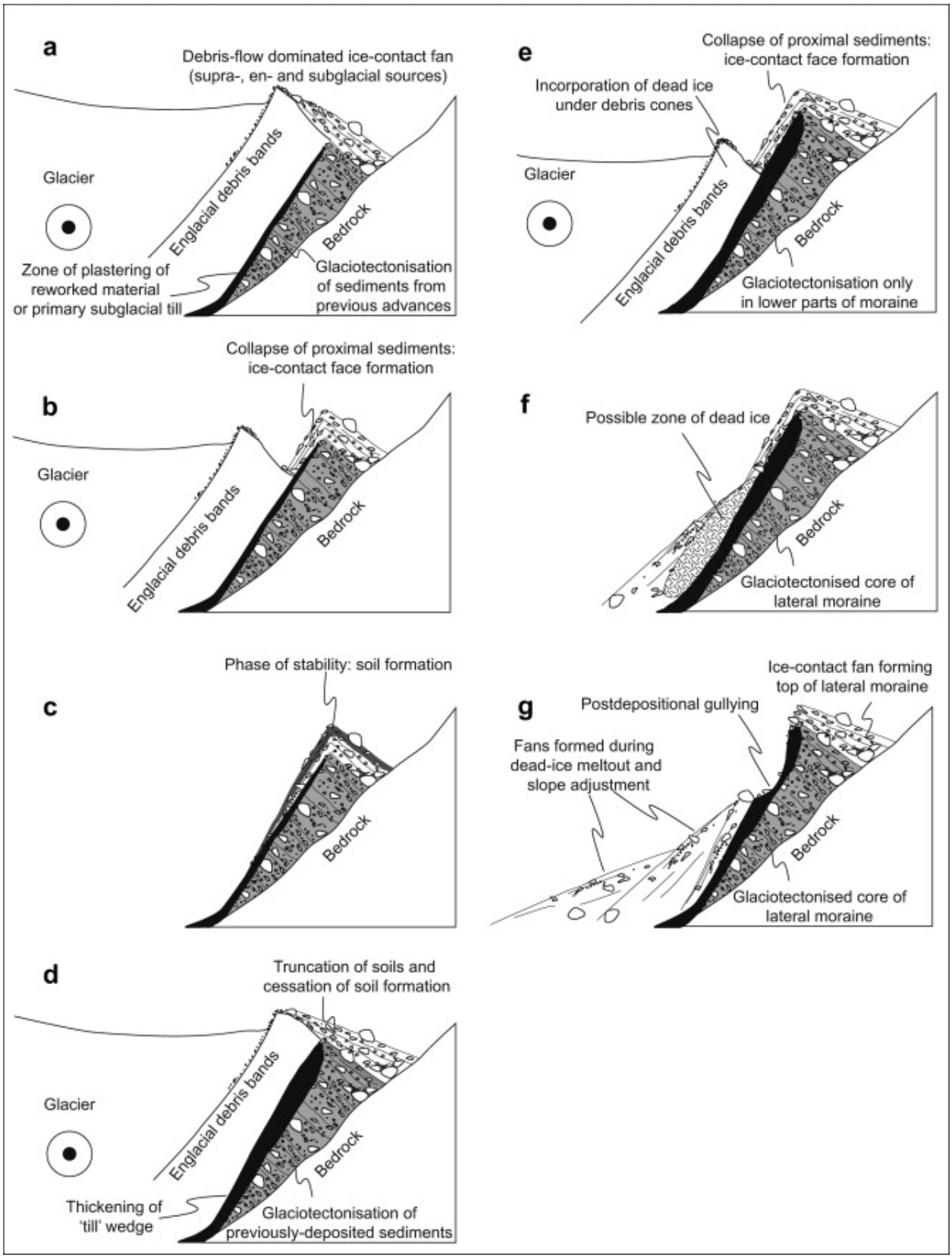

Figure 2.2: The temporal evolution of moraines depending on glacier advance and retreat phases (Lukas et al., 2012)

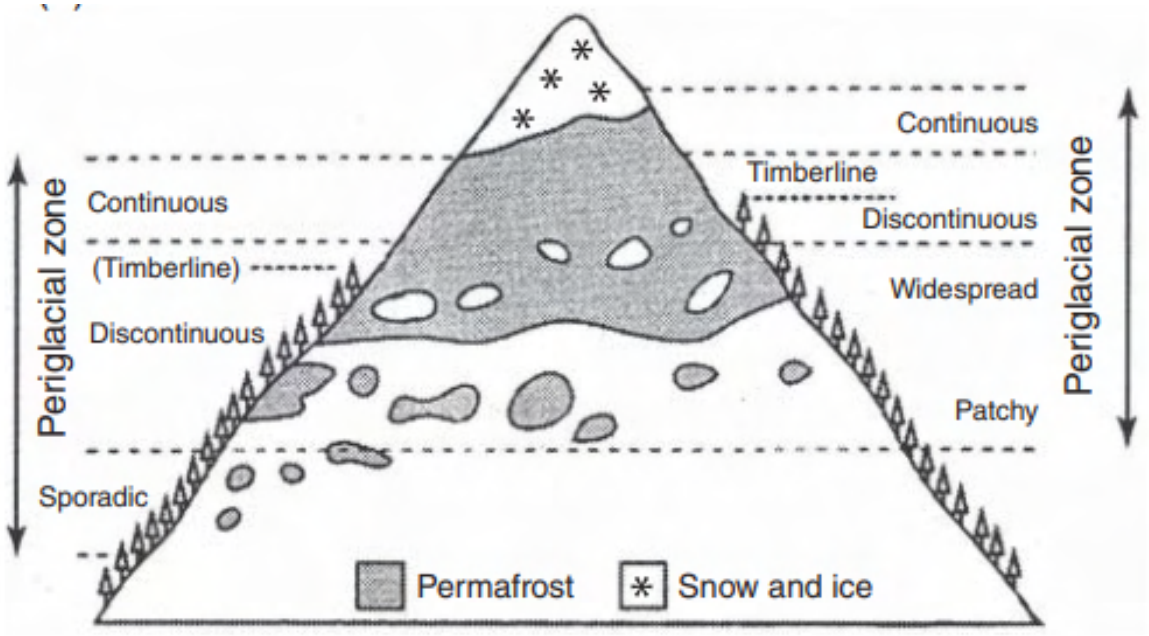

Figure 2.3: Periglacial concept by French (2017) showing the distribution of permafrost and snow and Ice

Periglacial environments can be found at various locations around the world, predominantly at high latitudes and in polar regions, but also in high altitude mountain ranges such as the Alps, the Himalaya, and the tropical Andes, and many other mountain ranges worldwide. Even at lower elevation mountain regions, remnants of periglacial settings persist in the form of relict features (French, 2017). Although current climatic conditions may no longer allow the formation of new periglacial features in lower latitude, these relics continue to shape the landscape. Examples of such regions include the Sierra Nevada and the High Atlas mountain range, as well as the Russian Tundra (Garankina et al., 2022; Oliva et al., 2022; Vieira et al., 2017). The dominant processes in periglacial environments include frost weathering, frost heave, solifluction, rock glaciers, and the formation of patterned ground features such as ice wedges, pingos and many more. These processes are driven by repeated freeze-thaw cycles that occur seasonally or diurnally, depending on the specific thermal regime. The vegetation in periglacial environments is limited to cold-adapted species that can withstand the freeze-thaw cycles and harsh thermal conditions (French, 2017). In high mountain areas, rock glaciers are a clear sign of periglacial environments. They occur when unconsolidated sediment contains an ice core formed from snow, avalanches, or buried glacier ice, which is preserved through sediment insulation over centuries (Dikau et al., 2019). Haeberli et al. (1998) found that this permafrost ice inside rock glaciers can even been relicts from Holocene glaciations. In the literature, another genesis of rock glaciers is debated. Here, the ice originates from in-situ freezing of water within talus slopes through ice segregation. Therefore,

the ice content of rock glaciers varies depending on the source of water and the location of the surrounding area (Noetzli and Phillips, 2019).

2.1.3 Paraglacial environments

The paraglacial environment is described as encompassing "non-glacial processes that are directly conditioned by glaciation" (Church and Ryder, 1972; Ballantyne, 2002). It refers both to proglacial processes and to those occurring around and within the margins of a former glacier that are the direct result of the former presence of ice (Ballantyne, 2002). Paraglacial environments, therefore, represent landscapes undergoing adjustments following deglaciation. They are no longer directly influenced by active glaciers. Unlike periglacial environments, which are characterised by freeze-thaw processes, paraglacial environments are defined by the reworking of glacially conditioned sediments and landforms through various geomorphological processes. These transitional zones are particularly vulnerable to slope instability in mountain environments. As glaciers retreat, weathered rock masses and unconsolidated glacial sediments are exposed, leading to increased mass movement activities through mass movement processes (Ballantyne, 2002; Laigle and Bardou, 2022; McColl, 2012).

2.2 Mass movements

Mass movements exhibit a wide variety of characteristics, and several attempts have been made to categorise them. As highlighted by Shanmugam and Wang (2015), there are significant flaws in the nomenclature of mass movements, particularly within the field of geology and related subdisciplines. This thesis adopts a nomenclature from a geomorphological perspective that uses the type of movement as the main distinguishing factor. This classification system was first described by Varnes (1978), who identified six types of slope failure movements: falls, topples, spreads, translational slides, rotational slides and flows.

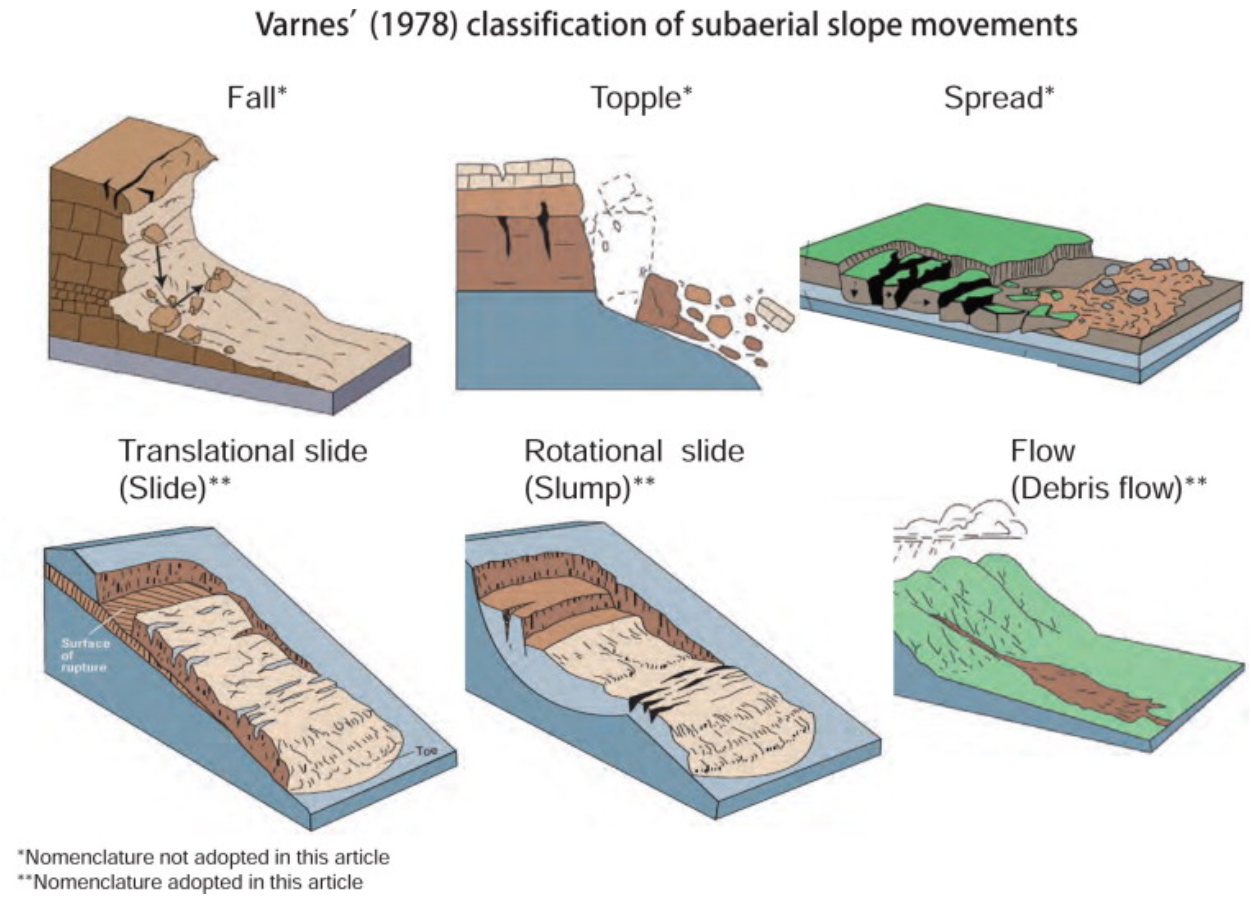

Figure 2.4: Visualisation of the 6 different mass movement as defined by Varnes (1978) (Shanmugam and Wang, 2015)

Hungr et al. (2014) refined this classification to 32 different types of mass movements based on material types and movement mechanisms. In this section, only the mass movement processes relevant to periglacial and paraglacial environments are described, following the classifications of Varnes (1978); Hungr et al. (2014), and Laigle and Bardou (2022). It is important to acknowledge that these categories are discrete sections along a continuous range of mass movement behaviour. In nature, one event can under certain conditions transform or be transformed into another type. While gravity is the fundamental driving force of all mass movements, the triggering mechanisms vary from site to site. Some of the common triggers for mass movement processes are seismic activity, extensive rain events, fracture propagation, and thawing of permafrost. This list is not complete, and it is uncertain how some of the factors influence slope failures (McColl, 2012).

2.2.1 Solifluction



Figure 2.5: Solifluction lobe bound by vegetation at Meretschialp, Valais, Switzerland (Dikau et al., 2019).

Solifluction is the slow downslope creep of soil. It's a very slow form of flow according to Varnes (1978). This mass movement is driven by shear stress that leads to permanent deformation but is not strong enough to produce discrete shear failures (Hungr et al., 2014; Laigle and Bardou, 2022). Solifluction is very common in periglacial environments such as the Alps (French, 2017). During thawing cycles, the active layer (the uppermost soil layer that thaws seasonally) becomes mobile. This process has to involve some kind of water/ice, but it is not necessary to be fully saturated soil. This soil is slowly moving downward over the still-frozen substrate beneath. This differential movement produces characteristic features such as solifluction lobes and terraces (Matsuoka, 2001).

2.2.2 Debris flow



Figure 2.6: A debris flow at the lower section of Illgraben(Image: WSL) (Michael Keller, 2021).

A debris flow is a rapidly flowing mixture of water, rocks, soil and organic matter. It is a common type of mass movement in high mountain areas that occurs at steep slopes and in narrow channels. For debris flows to occur, the material must be mobilised by water. Heavy precipitation is not the only trigger; thawing permafrost and glacier melt are also frequent triggers for debris flows (Laigle and Bardou, 2022). Debris flows are highly destructive because they carry significant momentum and mass. They can reach infrastructure and settlements in alpine communities even when their origin is far away. They also impact the channels through which they flow as their high velocity erodes the channel bed and banks, leaving steep levees behind (Hungr et al., 2014; Laigle and Bardou, 2022).

2.2.3 Rock avalanche



Figure 2.7: The bulging Birch glacier covered a rock avalanche before the glacier collapsed under the load of the rock masses (Image: KEYSTONE / Jean-Christophe Bott) on 23 May 2025 (Florian Meyer, 2025)

This mass movement type is extremely rapid, with velocities of 10-100 m/s, and can involve very large volumes, if an entire rock face collapses (Laigle and Bardou, 2022). When rock avalanches are initially observed, the material is typically dry during the failure phase. However, as the avalanche moves downslope and erodes saturated soil or impacts on a glacier, the rock avalanche can easily become liquefied through the incorporation of water and ice (Hungr et al., 2014). This transformation was observed in the disasters at Bondo and Blatten, where initially dry rock material became liquefied through interaction with saturated sediments, glacier material that melted during the impact or subsequent fragmentation (Peter Höllrigl, 2018; Daniel Farinotti et al., 2025). Among the common triggers of rock avalanches are earthquakes (McColl, 2012).

2.2.4 Rockfalls



Figure 2.8: Rockfall at Mel de la Niva captured by Ludwig Haas, canton Valais. (Institut für Schnee- und Lawinenforschung SLF, 2025)

Rockfalls are characterised by the detachment of rock from its source, which then falls, rolls, and bounces downslope. The key difference between rock avalanches and rockfalls is that rockfalls involve discrete volumes of material, which move as individual blocks or fragments rather than as a flowing, fragmenting mass (Hungr et al., 2014). Consequently, rockfalls typically entrain less additional material during their downslope movement compared to rock avalanches. Rockfalls are triggered when the internal strength of the rock mass is reduced by various factors, including permafrost degradation, freeze-thaw cycles that progressively widen cracks, erosion that undercuts or destabilises the slope, root wedging, increased pore water pressure of the rainfall or snowmelt, seismic activity or even anthropogenic disturbances such as construction activities (Institut für Schnee- und Lawinenforschung SLF, 2025). Rockfall events typically result from a combination of multiple factors rather than a single cause (McColl, 2012). Areas with high relief topography and steep rock faces, particularly in alpine environments, frequently experience rockfall activities (McColl, 2012; Stoffel et al., 2024; Institut für Schnee- und Lawinenforschung SLF, 2025).

In Switzerland, the Institute for Snow and Avalanche Research (SLF) has developed a volume-based classification system for rockfall events that helps to assess event severity and gives information for hazard management strategies (Institut für Schnee- und Lawinenforschung SLF, 2025).

- Mountain falls: $> 10^6$ m^3 (>1,000,000 m^3)
- Rockfalls: 100–10^6 m^3
- Boulder falls: 0.5–100 m^3
- Stone falls: <0.5 m^3

2.2.5 Rockslides



Figure 2.9: A rotational slide involving Cretaceous shale, overlain by sandstone. Liard Plateau, Canada (Photo by O. Hungr)(Hungr et al., 2014)

Rockslides are classified according to the geometry of their rupture surfaces and the mechanisms controlling their movement (Hungr et al., 2014). The main types include rotational, planar, wedge, compound and irregular rockslides. Rotational rockslides occur on curved rupture surfaces and have a characteristic main scarp and back-tilted motion. Additionally, their internal deformation is relatively low. These slides occur in weak rock masses that are overlain by a stronger rock cap. The general motion is rather moderate and is also known as self-stabilising movement, since with more displacement there is less gravitational force acting on the rock mass (Hungr et al., 2014).

Planar rockslides have a single planar discontinuity; in sedimentary and metamorphic rocks, bedding planes, fault surfaces, or exfoliation joints act as this sliding horizon. Unlike rotational slides, planar sliding is not self-stabilising, and these failures tend to be extremely rapid. The volume of these slides can exceed 100 million m^3, as occurred in the 1248 rockslide in the Savoy Alps, a catastrophic event (Hungr et al., 2014).

Wedge slides occur when two discontinuities intersect to form a wedge-shaped failure surface with a downslope-oriented intersection line. These slides are mechanically similar to planar slides but involve increased resistance due to friction actions on two surfaces simultaneously (Hungr et al., 2014).

Compound rockslides have multiple discontinuity planes, which act as rupture surfaces. The sliding motion is only possible due to internal deformation. This is common in limestone rock masses (Hungr et al., 2014).

There are also combinations or unclear rupture surfaces that Hungr et al. (2014) categorised as irregular rockslides. These rock collapses occur when discontinuities on the slope get connected, and the rock bridges cannot resist the shear stress of gravitational forces, and a complex rupture surface emerges. This was observed at the Randa rockslide in 1991, where complex crack propagation was observed before the rock face collapsed (Hungr et al., 2014).

2.2.6 Gravitational slope deformations

Mountain slope deformations are extremely slow mass movements (Hungr et al., 2014). They are defined as large-scale gravitational deformations of steep mountain slopes, typically with a vertical relief exceeding 1 km, manifested by benches, cracks, bulges, double-crested ridges, trenches, and synthetic and antithetic uphill-facing scarps (Hungr et al., 2014; Pánek and Klimeš, 2016), but lacking a fully defined rupture surface (Hungr et al., 2014). Movement rates are often so slow that they cannot be measured. The style of deformation varies depending on rock mass structure relative to slope orientation and can resemble early stages of rotational sliding, compound sliding or toppling movements. Most mountain slopes remain stable over historic timescales (Hungr et al., 2014).

Mountain slope deformation describes large-scale deformation of mountain slopes, while for smaller rock slopes the term rock slope deformation is often used (Hungr et al., 2014). The terms sagging (”Sackung”) and deep-seated gravitational slope deformation (DSGSD) are used to describe slow-moving rock mass movements affecting valley flanks, exhibiting the same landform features as mountain slope deformations but on a larger scale. These terms are often applied when the boundaries of the deforming mass are unclear (Pánek and Klimeš, 2016). DSGSD emphasise how valley flanks or slope flanks have evolved since the Last Glacial Maximum or over even longer timescales (Pánek and Klimeš, 2016). There are two modes of movement: one is continuous creep and the other episodic movements, where catastrophic failure can occur (Pánek and Klimeš, 2016).

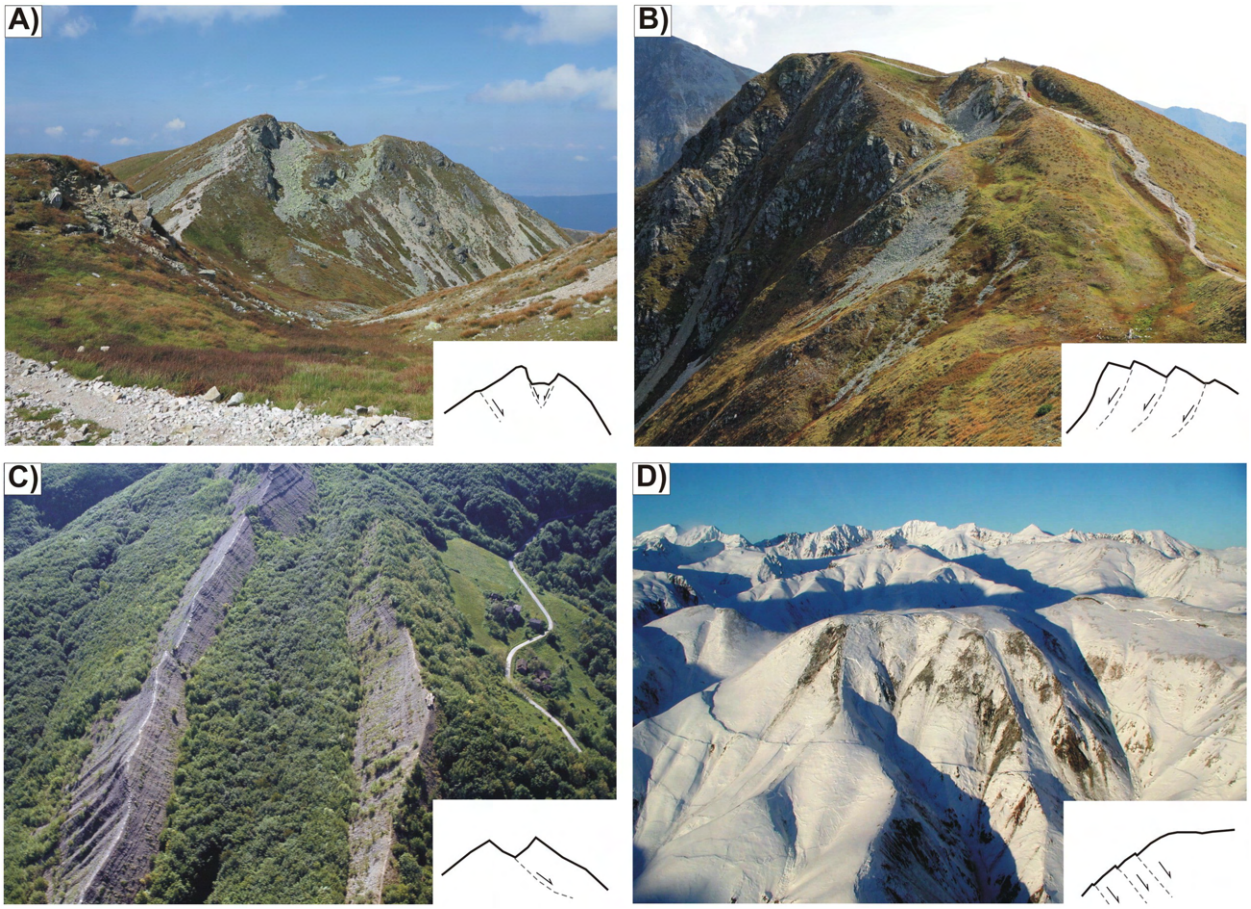

Figure 2.10: "Examples of frequently occurring modes of DSGSDs from various types of landscapes. A. Ridge-top graben affecting granodiorites of the Salatín Mt. (Tatra Mts., Slovakia). B. Asymmetric sagging (ridge displacement to the left) affecting SE part of the Salatín ridge (Tatra Mts, Slovakia). Cases A and B are examples of DSGSDs situated in mountains that were heavily glaciated during the Late Pleistocene (final deglaciation about 11 ka; Makos et al., 2014) C. Nearly 3 km long double ridge on non-glaciated flysch terrain (Mt. Barigazzo, Northern Apennines, Italy; photo courtesy: G. Bertolini). D. Series of uphill-facing scarps at the Gilette Pass (Alaska, USA) produced by the 2002 Denali Fault earthquake. (Photo courtesy: U.S. Geological Survey/photo by Peter Haeussle.)" (Pánek and Klimeš, 2016)

Crosta et al. (2013) analysed an inventory of 1033 DSGSDs across the entire European Alps and investigated their controlling factors. Their results indicate that the occurrence of foliated metamorphic rocks, former LGM ice thickness, local relief, slope size and drainage density are the parameters most strongly correlated with DSGSD occurrence. The controlling factors can be grouped into internal factors, such as lithology, geological structure and rock mass quality, and external factors, such as glaciation and debuttressing, seismicity, climate and groundwater regime (Crosta et al., 2013).

One approach to measuring these deformations in the field is through boreholes (Yamamoto et al., 2023). Inclinometers measure the displacement (fig. 2.11). The drilled cores help to understand the geology of the slope. With both sources of information, a prediction of the sliding horizon can be made. The authors found that the movement pattern changed from creep to sliding when the groundwater level rose, highlighting the important role of groundwater in slope stability (Yamamoto et al., 2023).

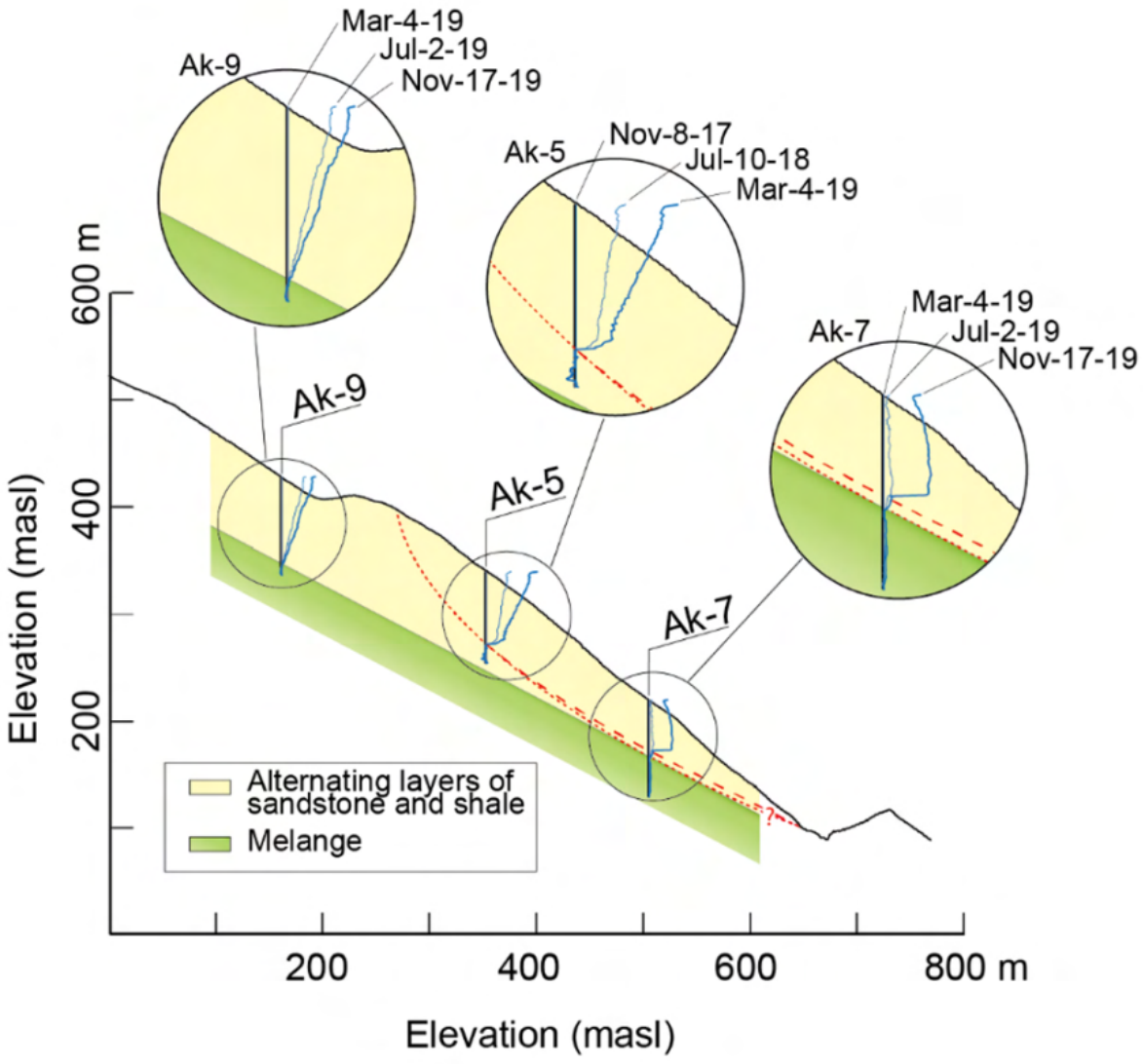

Figure 2.11: Borehole measurement which showed movement pattern of slope and the rupture surface (Yamamoto et al., 2023)

2.3 Slope controlling variables

Mass movements are affected by internal and external factors. This section focuses on a brief overview of the variables and highlights the mechanism in the context of slope instability.

2.3.1 External factors

2.3.1.1 Glacier retreat and debuttressing

Temperature and precipitation control the size of glaciers. With higher temperatures, there will be more ice melt, while less precipitation leads to less snow accumulation and vice versa. In recent decades, a worldwide trend of glacier retreat was observed (Zemp et al., 2025; GLAMOS, 2026). Glacier ice provides additional resistance against the shear force of the slope. This effect is called buttressing (McColl et al., 2010) and can be seen in fig. 2.12. When glaciers retreat, the loss of ice masses also decreases the support, which is called debuttressing (Grämiger et al., 2017).

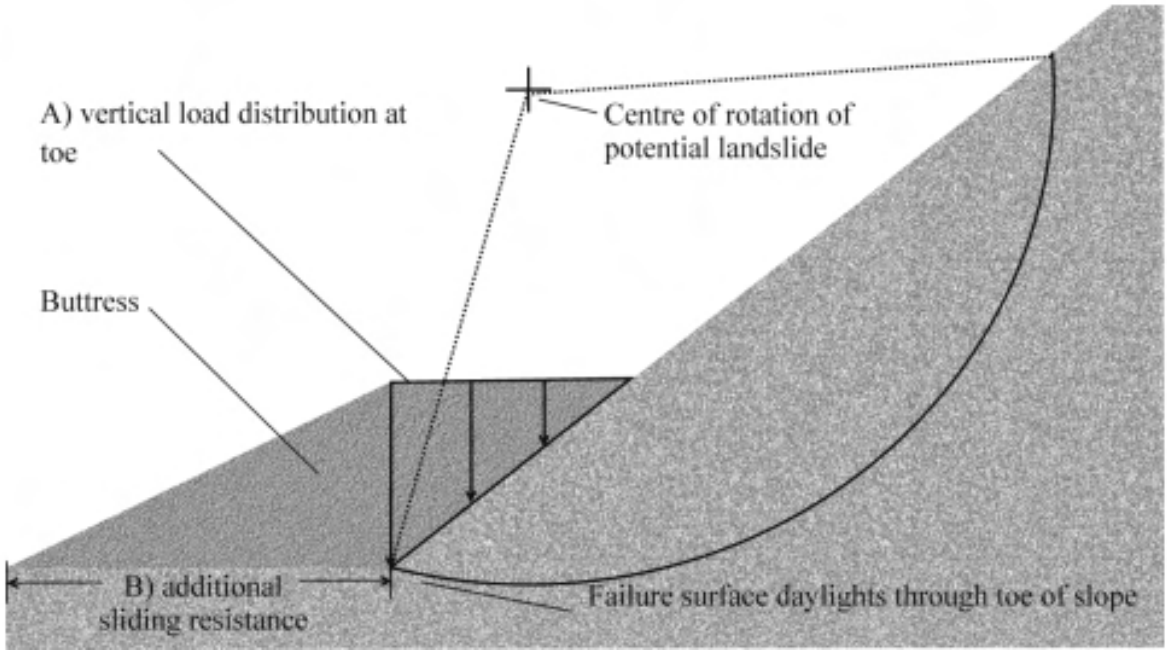

Figure 2.12: "Rock slope with potential slope failure being buttressed. A toe-of-slope buttress provides external support to a slope by adding a vertical load surcharge to the toe (A) and by providing additional sliding (shear) resistance (B). The buttress counterbalances the forces driving landslide displacement" (McColl et al., 2010)

Many studies have investigated whether glaciers can provide support for adjacent rock slopes (Grämiger et al., 2017; McColl et al., 2010; McColl, 2012). Most agree that ice cannot

provide sufficient support for slope stabilisation, as ice is more ductile than rock (McColl et al., 2010; Grämiger et al., 2017). However, glacier fluctuations are effective in inducing rock damage, which lowers the strength of the slope. Periods of low ice thickness also expose the slope to other environmental processes such as ice segregation, chemical weathering of joints, changes in joint water pressure, thermal stresses and seismic activity (Grämiger et al., 2017; McColl et al., 2010). Therefore, debuttressing has only a minor direct effect on slope stability, but glacier advance and retreat affect many factors that promote erosion and weakening of slopes. Dated slope instabilities in the Aletsch area showed a significant time lag of several thousand years relative to previous glacier retreat phases following the LGM or Egesen maximum (Grämiger et al., 2017). It is therefore difficult to directly link slope instability to glacier retreat.

2.3.1.2 Climate variables

Temperature and precipitation are the two fundamental variables defining climate and together control the energy and the water balance of a system. Both act strongly on geomorphological processes, particularly in high mountain areas where they control the thermal state of the ground, the snowpack and the distribution of ice (Pepin et al., 2022; IPCC, 2023).

Temperature has a great influence on ice, snowpack and permafrost. Rising temperatures increase the amount of energy transferred to soil, rock and ice, leading to melting or warming of rock and soil. In permafrost bodies, the thickness of the active layer increases (Zhou et al., 2022) or, where permafrost is very shallow, may lead to its complete loss (Huss et al., 2017). Larger temperature differences promote freeze-thaw cycles, which are among the most effective physical weathering mechanisms (D'Amato et al., 2016; Matsuoka and Murton, 2008; Fischer and Huggel, 2008; McColl, 2012; Stoffel et al., 2024). Heat waves and prolonged warm periods appear to correlate with increased rockfall frequency (Ravanel and Deline, 2011). Higher temperatures, therefore, enhance many natural processes that have a destabilising effect on slope stability.

Precipitation has a great influence on rockfalls. Rainfall can increase water pressure in rock joints, dissolve minerals in rocks and result in thermal stress which propagates cracks (D'Amato et al., 2016). Many landslides are triggered by precipitation (Huggel et al., 2012; Bhuyan et al., 2024; Gautam et al., 2021; Hsieh et al., 2016; Sousa et al., 2021). When the snow pack begins to melt in spring, the water can infiltrate the soil and rock. In high mountain areas, the snow pack can reach 1–2 metres in thickness, and on glaciers even up to 4 meters (SLF, 2026). This infiltration leads to changes in the groundwater table, which decreases slope stability (Bajni et al., 2021). Another aspect of precipitation is how ecosystems depend on water availability. Depending on precipitation, vegetation ranges from complex structures such as shrubs and trees to grasses. Vegetation has two contrasting effects on slopes. On one hand, roots can widen cracks and joints, promoting mechanical

weathering (Institut für Schnee- und Lawinenforschung SLF, 2025). On the other hand, vegetation has a stabilising effect on slopes through primary succession. Primary succession is the process following on glacier retreat, where lichens and mosses first colonise newly exposed surfaces, followed by pioneer plants and eventually shrubs and grasses. Schumann et al. (2016) showed that greater vegetation cover stabilises the soil, as root structures bind the soil and increase its water retention capacity before saturation is reached (Masi et al., 2021).

Climate change affects both temperature and precipitation substantially. Projections indicate that heat waves and heavy rainfall events will increase in frequency in a warmer world compared to pre-industrial periods. More intense rainfall events are expected since warmer air can hold more moisture (IPCC, 2023).

Heat waves and heavy rainfall showed significant correlations with mass movement and slope instability in many sites and studies around the world (Matsuoka and Murton, 2008; Ravanel and Deline, 2011; D'Amato et al., 2016; Huggel et al., 2012; Sousa et al., 2021). Higher temperature and more precipitation increase the chemical and physical erosion and therefore contribute to slope instability (Dikau et al., 2019).

2.3.2 Interal factors

2.3.2.1 Permafrost

Permafrost is a thermal state of the subsurface. It is defined as ground (soil or rock, including any ice or organic material) that remains at or below 0°C for at least two consecutive years (International Permafrost Association, 2026). The presence of water or ice is not required for the ground to be classified as permafrost; the definition is based solely on the temperature criteria (Dobinski, 2011). Although permafrost commonly occurs in periglacial environments, periglacial processes are not exclusively dependent on the presence of permafrost. In alpine and polar regions, where permafrost occurs, a typical vertical stratigraphy develops with distinct thermal layers fig. 2.13. The active layer is the uppermost zone, which is strongly influenced by seasonal atmospheric temperature variations. Consequently, this layer is exposed to seasonal freezing and thawing. Below the active layer lies the permafrost body, which is perennially frozen as shown in fig. 2.13, meaning it remains at or below 0°C throughout the year. Below the permafrost base lies the perennially unfrozen layer, where geothermal heat maintains temperatures above 0°C year-round (Dobinski, 2011).

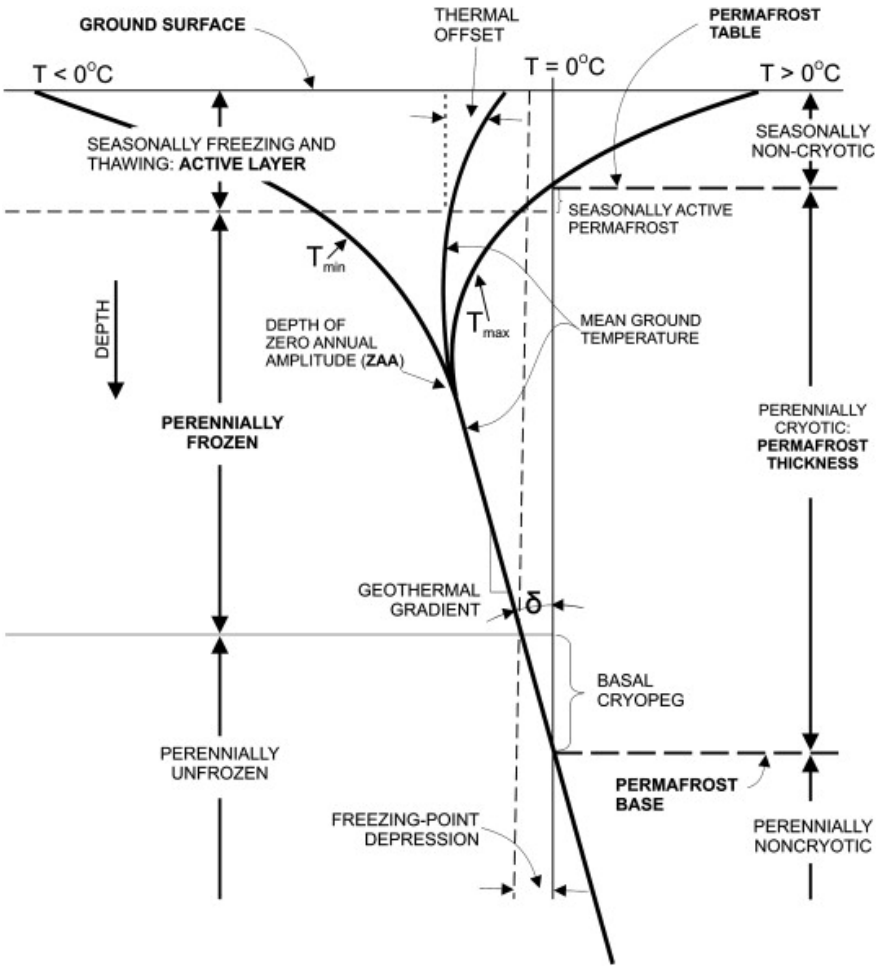

Figure 2.13: "Thermophysical model of permafrost of a periglacial environment and associated terms used to describe the ground temperature relative to 0 °C, after van Everdigen (1998), with changes" (Dobinski, 2011)

.

As many studies have shown, debris flows commonly occur in areas of previous permafrost (Carrivick and Heckmann, 2017). Many rock detachments are found at degraded permafrost locations (Fischer et al., 2006, 2010; Huggel et al., 2012; Matsuoka and Murton, 2008; Ravanel and Deline, 2011). When permafrost warms, the shear strength of ice-filled discontinuities in rock slopes changes. At low ice temperatures, the factor of safety can be significantly higher than for an unfrozen slope. However, as the ice warms, the factor of safety decreases and can fall below that of an ice-free slope. This means that slopes near 0°C become more unstable than ice-free slopes (Davies et al., 2001; Krautblatter et al., 2013). Numerical models and field measurements indicate that increased liquid water content at the freeze-thaw interface raises pore water pressure and thereby reduces effective stress (Hou et al., 2025). Permafrost temperature measurements in the Swiss Alps have shown a clear trend of rising temperatures in recent decades (Davies et al., 2001; Krautblatter et al., 2013). These studies highlight that degrading permafrost conditions tend to have a negative effect on slope stability.

2.3.2.2 Geology

The morphology of the slope depends on the geology. The different types of geological structures behave differently to stress (Ambrosi and Crosta, 2011). In geology, the rock stability is often described by the term factor of safety. The factor of safety is defined as the ratio of resisting to driving forces (or moments), first described by Terzaghi, K. et al. (1958) and still commonly used in stability assessments of slopes and rock masses (Stead and Wolter, 2015):

$$FS = \frac{\text{Resisting forces (or moments)}}{\text{Driving forces (or moments)}} \tag{2.1}$$

where $FS > 1$ indicates a stable slope, $FS = 1$ represents the critical stability threshold, and $FS < 1$ indicates failure (see fig. 2.14).

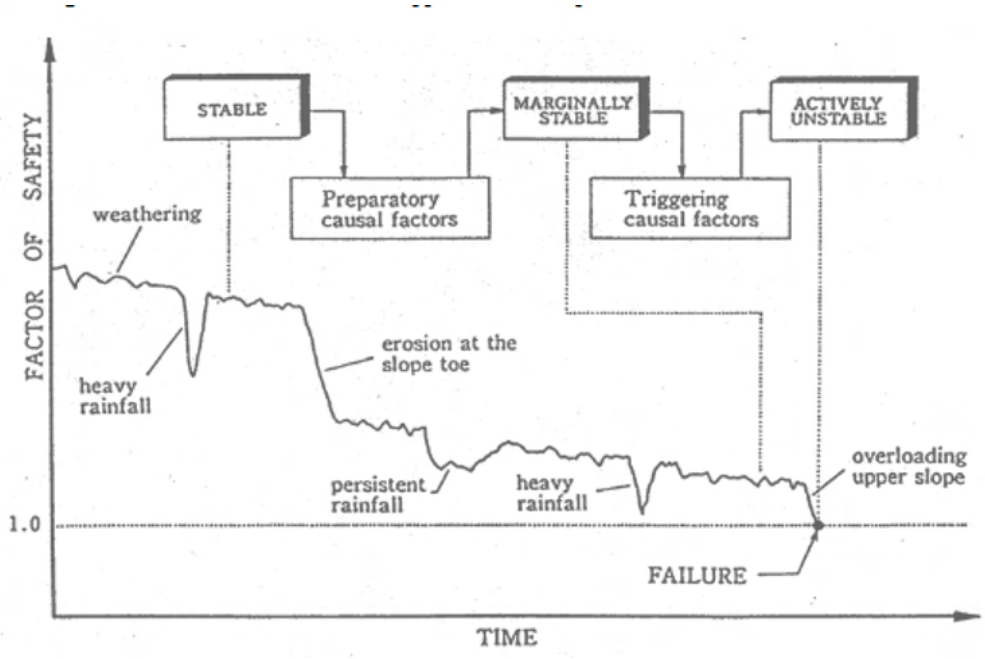

Figure 2.14: Factor of safety shows the evaluation of slope on time scale and processes which occur in this time (Mihail E. Popescu, 2002)

The lithology of rock also influences its susceptibility to failure and resistance to erosional processes, including its strain behaviour under shear forces and thermal deformation characteristics (Dikau et al., 2019).

In sedimentary rock structures, the orientation of bedding planes is very important. These planes represent natural weaknesses that may act as slip horizons for mass movement processes (Stead and Wolter, 2015). In igneous rocks (or magmatic rocks), fault zones are often the weakest zones. Groundwater flow and pore pressure are the main controlling factors of slope stability in igneous rocks (Stead and Wolter, 2015).

In metamorphic rock slopes, foliations, cleavage and other deformational features often act as weak zones(Agliardi et al., 2001; Stead and Wolter, 2015). Many slope failures have been observed in metamorphic rocks ranging from gneiss to phyllites and schist (Stead and Wolter, 2015). The age of the geological structure is also important, particularly in metamorphic rocks where strength decreases over time (Stead and Wolter, 2015). Generally, with more fractures and discontinuities, rocks lose strength and become more vulnerable to water infiltration. This leads to instability through physical erosion, such as freeze-thaw processes and increased pore pressure, which creates additional stress on the rock mass and may reduce the factor of safety (Ambrosi and Crosta, 2011; Hoek et al., 2000; Stead and Wolter, 2015). This is illustrated by the Geological Strength Index for jointed rocks as described in fig. 2.15.

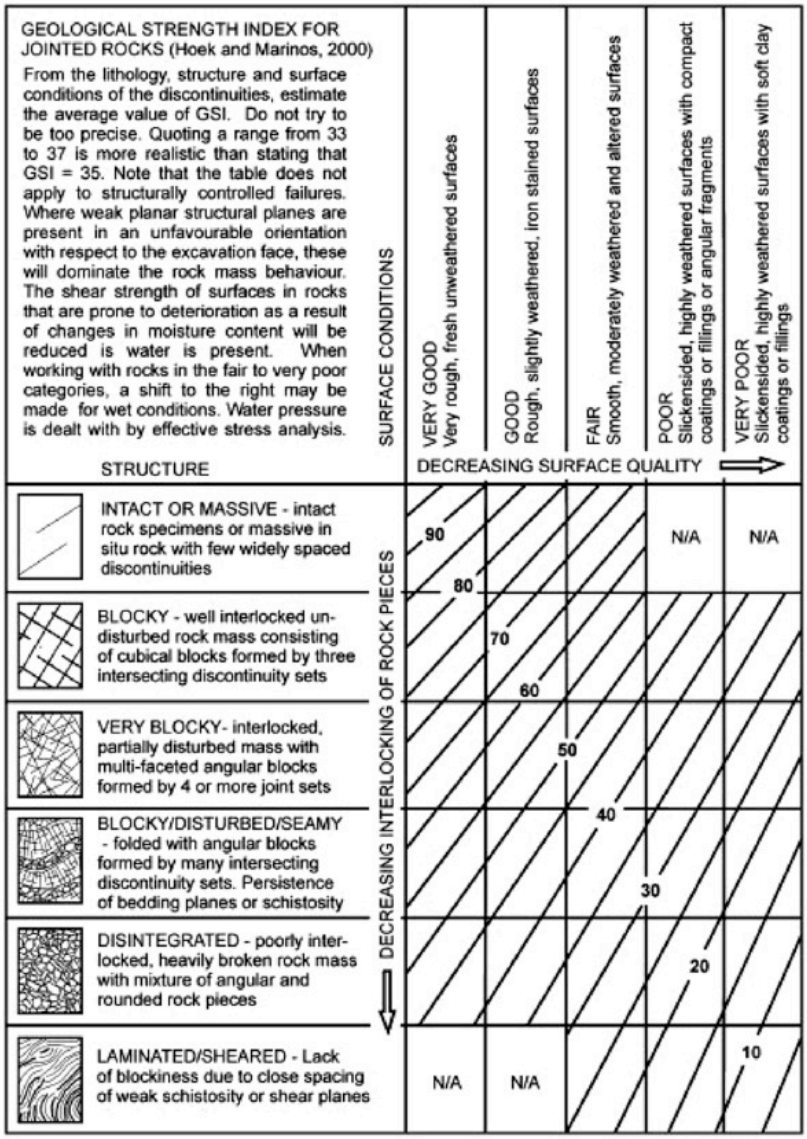

Figure 2.15: Geological Strength Index (GSI) chart, based on block size and joint condition (Hoek et al., 2000)

Study site

3.1 Findel valley and glacier



(a) Findel Glacier in 1990 (WGMS, 2025)



(b) Findel Glacier in 2025 (Michael Czaderski)

Figure 3.1: Findel Glacier comparison 1990–2025

The Findel Glacier (see fig. 3.1), or Findelen glacier, is located in the Matter Valley. In 2015, the glacier had an area of 13.87 km² (GLAMOS, 2026). The tongue reached an elevation of 2624 m a.s.l. and stretched to 3468 m a.s.l. at its highest point (WGMS, 2025). The glacier lies north of the Monte Rosa massif. The Weisshorn ridge forms a natural border to the east and towards Italy. It has one of the highest equilibrium lines of any glacier in the Alps. The glacier is situated in a continental climate (WGMS, 2025).

The Findel Glacier has shown an overall retreating trend since the early 1920s (fig. 3.2). However, there are some data gaps before 1956. The retreating trend over the last 20 years shows an even stronger decrease in length and mass (fig. 3.3). This results in a total length reduction of the glacier by 2500 m over the last century (GLAMOS, 2026; WGMS, 2025). However, there were some small advances in the 1980s due to global dimming (Martin Wild et al., 2007). Since the 1990s, the Adler glacier has no longer been connected to the Findel Glacier (swisstopo, 2026; GLAMOS, 2026).

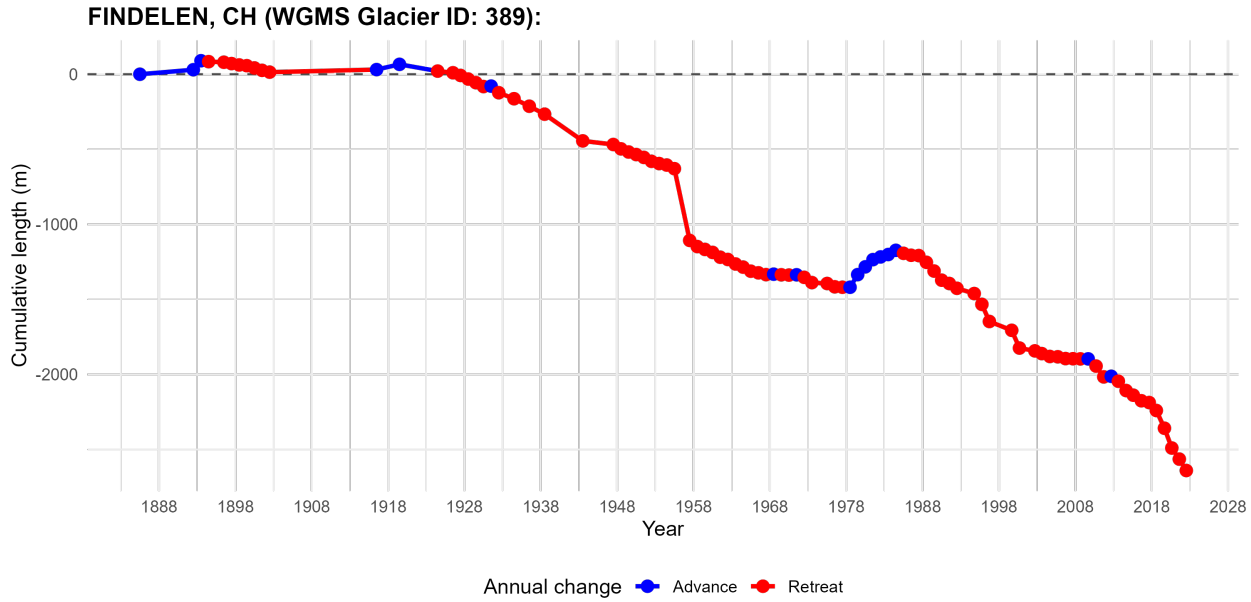

Figure 3.2: Findel Glacier cumulative length changes over the last century measured by GLAMOS (2026) and published by WGMS (2025)

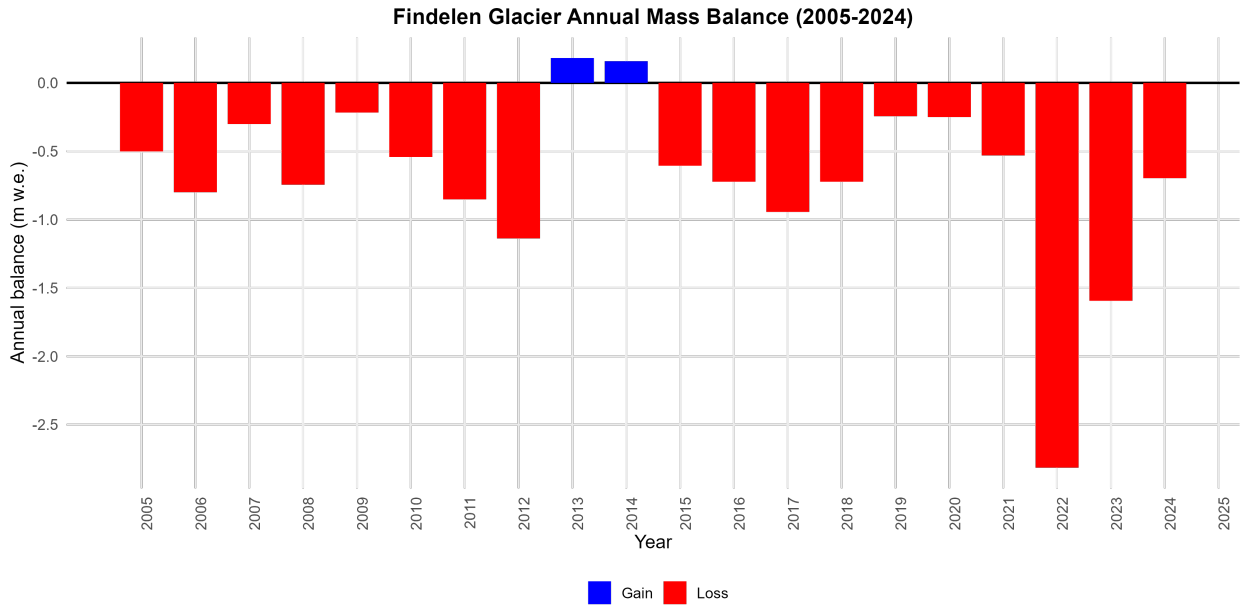

Figure 3.3: Findel Glacier mass balance (glaciological method) over the last 20 years measured by GLAMOS (2026) and published by WGMS (2025)

The Findel Glacier has one of the tallest moraines in the Alps. The glacier itself has a gentle and uniform surface gradient of approximately 14° (GLAMOS, 2026).

The Findel Glacier is one of the 80 glaciers monitored by the VAW (Research Institute for Hydraulic Engineering, Hydrology and Glaciology) as part of the glacier hazard monitoring program. The inventory was established to ensure good data coverage over longer time

ranges. With this data, periodic risk management and assessment of the situation can be performed. Early detection of dangerous changes allows the risk to be re-evaluated and appropriate measures to be taken to prevent hazards (Mélanie Raymond et al., 2003). In the case of the Findel Glacier, the two main hazards are changes in length and geometry and the triggering of floods. At the moment, the Findel Glacier has a relatively stable geometry, but during a short period in the 1980s, the glacier re-advanced almost to the water storage facility. The facility was relocated earlier due to the potential threat posed by the advancing glacier. Eventually, the advance stopped before reaching the facility. In 1982, a subglacial lake triggered a flood which damaged the construction site of the new water storage facility. Since then, no major events have occurred at the Findel Glacier (Mélanie Raymond et al., 2003). Most glacial hazards occur during advance phases. During the last 30 years, most glaciers have been retreating, which has reduced direct glacial risks. However, the threat of a glacial lake outburst flood (GLOF) or a glacial flood cannot be ruled out. GLOF events are becoming more probable as many glacial lakes are dammed by unstable material (Ma et al., 2021; Mölg et al., 2021; Mélanie Raymond et al., 2003).

3.2 Slopes

For the assessment of mass movement processes, two sites with detectable changes over the study period were selected. One is the Innere Rimpifschwäng slope (IR), which showed many changes over the study period (fig. 3.4), and the other was the Tripfen slope, where a previously studied rockslide took place. For the assessment of the full area, only the years until 2021 were considered, since in the last 3 years the data collection was not capturing the whole IR slope, but more details about data quality in section 4.1.

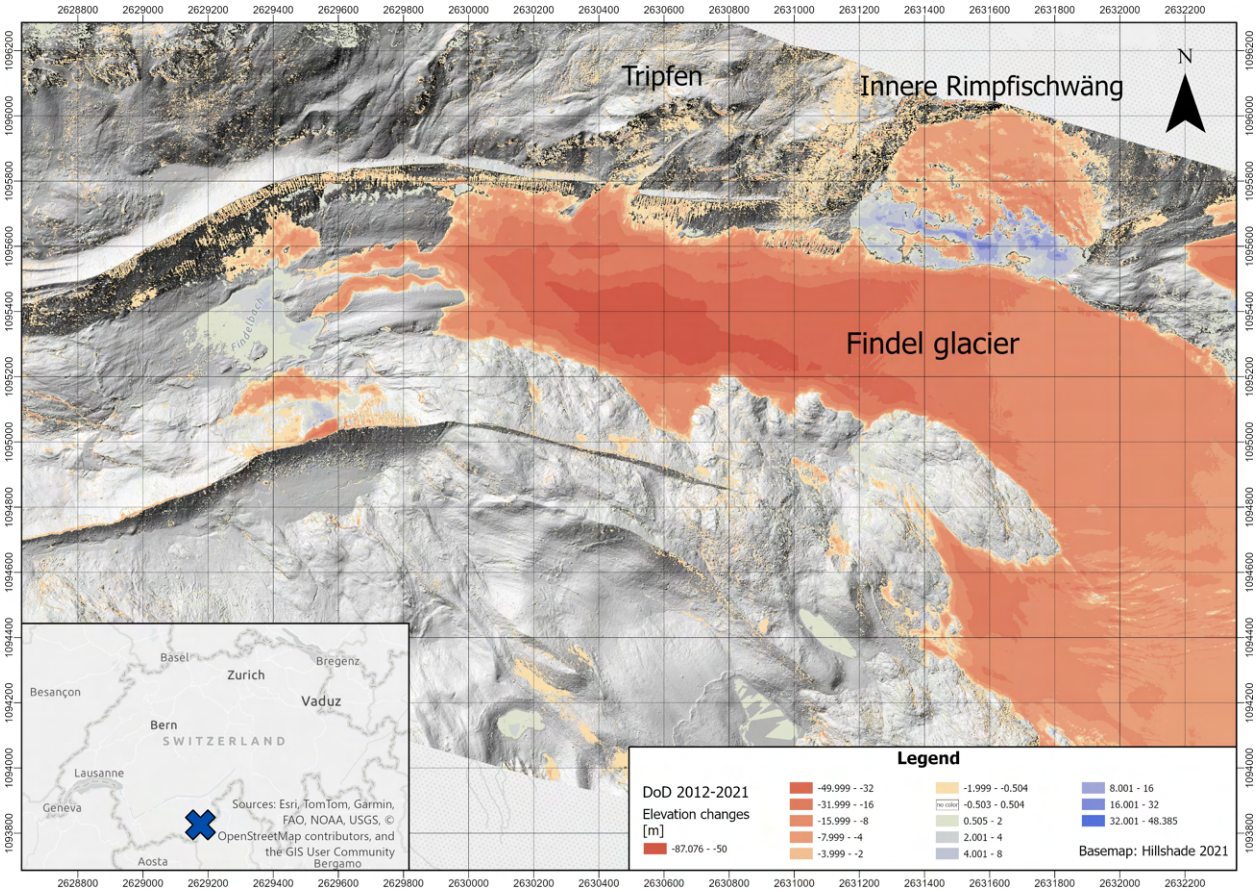

Figure 3.4: Elevation changes (DoD 2012–2021) across the Findel Glacier and its margins. Negative values (red) indicate surface lowering dominated by glacier thinning, reaching up to −87 m on the glacier tongue. Positive values (blue) reflect local accumulation. The two study slopes (Tripfen and Innere Rimpfischwäng) are labelled.

Figure 3.4 shows that the glacier lost a tremendous amount of ice over the period between 2012 and 2021, thereby exposing many new surfaces to the atmosphere. The moraine and glacial forefield, on the other hand, were rather stable. Despite the fine to coarse heterogeneous material, the moraine remained largely unchanged, with material loss occurring only at the ridge within the gully. In the floodplain, material was accumulated through fluvial processes. Around the glacier and beyond the moraine walls, the slopes showed different behaviours. At the Innere Rimpfischwäng (IR) and the Tripfen slope, many changes can be observed (see fig. 3.4). In contrast, the opposite valley side showed only minor changes. The proglacial lakes expanded over the study period, with visible yearly variations in the elevation change (fig. 3.4), but receded to the background due to the retreat of the glacier.

3.2.1 Innere Rimpfischwäng slope

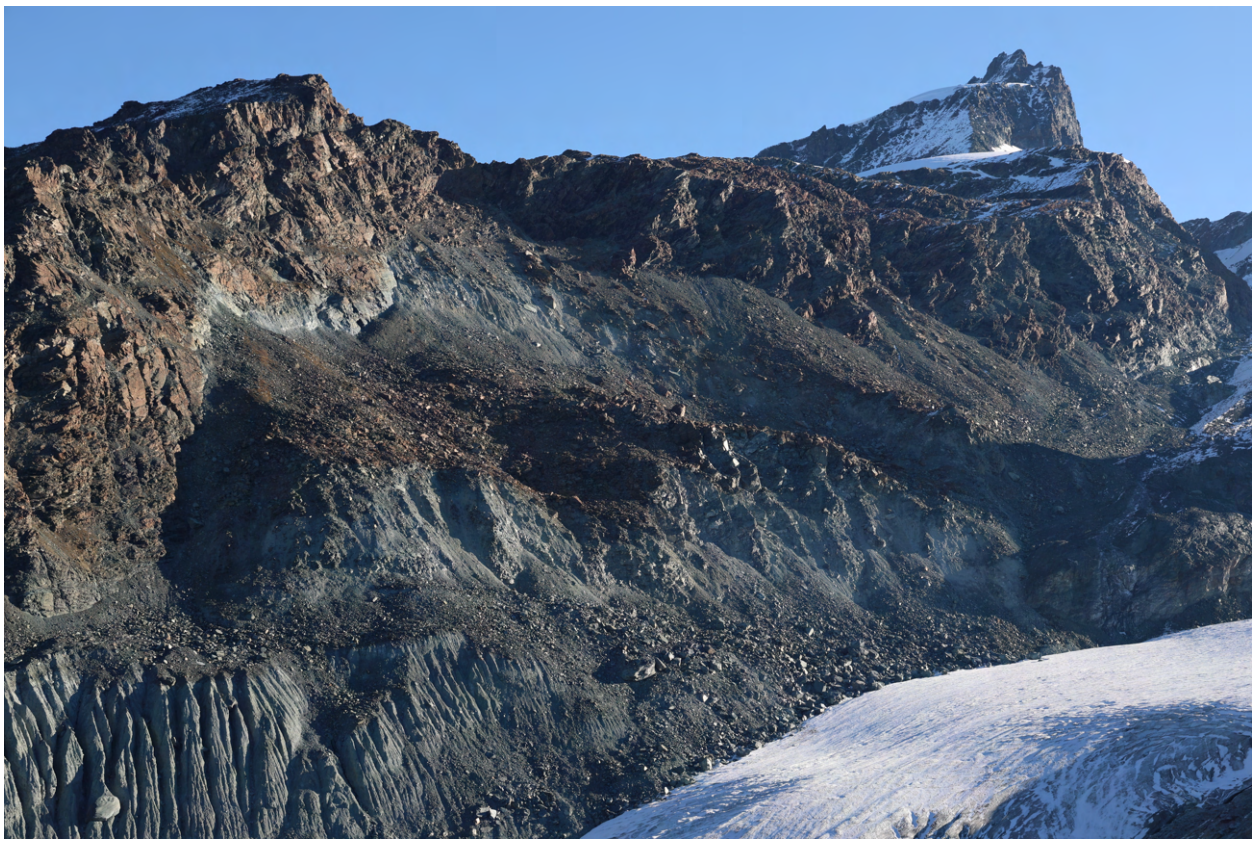

Figure 3.5: Aerial view of the Innere Rimpfischwäng slope in late September 2025 (field observation).

As the IR slope is the most dominantly changing slope in the area, it was selected for a detailed analysis of geomorphological changes. This will be compared to the already documented rockslide at the Tripfen slope, which breached the moraine. In section 5.3 and section 5.4, both vertical and horizontal changes will be assessed. The Innere Rimpfischwäng slope is located near the confluence of the Alder with the Findel Glacier (fig. 3.5). As mentioned in section 3.1, the two glaciers have not been connected since the 1990s. The slope head predominantly consists of unconsolidated material that was most likely accumulated from the steep rock walls above (see fig. 3.5). In fig. 3.6, the slope extent is shown more closely. It is adjacent to the glacier for 600 meters and ranges from an elevation of 2800 m.as.l. to 3250 m.a.s.l. It is a south-west-facing slope. The scarp could be identified, which can be seen in results sections 5.3 and 5.4.

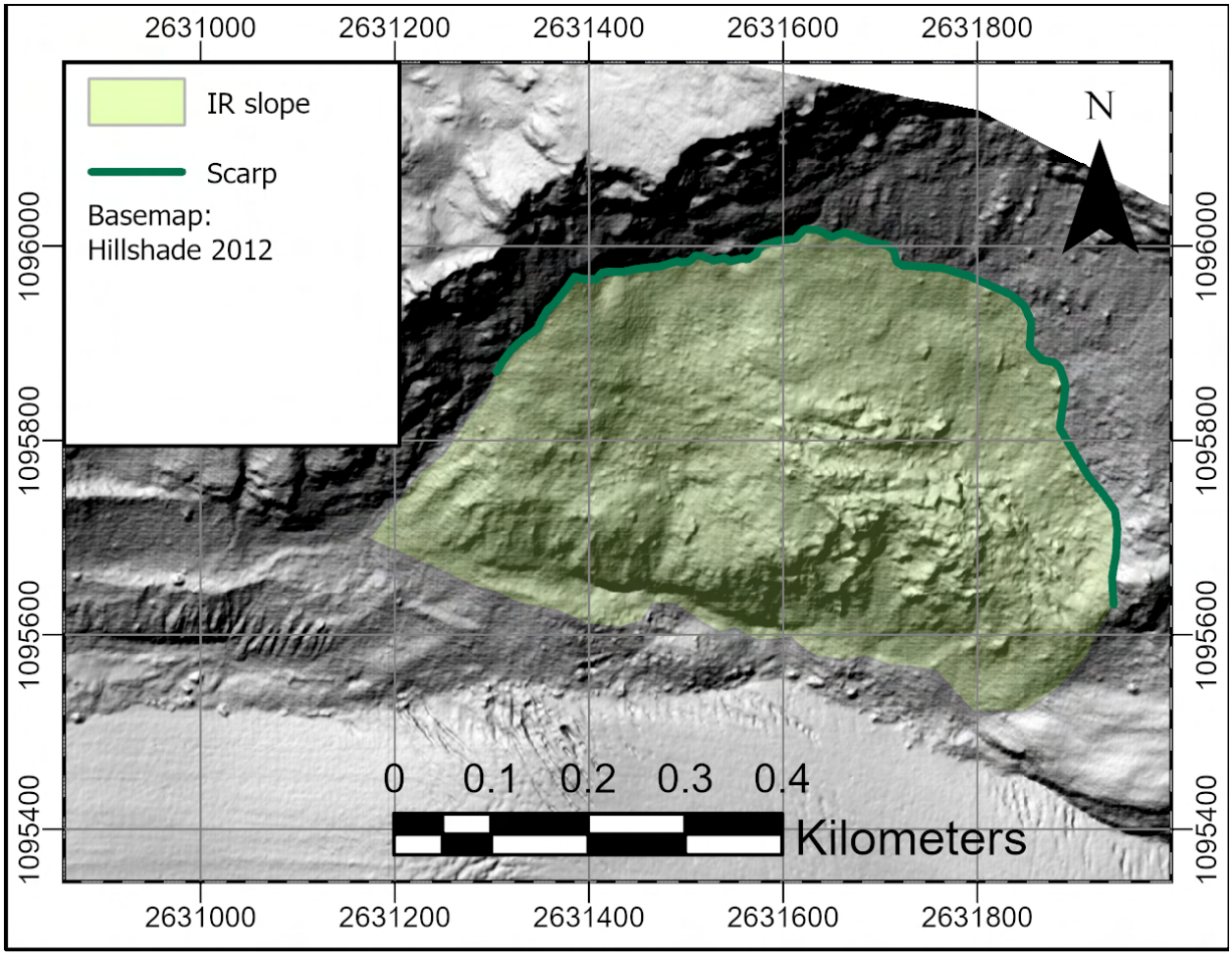

Figure 3.6: Innere Rimpfischwäng slope extent and scarp at the slope head. Spatial extent of the Innere Rimpfischwäng (IR) slope (green polygon) and scarp (dark green). The scarp marks the upper boundary of the unstable slope body.

3.2.2 Tripfen slope

The Tripfen slope is further downward (fig. 3.7). The slope is supported by steep moraines, and nowadays a glacier lake is location at the proglacial zone of the Findel Glacier. A rock slide once breached the moraine and now reaches into the glacier lake.

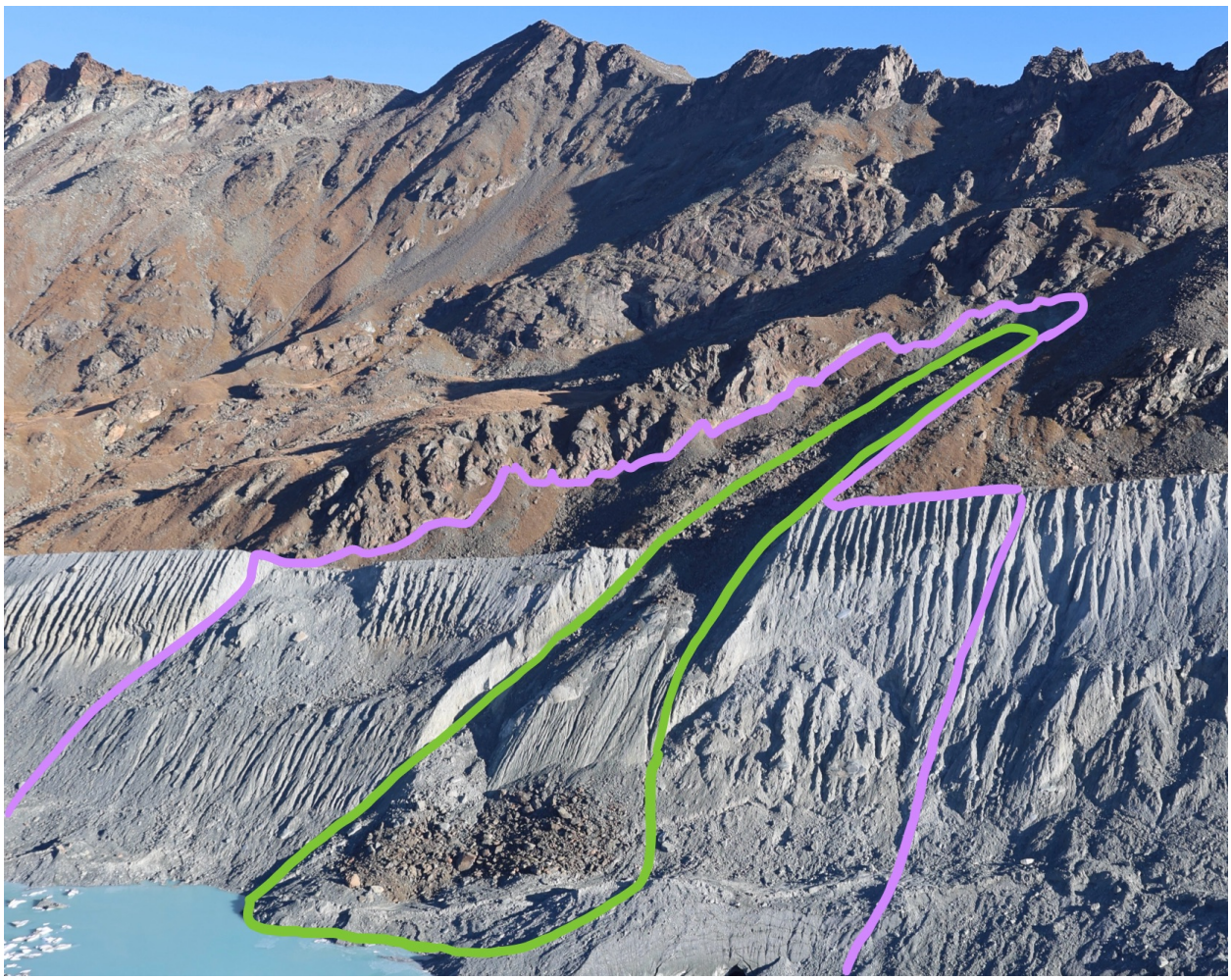

Figure 3.7: Tripfen slope in 2025 from field observation (Michael Czaderski). The rockslide (green) migrated over the years (breached the moraine and reached the valley floor). The Tripfen area is marked in violet.

The Tripfen slope extent (shown in fig. 3.8) is also a south-west-facing slope. It ranges from 2600 m.a.s.l (glacier lake) to 2900 m.a.s.l. (slope crown). A 400-meter-long moraine section divides the slope from the glacier.

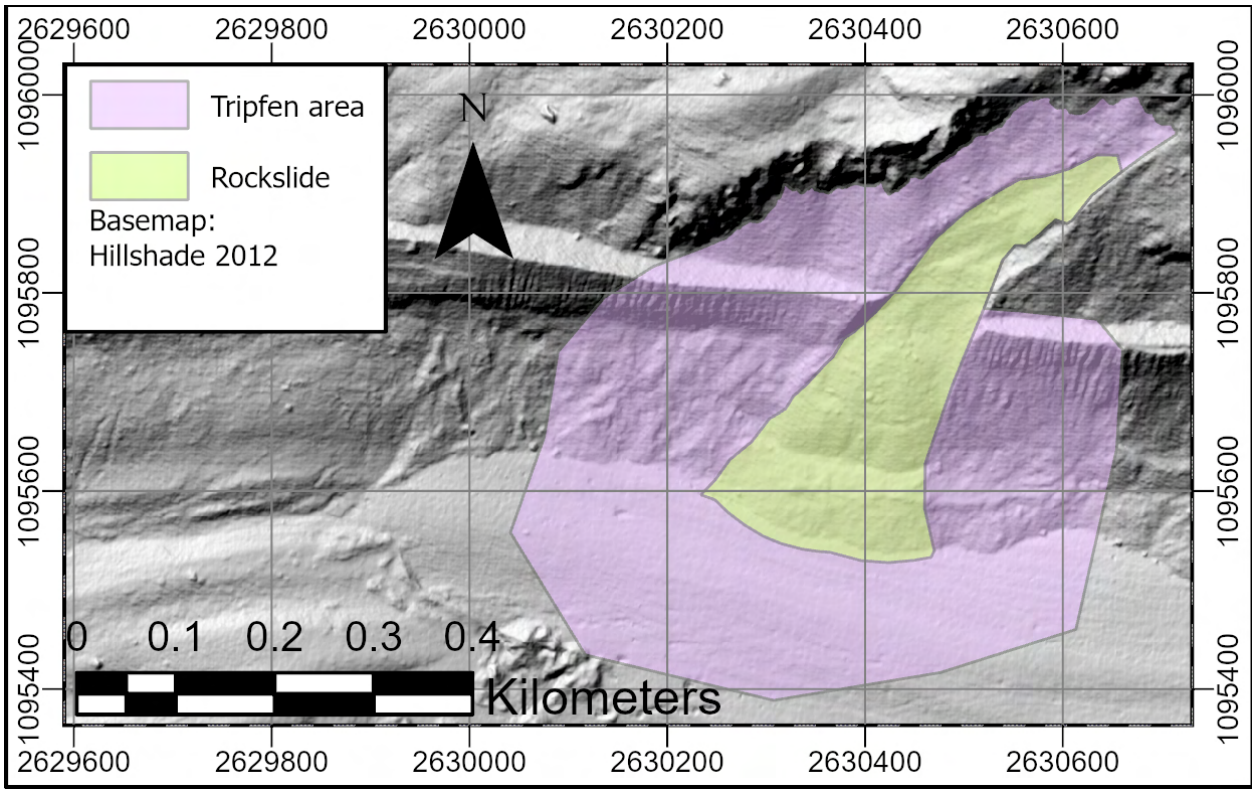

Figure 3.8: Tripfen slope extent in 2012 (purple), limited by the steep rock wall at the top and a buffer around the rockslide body (green/yellowish) at the bottom.

3.2.3 Geology at study slopes

All information derived from this section originates from the Geological Atlas of Switzerland (Bearth, 1953) and is shown in fig. 3.9. The geological setting of the Findel Glacier consists of two tectonic units: the Monte Rosa nappe and the Zermatt-Saas ophiolite zone (ZSZ) (Bucher et al., 2020). Both units are part of the Penninic domain, which underlies most of the Valais mountains. At the study slopes, only the ZSZ is present. This geological unit was once oceanic crust, which was subsequently subducted, leading to an initial phase of eclogite-facies metamorphism. During the Alpine orogeny, folding and stacking with adjacent nappes resulted in high- to ultra-high-pressure metamorphism. The characteristic rocks of the ZSZ that have formed under these conditions are eclogite and serpentinite (fig. 3.9). Eclogite originates from basaltic oceanic crust (mid-ocean ridge basalt), while serpentinite is derived from the underlying oceanic mantle peridotite. Both were part of the former Tethys ocean floor before the subduction and metamorphism happened. Serpentinite appears dark green in fresh outcrops and develops a rusty-brown weathering surface due to

oxidation of iron-bearing minerals. Eclogite is also greenish in colour, distinguished by its red garnet porphyroblasts set in a green omphacite matrix (fig. 3.9). In addition to the bedrock, numerous rockfall cones and debris accumulations can be found at many north- to northwest-facing rock walls (fig. 3.9). These rockfall cones represent persistent geomorphic features that remain preserved over longer timescales, even after many rockfall events (Shroder, 2013).

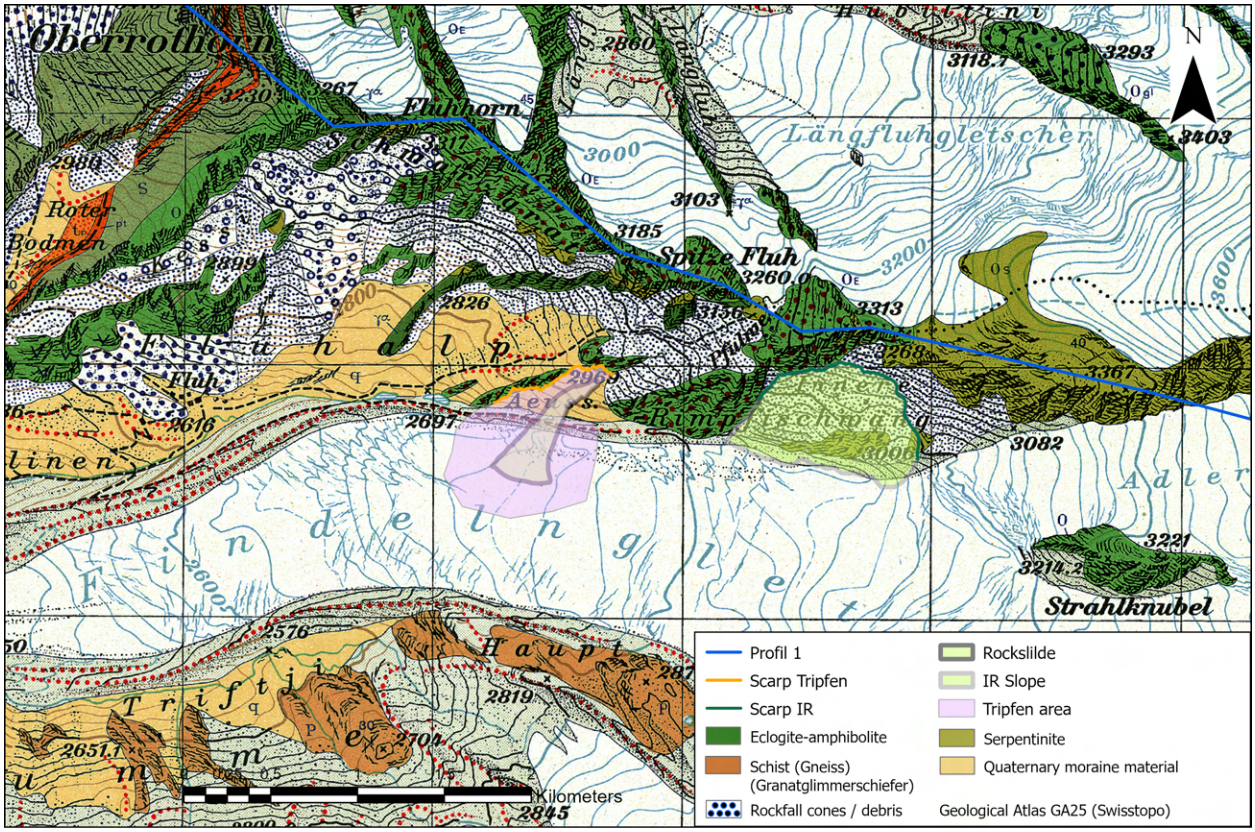

Figure 3.9: Geological overview of the Findel Glacier forefield and adjacent slopes, based on the Geological Atlas of Switzerland (Bearth, 1953). The two study slopes are the Innere Rimpfischwäng (IR) slope (light green) and the Tripfen slope (violet). The bedrock lithologies are eclogite-amphibolite (dark green) and serpentinite (olive-brown) and schist (gneiss, brown). Quaternary moraine material (beige) covers large parts of the margins of the glacier. Rockfalls, cones and debris accumulations are widespread along the valley flanks. Profile 1 (blue line) indicates the cross-sectional transect used for structural analysis (fig. 6.2).

At the slope head of the IR slope, a large amount of unconsolidated material had accumulated over time from the surrounding rock walls (seen in fig. 3.10). Features of the characteristic rusty weathering surface of serpentinite are visible at the slope toe on the right side. It is unclear whether this represents a previous rock face collapse or a larger rockfall/topple event. The structure is older than the Dufour maps. Along the mountain crest and down the slope, the two ophiolite formations, the eclogite and the serpentinite, come together. The scarp lies along this contact between the two rock formations (seen in figs. 3.10 and 6.2). It is unclear whether a fracture surface exists below the unconsolidated material, but it appears possible that at the interface between these two formations, shear strength

is lower compared to a single lithology. The scarp at the Tripfen slope also follows the rock wall of the bedrock between the quaternary moraine material and the eclogite-amphibolite (see fig. 3.10).

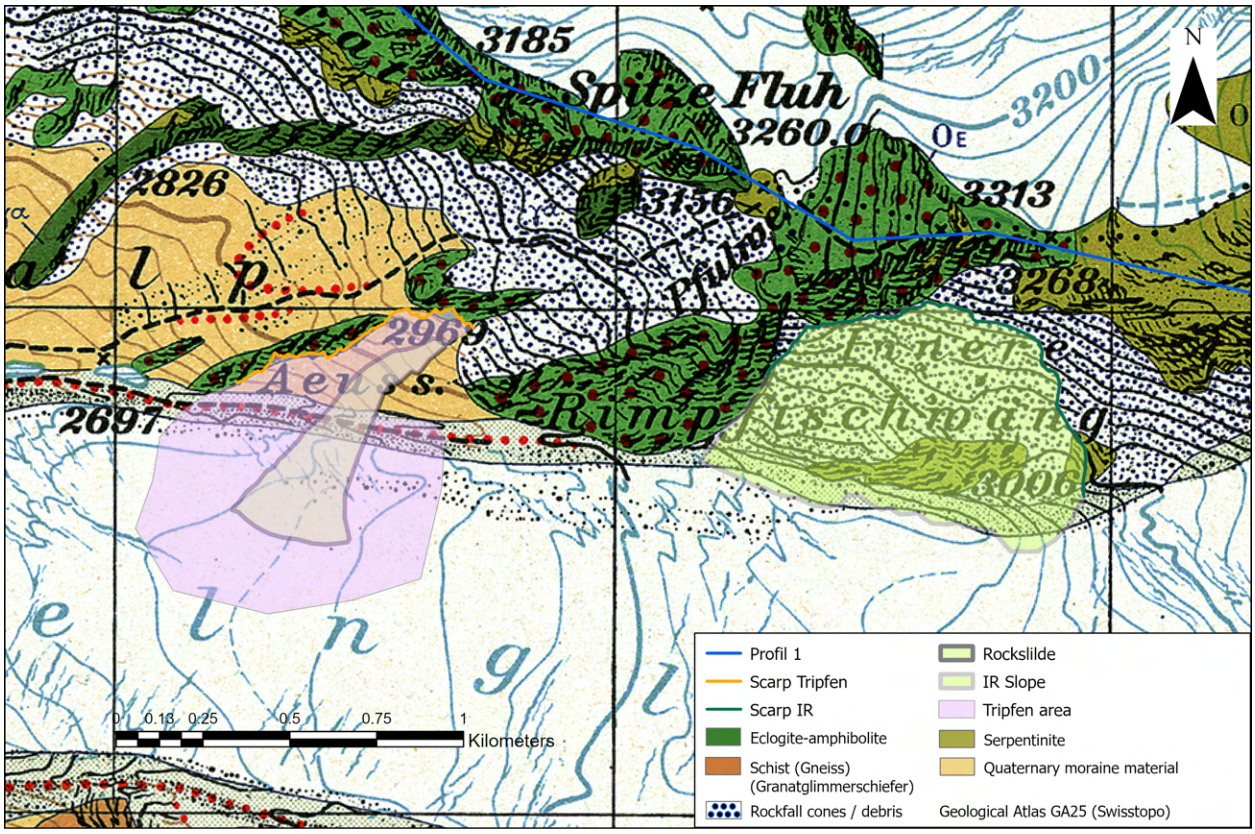

Figure 3.10: Detailed geological overview of the two study slopes overlaid on the Geological Atlas of Switzerland (GA25, Swisstopo, scale 1:12 500). The two main bedrock lithologies are eclogite-amphibolite (dark green) and serpentinite (olive-brown). Quaternary moraine material (beige) covers the slope of the Tripfen slope where the rockslide originated.

The original rockslide material consists of Quaternary moraine deposits from the previous ice ages. The glacier deposited this material laterally when its thickness was considerably greater than today. This material predates the Rockfall cones located further up slope. There are many areas showing vegetation such as grass, indicating that rockfall activity is less frequent here than at other locations. On top of this quaternary moraine material, many large boulders are present, presumably originating from eclogite rockfalls above. Notably, the scarp originates at a similar geological interface between the eclogite and the Quaternary moraine material (Bearth, 1953).

Methods

This chapter presents the methods used to address the research questions and outlines the associated uncertainties.

4.1 Data

The Swiss glacier monitoring service GLAMOS measures and researches glaciers. It collaborates with the Swiss Committee on Cryosphere Observations (SKK), the Academy of Natural Sciences, the VAW (Versuchsanstalt für Wasserbau, Hydrologie und Glaziologie at ETH Zurich), the Geosciences Department of the University of Fribourg, and the Geography Department of the University of Zurich. GLAMOS is funded by the Swiss Federal Office for the Environment (BAFU), MeteoSchweiz, and SCNAT. The VAW maintains a dedicated inventory for hazardous glaciers, as mentioned in section 3.1. For the aerial imagery, the VAW engaged Swisstopo, the Swiss Federal Office of Topography (Bundesamt für Landestopografie swisstopo, 2024), to collect the data.

The VAW provided the dataset used in this thesis which contains high-resolution airborne digital imagery (Airborne Laserscanner, ALS) of the Findel Glacier covering the period 2012–2024. The raster data contains a set of digital orthophotos (DOP) and digital surface models (DSM) for each year. These two products were used to quantify the evolution and movement of the glacier and the geomorphological changes on the surrounding slopes. Table 4.1 provides a comprehensive overview of the datasets. The images were acquired at the end of summer using the Leica ADS100 camera and ADS80 sensors (Leica Geosystems AG, 2025).

Year	Flight Date	DSM Resolution	DOP Resolution	Comments
2012	2012-09-14	1.0 m	0.25 m	
2013	2013-08-20	1.0 m	0.25 m	
2014	2014-08-27	1.0 m	0.25 m	
2015	2015-08-05	1.0 m	0.25 m	
2016	2016-08-26	1.0 m	0.25 m	
2017	2017-10-05	0.5 m	0.25 m	
2018	2018-09-11	1.0 m	0.1 m	swissALTI3D
2019	2019-09-03	0.5 m	0.1 m	
2020	2020-08-21	0.5 m	0.1 m	
2021	2021-08-14	0.5 m	0.1 m	
2022	2022-07-15	0.5 m	0.1 m	
2023	2023-08-21	0.5 m	0.1 m	
2024	2024-08-20	0.5 m	0.1 m	

Table 4.1: DSM and DOP dataset acquisition details for Findel Glacier (2012–2024). swissALTI3D was used for the DSM in 2018.

For the second research question, external factors were analysed. All data used for this purpose is openly available from various repositories. Geological and permafrost data were obtained from Swisstopo (Bundesamt für Umwelt BAFU, 2024; BAFU, 2011). The geological atlas is a vector dataset which was not frequently updated. The permafrost model contains, as its main input, ground temperature data. This is not always measured directly, and often just modelled; hence, these maps need to be carefully analysed. PERMOS (2026) has a monitoring network with boreholes, which are very valuable to verify permafrost conditions. These measurements are very expensive and time-consuming to manage. Hence, maps are only an estimate of where permafrost could be present. In situ measurements are needed to validate these maps and to be certain about the permafrost conditions. But they give a good indication if we could have permafrost-related processes acting on mass movement processes. Meteorological data from the MeteoSchweiz measurement network (MeteoSchweiz, 2026), including stations at Gornergrat and Findelen, were used for precipitation, temperature, wind, and duration of sunshine. The temperature is measured two meters above ground. The Findel station only contains data from 2011 onwards. The resolution was daily, but for the purpose of comparing monthly means or even the sum of the year was extracted. The Gornergrad station has a longer timeseries and as year measurement since 1923. For comparison to the images, years were calculated by the time span of September 20XX-August 20XX + 1, since over the whole time period, this was the best match (image acquisition was from July to September seen in table 4.1).

The temperature measurement device at Gornergrat is located at 3129 m.a.s.l. To interpolate temperatures for the study sites, which are located at elevations of 2700–3050 m a.s.l., a constant temperature lapse rate of 0.65°C per 100 metres was applied, based on (MeteoSchweiz, 2026). Accordingly, the estimated temperature at the IR slope is approx-

imately 1.3°C warmer and at the Tripfen slope (2550–2800 m.a.s.l.) approximately 2.6°C warmer than at the Gornergrat station.

4.2 Pre-processing and uncertainty

The entire processing and subsequent analysis were made with ArcGIS PRO Version 3.5.2 (Esri, 2025) and QGIS 3.40 Bratislava (QGIS, 2025). Figures and statistics were produced using RStudio (Version 2023.03.0+386 "Cherry Blossom") (RStudio, 2025) and Spyder IDE 5.4.3 (conda) (Spyder Project Contributors, 2009). Data extraction from Imagary data (velocities, elevation transect, feature tracking, etc.) was stored and managed in CSV format using Microsoft Excel.

4.2.1 Pre-processing

In the ALS imagery datasets, pre-processing was needed to homogenise the data (Yan and Shaker, 2018). In remote sensing data, artefacts are a common source of error. Artefacts can result from steep terrain, where the light signal is back-scattered unevenly (Bollmann et al., 2011; Yan et al., 2017). Further, if the flight height is at a low altitude, areas in the shadow of ridges or hills cannot be scanned, resulting in data gaps and artefacts (Yan, 2023). Furthermore, sensor errors can also lead to artefacts. All of these issues can be corrected to a certain degree with filters and algorithms (Kääb, 2002; Nuth and Kääb, 2011; Yan and Shaker, 2018; Yan, 2023). The co-registration, which was used for the data, could not eliminate all the artefacts in the images.

When comparing remote sensing datasets, they must share the same coordinate system. All DSMs were already in the reference system (CH1903+ LV95/LN02) and did not require a reprojection. For the DOP datasets, only the image acquisition of 2014 required a reprojection (table 4.1), which was performed using the ArcGIS Pro reprojection tool. Raster data requires a considerable storage capacity, which is why aerial images are often stored as smaller individual raster tiles. When large areas are analysed, they need to be merged into a single image. This process is called mosaicking (Esri, 2026a). The DSMs had already been mosaicked by Swisstopo; this step was only necessary for the DOP datasets (table 4.1). Mosaicking was performed in ArcGIS Pro using the Mosaic to New Raster tool, with settings of 8-bit unsigned, LV95 coordinate system, and pyramid and statistics calculation enabled.

Resampling is used to change the spatial resolution of raster datasets. An algorithm was used to create smaller cells with new pixel values (to match the 2024 resolution of 0.5 m pixel size). There are a variety of different resampling techniques (Nearest, Majority, Bilinear, Cubic). For this thesis, the cubic option was chosen because it's known to produce less geometric distortion than other techniques, at the cost of more processing time (Esri,

2026b). As shown in table 4.1, the DSM did not have the same spatial resolution, highlighting the need to resample and standardise the resolution. This was performed by using the xDEM Python package (Romain Hugonnet et al., 2020). This package is designed for the analysis of elevation data. It builds upon already established geospatial packages, such as Rasterio, GeoPandas, pyProj and GeoUtils.

An overview of all pre-processing steps is provided in fig. 4.1.

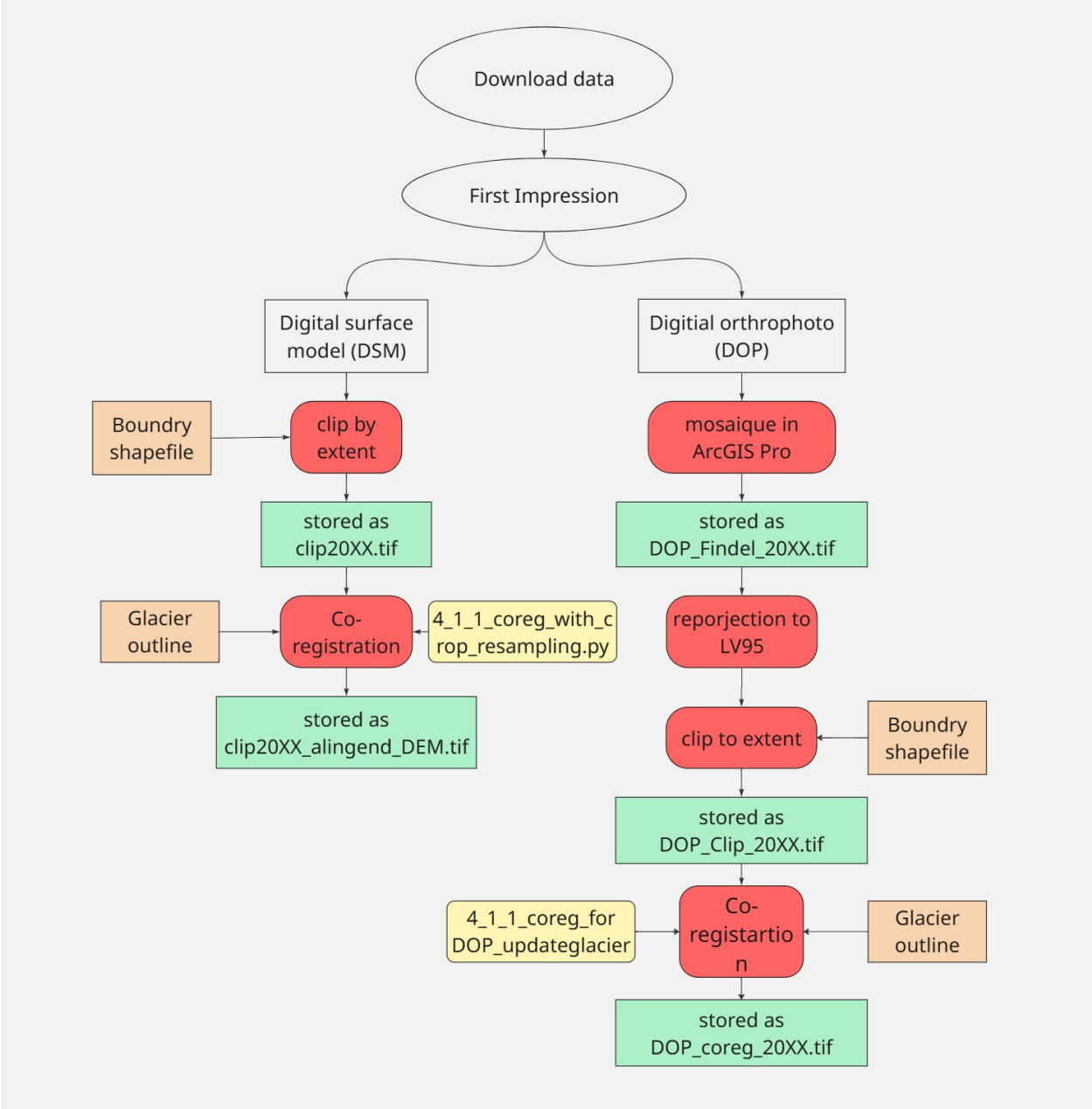

Figure 4.1: Pre-processing workflow for aerial remote sensing data for this thesis. Highlighted in green are steps, which stored the files, processes performed in ArcGIS are red, in orange are all the used shapefiles, which were needed as input and the code used to execute operations in ArcGIS is shown in yellow (created in Miro (2025)).

4.2.2 Co-registration

When comparing DEMs of the same location without co-registration, they are not perfectly aligned and produce errors in the relationship between elevation differences and terrain aspect. These errors have been documented by numerous studies (Schiefer et al., 2007; Van Niel et al., 2008). The methodology used to correct for vertical and horizontal error is called co-registration, developed by Nuth and Kääb (2011). It removes shifts in the DEM, resolves elevation-dependent biases and checks for higher-order sensor-specific errors. Figure 4.2 shows an error produced by a shifted DEM. There are many manual approaches to aligning DEMs and correcting this error. The xDEM package includes a co-registration algorithm that iteratively estimates vertical and horizontal displacement by solving the relationship between terrain orientation and elevation difference (fig. 4.2). This approach aims to improve sub-pixel 3-D alignment, though residual uncertainties may remain. Co-registration was performed by aligning each older DEM to the 2024 DEM.

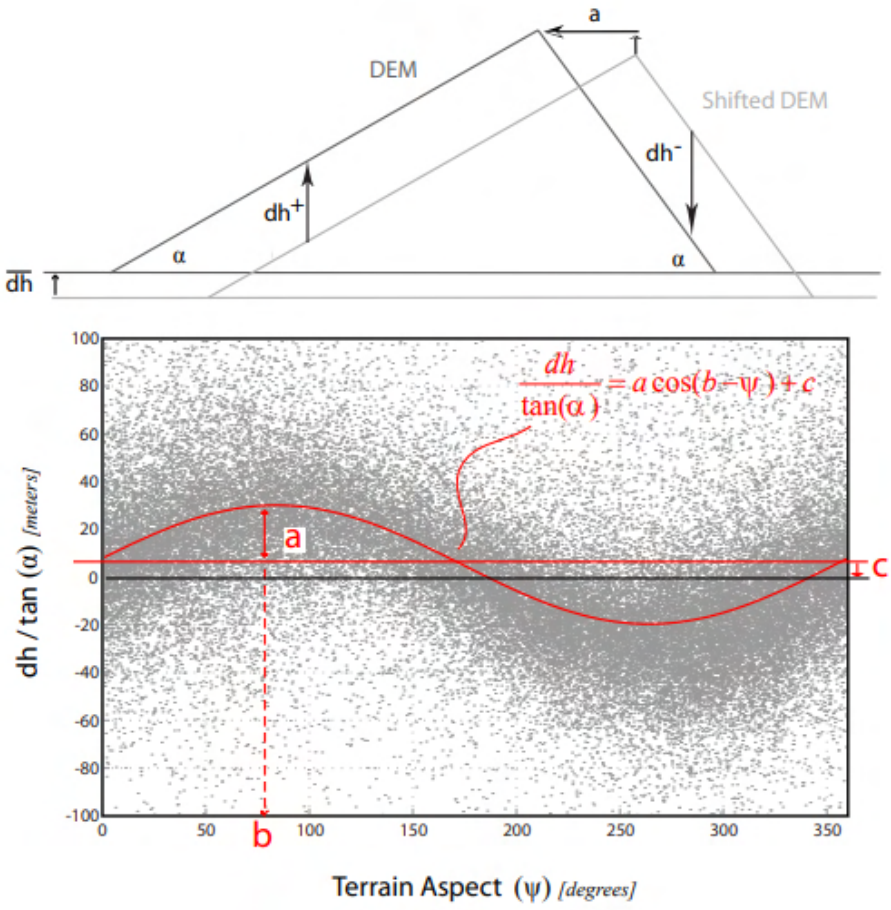

Figure 4.2: "Top: 2-D scheme of elevation differences induced by a DEM shift. Bottom: The scatter of elevation differences between 2 DEMs showing the relationship between the vertical deviations normalised by the slope tangent (y-axis) and terrain aspect (x-axis)." (Nuth and Kääb, 2011)

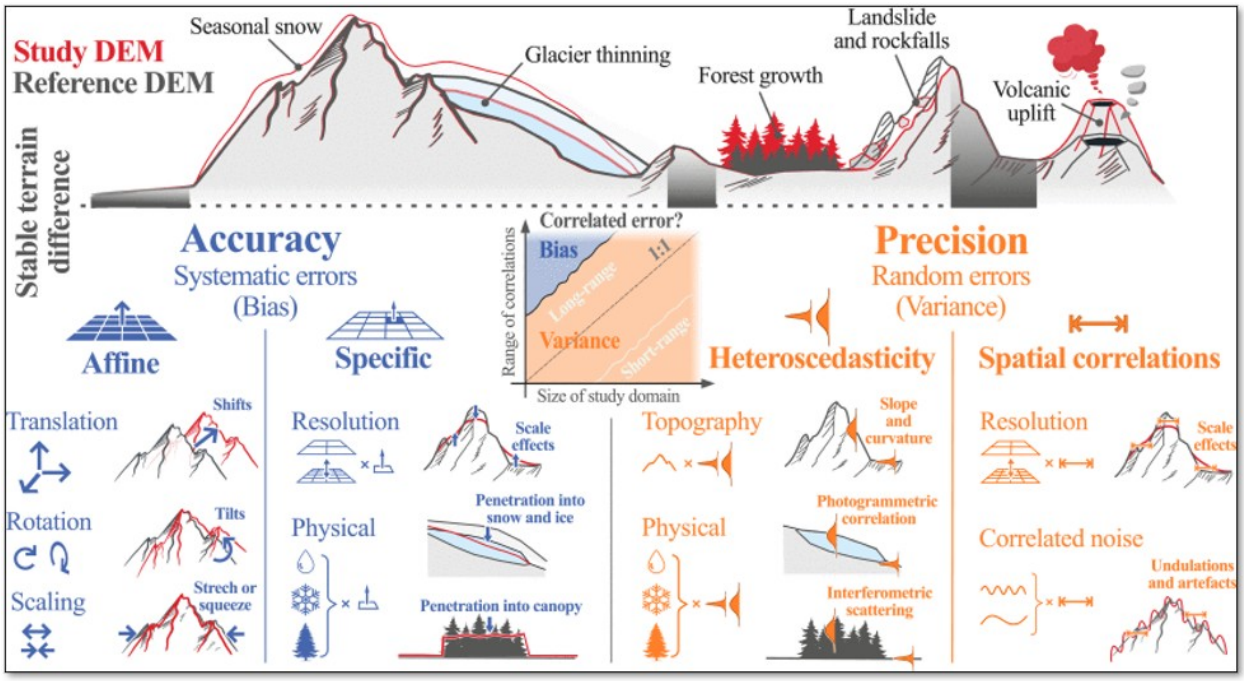

Figure 4.3: Uncertainty in digital elevation models (DEM). These can be defined as systematic errors and random errors and have various reasons (Hugonnet et al., 2022).

The mismatch of pixels and shifts is not limited to DSM; it can also occur in DOPs. Since xDEM is specifically designed for the analysis of elevation data and is therefore not applicable to DOPs, a different Python package called AROSICS was used for the co-registration of DOPs (Scheffler et al., 2017). In DOPs, the errors manifest as mismatches and shifts in the x- and y-directions.

4.2.3 Uncertainties

4.2.3.1 Uncertainties in remote sensing imagery

Uncertainty in remote sensing imagery is an important parameter. There are systematic and stochastic uncertainties. Systematic uncertainty should be minimised by pre-processing and co-registration, but stochastic uncertainty persists. The median elevation difference (MED) is used to quantify systematic uncertainty, while the Normalised Median Absolute Deviation (NMAD) is used to characterise random errors. The NMAD was used for the DSM uncertainty assessment since systematic error is minimal after co-registration. Random errors of DEMs and DSMs do not follow a normal distribution, as many errors are spatially correlated or depend on sensor characteristics or other external factors such as post-processing and filters (Höhle and Höhle, 2009; Hugonnet et al., 2022). An overview of factors contributing to random errors is shown in fig. 4.3. NMAD is a reliable estimator of DEM/DSM uncertainty and is not influenced by outliers as other measures are. NMAD, developed by Höhle and Höhle (Höhle and Höhle, 2009), is calculated as follows:

$$\text{NMAD} = 1.4826 \cdot \text{median}_j \left(|\Delta h_j - m_{\Delta h}| \right) \tag{4.1}$$

Where Δh_j is the elevation difference at a stable terrain pixel j, and $m_{\Delta h}$ is the median of all elevation differences.

The lower the NMAD, the fewer errors a dataset contains. Stable terrain is often used to investigate random errors. In the literature, stable terrain is classified as land surface that does not change in elevation over time. There are processes which take place even on stable terrain surfaces, such as erosion, short vegetation growth and continental drift, but these processes are normally smaller than the measurement accuracy and are therefore not visible in the data. Stable terrain does not change in shape, elevation or orientation over time.

The Root Mean Square Error (RMSE) is a commonly used measure of uncertainty estimation in DOPs (Höhle and Höhle, 2009; Shoab et al., 2022). It is suitable when errors follow a normal distribution (Höhle and Höhle, 2009). The RMSE is calculated as follows:

$$\text{RMSE} = \sqrt{\frac{1}{n} \sum_{i=1}^{n} \Delta h_i^2} \tag{4.2}$$

Where n is the total number of observations and Δh_i is the elevation difference at pixel i.

4.2.3.2 Uncertainty assessment

This section describes the uncertainty of the DSM and DOP images. The co-registration corrects shifts in the DSM and thereby reduces systematic errors. However, even after co-registration, the DSMs are not perfectly aligned due to actual surface changes, and residual uncertainties remain. The 2018 DSM was removed due to the fact that the recorded changes were inconsistent with plausible surface processes at the glacier and surrounding. The 2020 DOP co-registration for the IR slope appeared unreliable, likely caused by insufficient iterations in the co-registration process. The imagery for this year was therefore considered unreliable and excluded. Since in the adjacent years 2019 and 2021, almost all boulders were at nearly the same location, the movement rates between these years were assumed to be minimal. The boulder positions for 2020 were therefore linearly interpolated from the 2019 and 2021 positions.

Table 4.2 shows the statistics after co-registration over the whole study area. The more recent DSMs have lower NMAD values.

At the Findel Glacier, stable terrain is rare and only a few grasslands and visible bedrock areas fit this characteristic. A slope mask identified terrain with very low slope angles, where

Table 4.2: Co-registration performance metrics for DSM datasets (2012–2023)

	MED (m)		NMAD (m)	
Year	**Before**	**After**	**Before**	**After**
2012	3.40	0.00	0.47	0.38
2013	3.33	0.00	0.40	0.38
2014	0.07	0.00	0.44	0.35
2015	0.04	0.00	0.68	0.35
2016	0.03	0.00	0.30	0.23
2017	−0.21	0.00	0.22	0.22
2019	0.08	0.00	0.15	0.14
2020	0.11	0.00	0.18	0.17
2021	0.10	0.00	0.14	0.13
2022	0.10	0.00	0.09	0.09
2023	0.04	0.00	0.09	0.08

gravitational processes are not active. Within these flat terrain patches, areas with no nearby fluvial processes were selected (fig. 4.4).

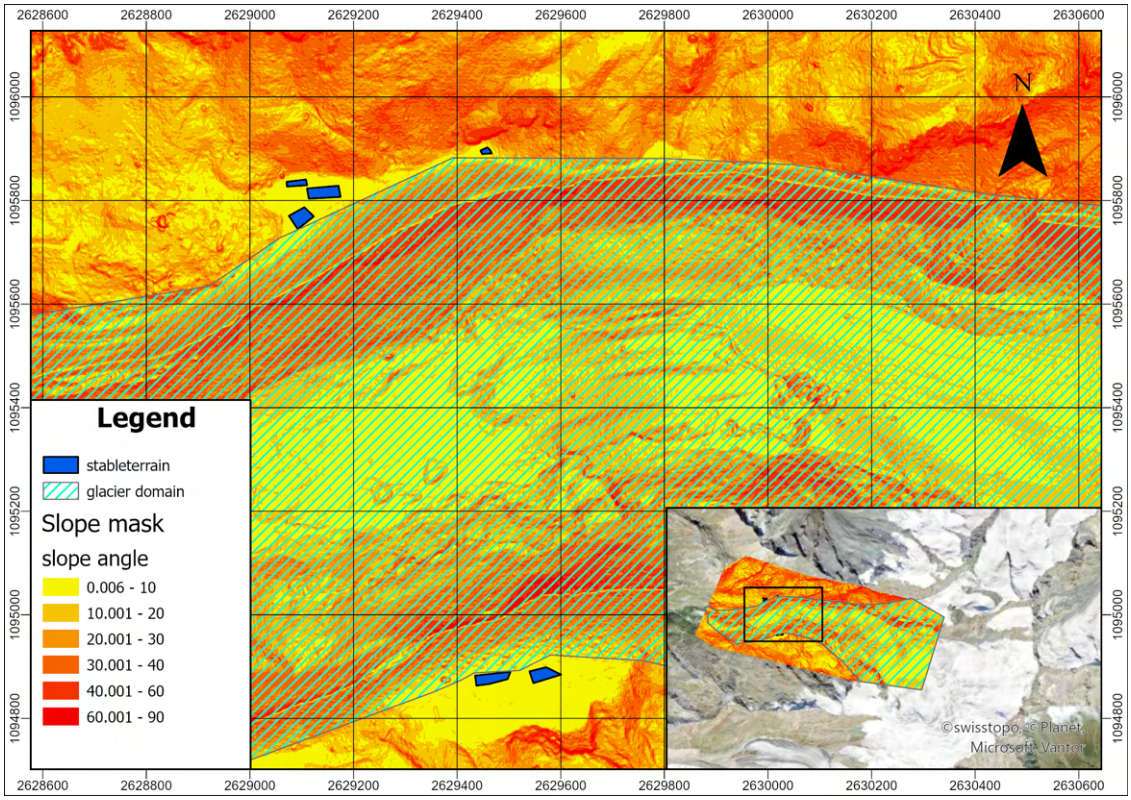

Figure 4.4: Slope mask showing the slope angle of each pixel. Only the first class (yellow) of the slope angle is referenced as flat terrain and therefore can be used for stable terrain. In blue are the chosen stable terrain polygons. The glacier domain was excluded.

On stable terrain, further investigation of random noise is shown in table 4.3.

Table 4.3: Systematic error and random error over stable terrain

Year Pair	Pixels	MED (m)	NMAD (m)
2013–2012	5,011	−0.045	0.133
2014–2013	5,011	−0.155	0.089
2015–2014	5,011	0.015	0.104
2016–2014	5,011	0.115	0.163
2017–2016	20,047	0.090	0.193
2019–2017	20,047	−0.03	0.133
2020–2019	20,047	0.145	0.185
2021–2020	20,047	−0.010	0.082
2022–2021	20,047	0.025	0.067
2023–2022	20,047	−0.045	0.052
2024–2023	20,047	0.030	0.044

The random noise, or random error, corresponding to the NMAD has a value of 0.126 ± 0.061 metres. This results in a total error range of **± 0.187 meters** over stable terrain. In steep areas, the error increases by a factor of 10 (Hugonnet et al., 2022). In their study, Hugonnet et al. (2022) used Pléiades and SPOT-6 images with resolutions of 1.7 m and 0.7 m, respectively. They suggest that with increasing slope angle, heteroscedasticity increases the error by up to a factor of 10. However, the data used in the present study is overall slightly more precise. Both studied slopes have mean slope angles of 34° and 26°, corresponding to factors of 4 and 3, respectively, according to Hugonnet et al. (2022). This means the Innere Rimpfischwäng slope has an uncertainty of **0.504 ±0.244 meters** and for the Tripfen slope **0.378 ±0.183 meters**.

Although DOPs do not have z-values, their pixels are not perfectly aligned and contain shifts in the x- and y-directions. The DOP uncertainty analysis after correction with the AROSICS package (Scheffler et al., 2017) showed that the newer DOPs have lower systematic and random errors (fig. 4.5).

$$\mathrm{RMSE}_{xy} = \sqrt{\overline{\Delta xy}^2 + \sigma_{\Delta xy}^2} \tag{4.3}$$

Where $\overline{\Delta xy}$ is the mean shift in the x- and y-directions and $\sigma_{\Delta xy}$ is the standard deviation of the shift.

The RMSE is used as the uncertainty measure for the DOPs. As shown in table 4.4, a mean remaining error of 0.1279 m was found across the full time series.

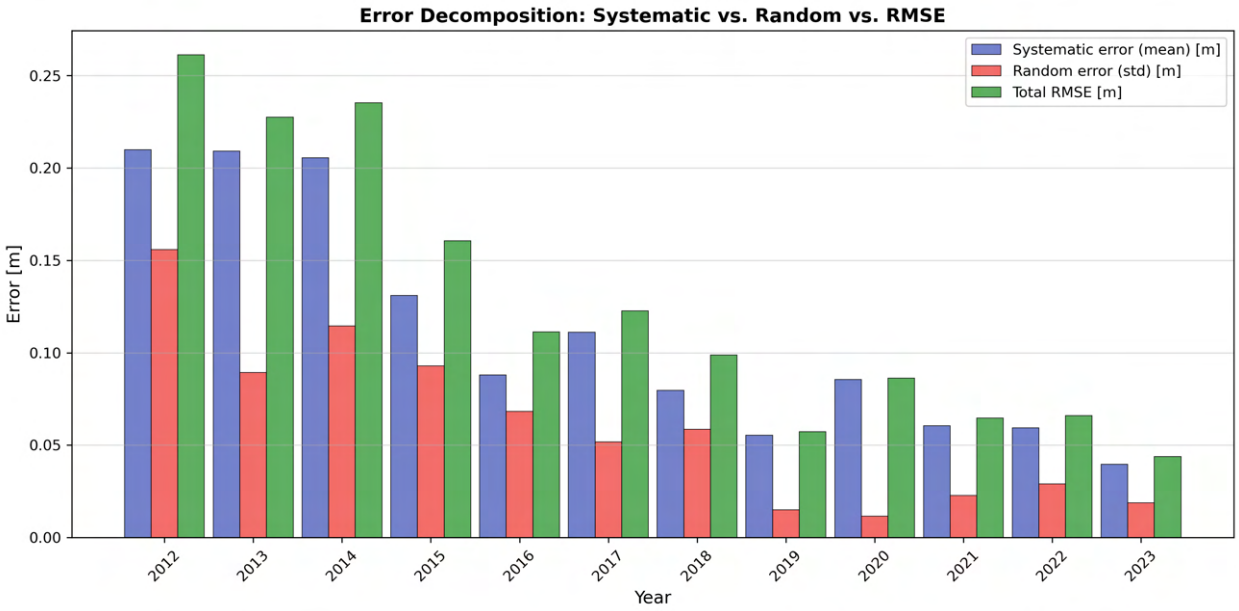

Figure 4.5: Systematic and random error and the total RMSE over the time series for DOP Images. Errors and total RMSE decrease towards newer images.

Table 4.4: Remaining DOP co-registration uncertainty relative to the 2024 DOP reference

Year	Resolution [m]	Systematic [m]	Random [m]	RMSE [m]
2012	0.25	0.2098	0.1558	0.2613
2013	0.25	0.2092	0.0894	0.2275
2014	0.25	0.2055	0.1145	0.2353
2015	0.25	0.1310	0.0929	0.1606
2016	0.25	0.0879	0.0682	0.1112
2017	0.25	0.1111	0.0518	0.1226
2018	0.10	0.0796	0.0586	0.0988
2019	0.10	0.0553	0.0149	0.0573
2020	0.25	0.0855	0.0116	0.0863
2021	0.10	0.0605	0.0227	0.0646
2022	0.10	0.0593	0.0291	0.0661
2023	0.10	0.0396	0.0187	0.0438
mean total	–	0.1112	0.0607	0.1279
mean 2012–2017	0.25	0.1591	0.0954	0.1864
mean 2018–2023	0.10	0.0633	0.0259	0.0695

systematic = mean error; random = noise; RMSE = $\sqrt{\text{mean}^2 + \text{std}^2}$

4.3 Spatial analysis

To answer the research questions, spatial analysis is needed. This analysis focuses on all the spatial aspects, like changes in elevation of the terrain, visible changes of the landscape, erosion and deposition of material. The features of the landscape might change over time.

This can be tracked. New landforms can evolve or change during the observation period. Form and velocity can be used to conclude the underlying processes.

4.3.1 Geomorphological mapping

Geomorphological mapping is a common method for analysing processes and landscape evolution. This mapping is possible through remote sensing and field observations, where geomorphic features can be mapped, and process domains can be derived (Chandler et al., 2018), as seen in fig. 4.6.

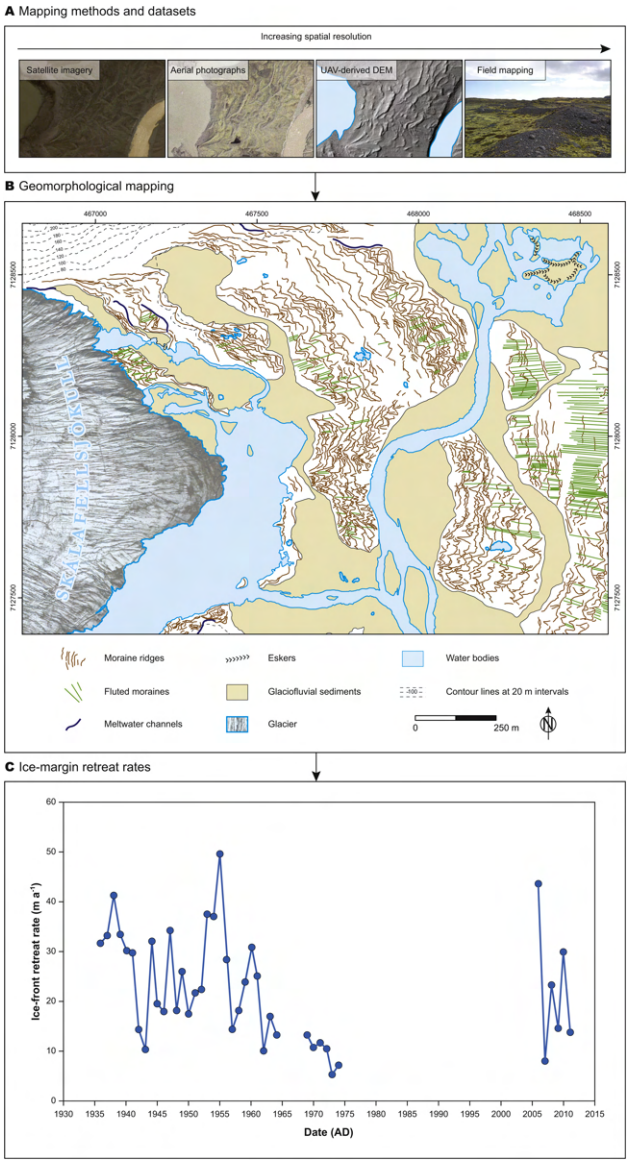

Figure 4.6: Example of geomorphological mapping of the foreland of Skálafellsjökull, from Chandler et al. (2018). A) shows the different input products that can be used for mapping; B) the resulting geomorphological map; C) the application of the map for calculating crest-to-crest moraine spacing as a proxy for ice-margin retreat rates.

In this study, the input data consisted of remote sensing data only, which is why only broad remote sensing mapping was performed. The colour scheme was selected based on a previous Master's thesis from the University of Zurich on geomorphological mapping (Alexander Ruff, 2015), with additions of specific mass movement nomenclature (Hungr et al., 2014; Church et al., 1979; Shroder, 2013; Sousa et al., 2021; Dikau et al., 2019).

The process domains were determined by slope angle and known geomorphological features associated with certain geomorphological domains. In many cases, there is an overlap of multiple processes. For certain areas, field observation is necessary to evaluate whether the estimated process domains are present or not. In particular, the periglacial process domain remains difficult to assess from aerial photographs alone.

4.3.1.1 Process domains

For geomorphological process domains, each domain is characterised by the dominant processes that reshape the landscape. The process domain classification applied in this study was developed based on the dominant processes observed at the study site, following the general concept of process geomorphology (Dikau et al., 2019).

The following process domains were identified:

The **glacial domain** contains the glacier itself and sediment directly influenced by glacial activity, including moraines and the glacial forefield.

The **periglacial domain** is characterised by freeze-thaw processes that shape the landscape, including rock glaciers, solifluction and frost weathering.

The **gravitational domain** is defined by exposed steep bedrock and steep terrain where mass wasting occurs through rockfall, sliding and toppling.

The **fluvial domain** is where surface runoff is responsible for the erosion and deposition of material, representing the main pathways of debris flows.

4.3.1.2 Geomorphic landforms of rockfalls

For smaller rockfall volumes, characteristic landforms are rockfall cones or talus sheets, which are commonly found below steep rock walls (Shroder, 2013) as seen in fig. 4.7.

Depending on the process, rockfall cones have different morphologies. This was first described by Rapp (1960) and was further developed by Church et al. (1979).

In rockfall-dominated areas, the slope is covered uniformly, forming more extensive deposits called talus sheets (fig. 4.7). For more rapid and larger events, such as rock avalanches or dirty snow avalanches, the rock deposition has a more cone-like morphology. When water plays a greater role, the rock deposits reach further from the slope base. The channels in the rock walls are also consistently carved deeper over time. With sufficient time, these

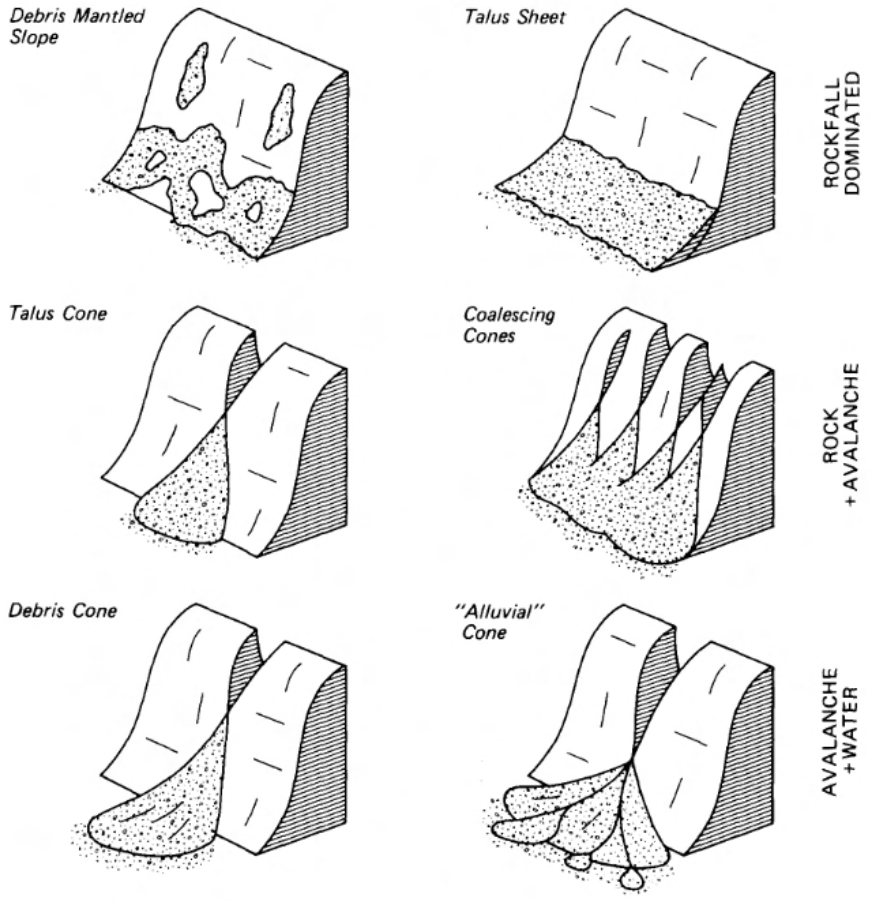

Figure 4.7: Morphological classification of debris slopes by Rapp (1960); Church et al. (1979). Depending on the water available, the morphology of the slope and the deposition of rocks change, as well as the presence or absence of avalanches.

can develop into debris flow fans, where water is drained through these channels after each rainfall event (Church et al., 1979; Dikau et al., 2019), as seen in fig. 4.7.

4.3.2 DEM of difference

A well-established method to analyse changes of the landscape is the DEM of difference (DoD) (Abermann et al., 2010; Hsieh et al., 2016; Kääb, 2002; Yang and Yu, 2025). This method was performed in ArcGIS with the raster calculator. One DEM was subtracted from a DEM of another year. This results in an elevation change between these two years. Elevation changes are always due to mass movement processes. The quality and accuracy of this method are strongly influenced by the alignment of the DEM's. Errors could lead to very high value differences, which are already described in section 4.2.3.

4.3.3 DEM transects

The transect method attempts to show the topography along a transect and how it evolves. The elevation was extracted using the Stack Profile tool in ArcGIS, which records the elevation every 0.5 metres and stores it in a table. This table was exported as a CSV file for further analysis and visualisation in Python. The position of the transect is shown in fig. 4.8.

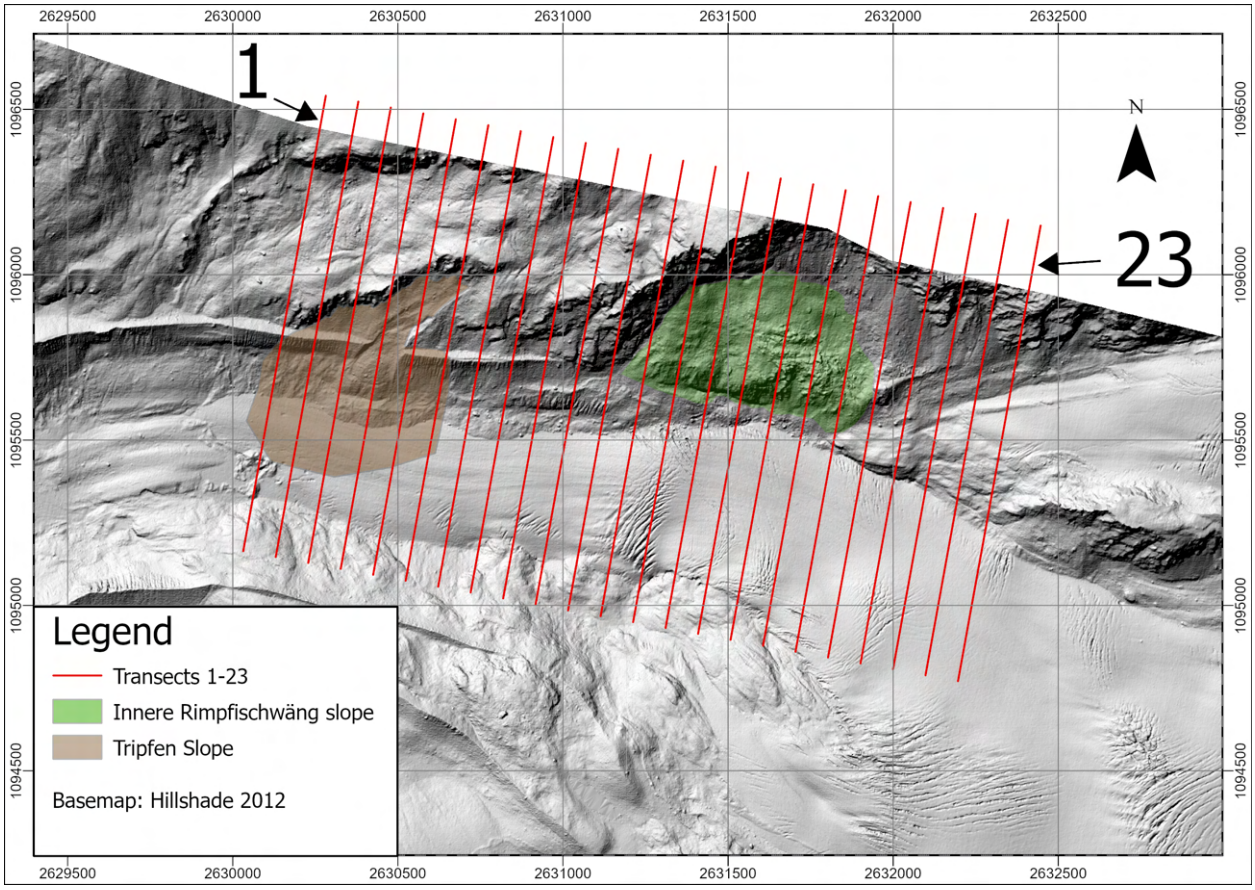

Figure 4.8: Transects 1–23 along the glacier and slopes of interest, spanning a total length of approximately 1400 meters.

4.3.4 Point tracking

Point tracking is a manual method to observe the displacement of distinct points in space and time (fig. 4.9). With this method, the displacement and velocity of these points can be calculated. The displacement was extracted by subtracting the coordinates between two different time intervals.

$$d = \sqrt{(\Delta x)^2 + (\Delta y)^2} \tag{4.4}$$

where Δx and Δy are the coordinate differences in the x- and y-directions between two acquisitions. The velocity was calculated by dividing the displacement by the desired time

interval. For the annual velocity, the time interval was simplified to one year, even though the acquisitions were not always taken on the exact same calendar day. This method was used to estimate velocity rates and to show how certain features evolved. It can help to understand the processes at the study site. For point selection, only large boulders or blocks were used, as they must be large enough to be recognisable throughout the entire time series. Additionally, they must be clearly distinguishable from the background to reduce picking errors.

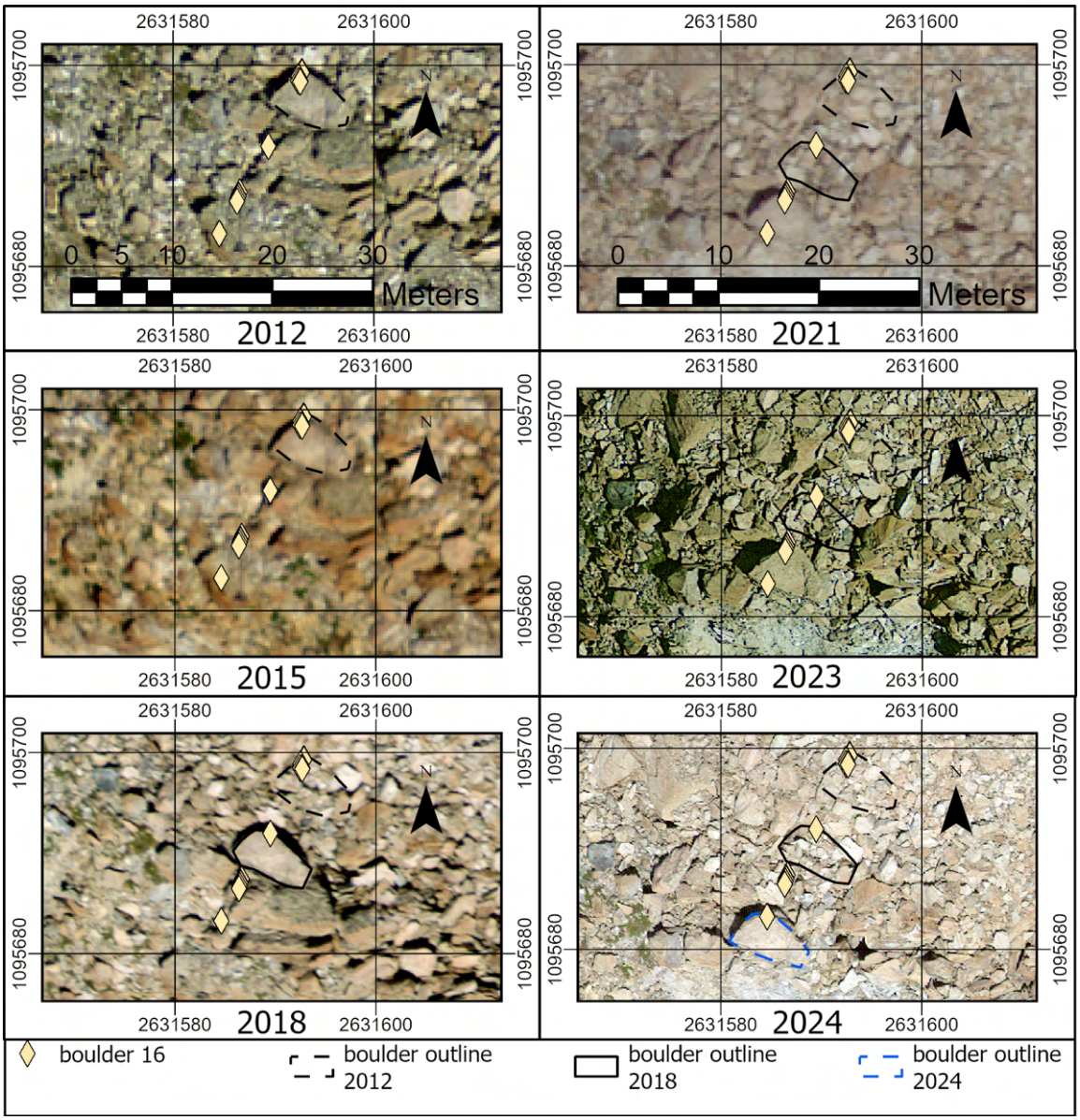

Figure 4.9: Example of a tracked boulder over the study period. Each year, the locations of the boulders were extracted by marking the same point on the boulder.

All selected boulders can be seen in fig. 7.1 and fig. 7.2 in the appendix.

Results

5.1 Geomorphological overview

This section presents the geomorphological process domains of the Findel Glacier and its margins, including the proglacial forefield and surrounding slopes (fig. 5.1).

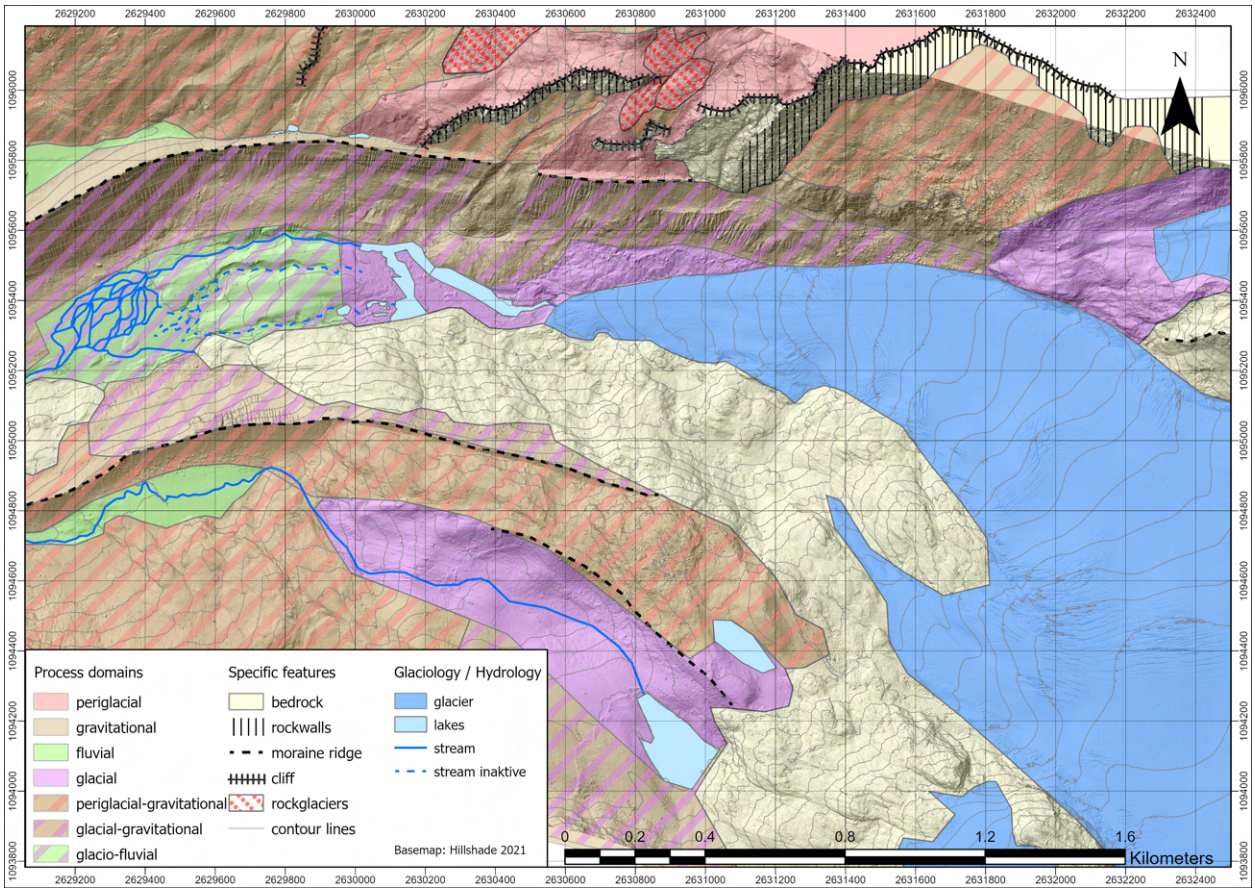

Figure 5.1: Geomorphological process domain map of the Findel Glacier forefield and adjacent slopes. Process domains, specific geomorphological features, and the glaciological and hydrological networks are mapped across the study area.

The identified process domains are typical for high alpine environments. The strong freeze-thaw cycles, both seasonal and diurnal, place the study area within a periglacial environment. The high altitude allows glaciers to exist and shape the valley, making it also

characteristic of a glacial process domain. The steep topography is a necessary condition for gravitational processes. Meltwater and precipitation also drive fluvial processes. At most locations, multiple process domains act simultaneously. A closer examination reveals specific geomorphological similarities between the two analysed slopes. Both slopes face south-west and are confined by steep rock walls. Below these rock walls, rockfall cones or talus slopes were found. Rockfall cones and talus slopes are categorised as landforms located at the foot of steep slopes where rock material accumulates over time. Nevertheless, there are many features which are unique to the respective slope.

The IR (fig. 5.2) slope runs directly up to the glacier and has no lateral moraines separating it from the glacier. As the glacier has lost a tremendous amount of thickness over the last 200 years, moraine material has accumulated between the glacier and the slope toe. A block field consisting of large boulders of the same lithology is located on the right side of the slope foot (when facing the slope). The main slope head is where the rockfall cones, or talus sheet in this case, are located. The slope crown extends above the slope head up to the rock wall (slope topology is illustrated in fig. 7.3).

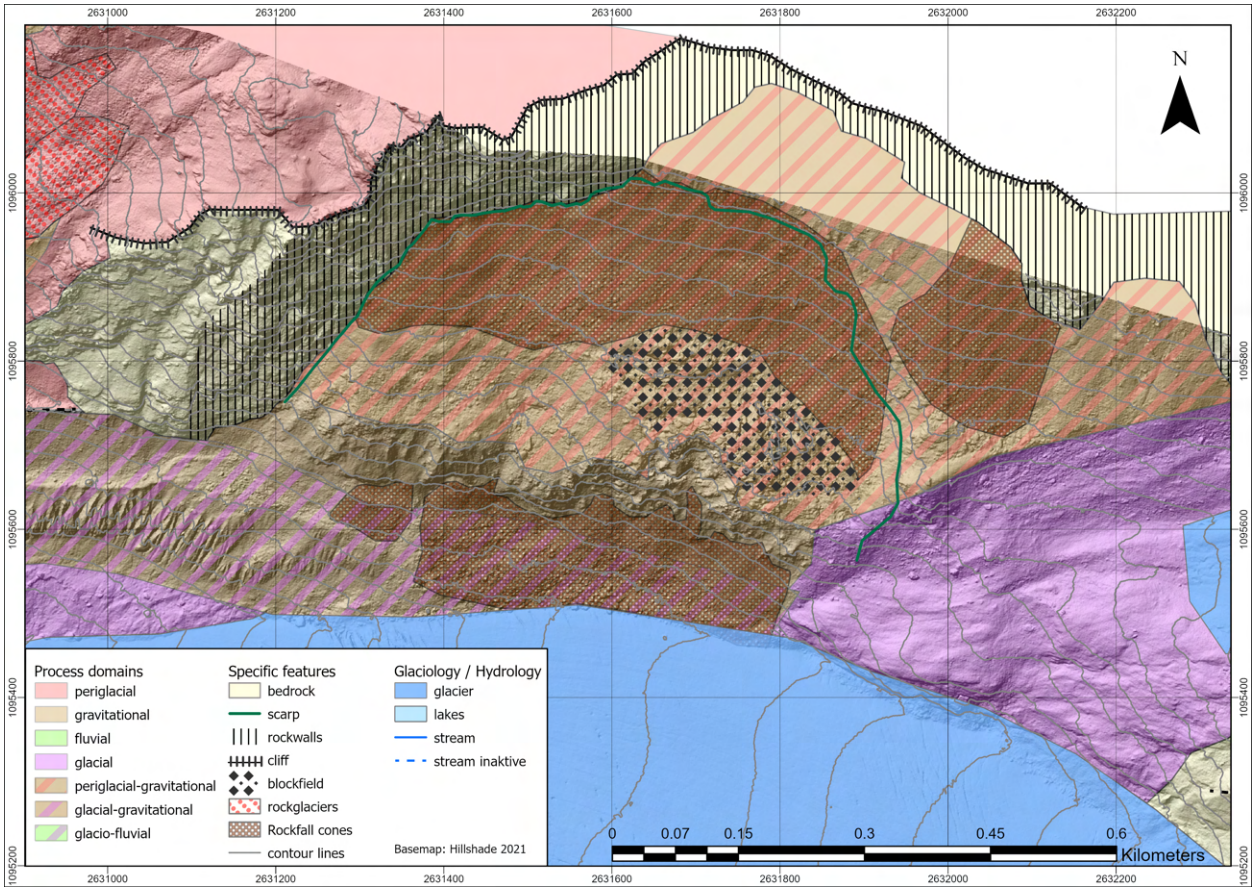

Figure 5.2: Geomorphological process domain at IR slope. Specific features of the slope are rockfall cones and a block field.

At the Tripfen slope (fig. 5.3), the most prominent geomorphological feature is the rockslide, which breached the lateral moraine. It consisted of darker rock material than the surrounding moraine walls, which now form the rockslide toe. The release area of the rockslide lay in a depression of the Tripfen slope, dividing the slope into a release area and a slope flank (slope topology is illustrated in fig. 7.4). On the Tripfen slope flank, numerous rockfall cones accumulate material from the steep rock walls above. There are patches where rockfall frequency is lower, allowing grass and other pioneer vegetation to establish. Further above, small rock glaciers are present on the slope.

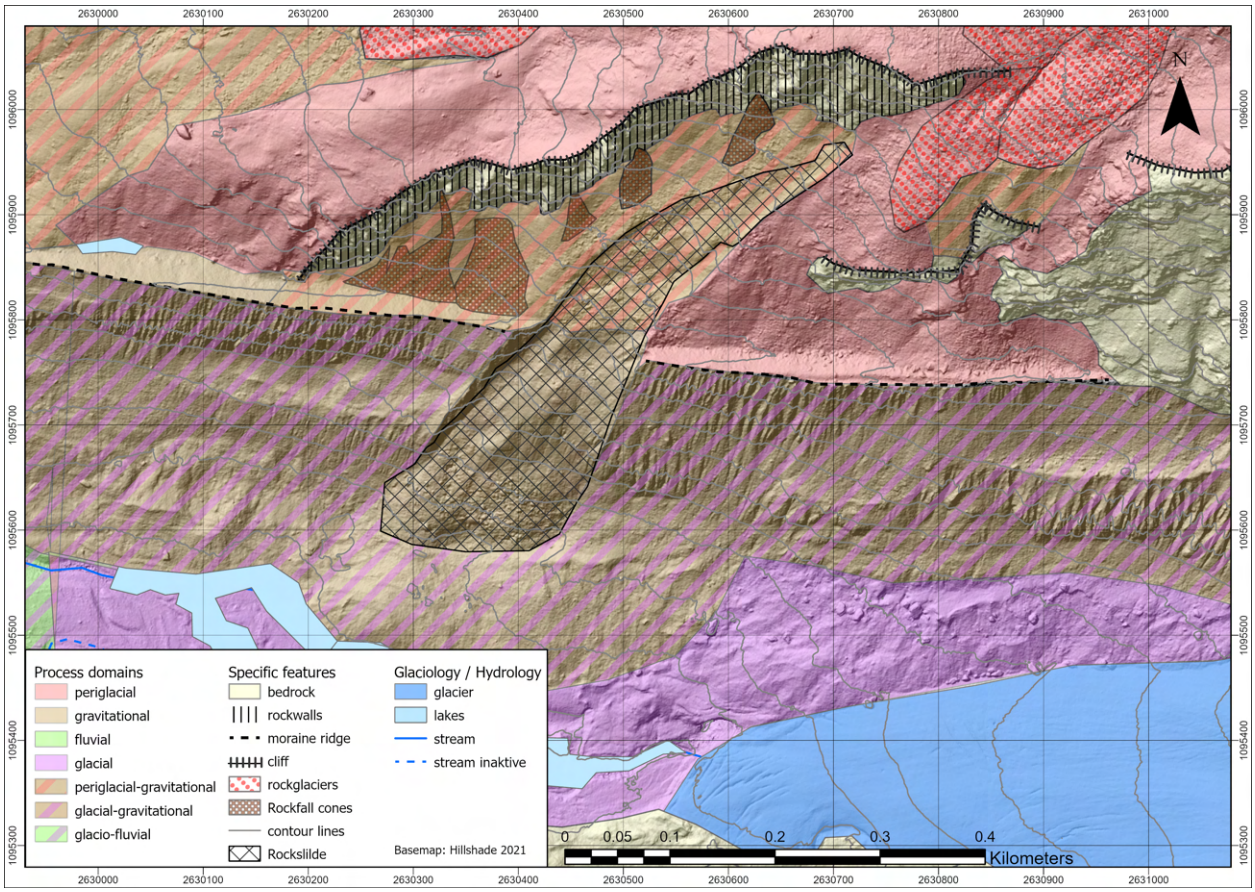

Figure 5.3: Geomorphological process domain at Tripfen slope. Specific features of the slope are the rockfall cones and the rockslide.

5.2 Findel Glacier

Here we present additional evidence of glacier retreat (fig. 5.4), consistent with findings previously reported by GLAMOS (2026) (fig. 3.2, fig. 3.3) The glacier shows a strong retreating trend over the 12-year study period, particularly at the glacier tongue. Since both slopes are located near the tongue, this has exposed many new surfaces, allowing various geomorphological processes to act upon them.

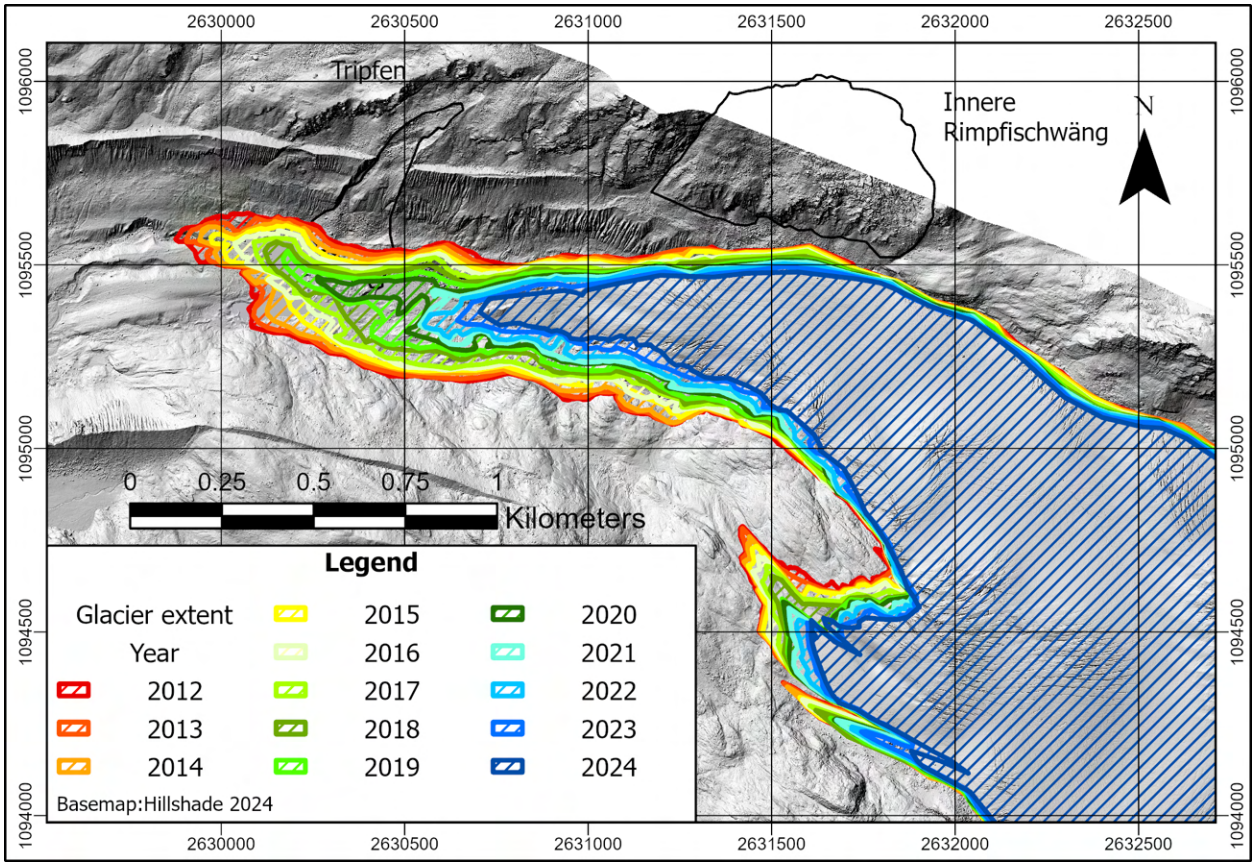

Figure 5.4: Glacier tongue evolution over the study period at the Findel Glacier.

In addition to a strong length reduction, the glaciers also lost a substantial amount of ice thickness during this time.

In fig. 5.5b, Transects 2–5 show that the glacier has completely disappeared below the Tripfen slope. An ice thickness loss of approximately 40 to 60 metres was observed here.

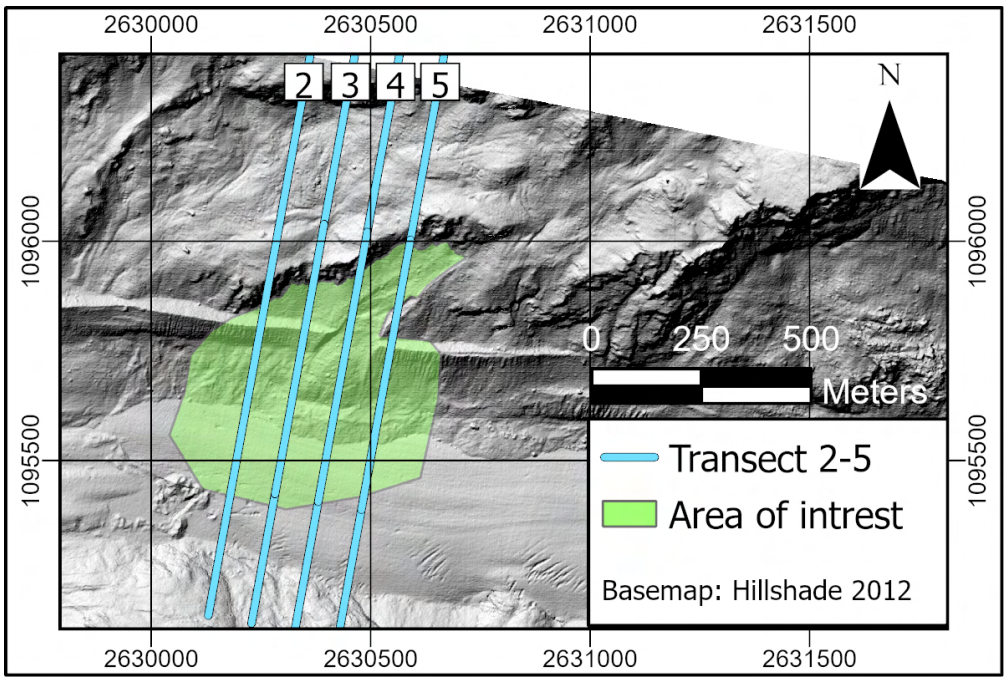

(a) Location of transects 2–5 for glacier tongue and Tripfen slope.

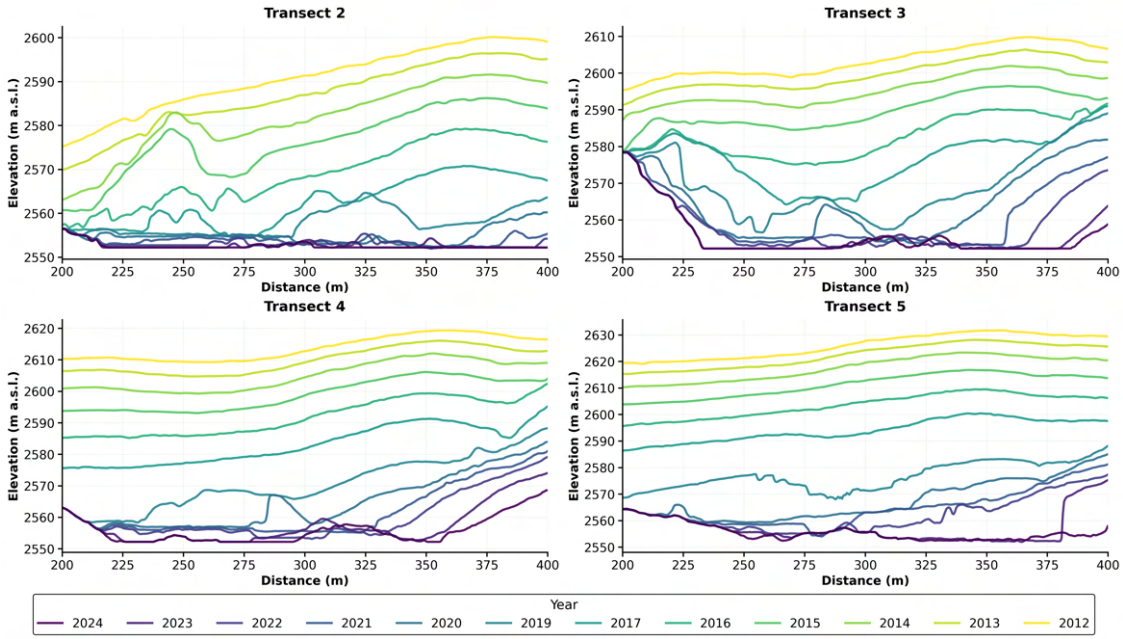

(b) Glacier tongue evolution 2012–2024 at Tripfen slope. The transects show the elevation at each year, ranging from 200–400 meters.

Figure 5.5: Transect shows glacier tongue thickness evolution over the study period at Tripfen slope.

Further up the glacier, closer to the equilibrium line of the glacier, the thickness changes are less pronounced and range from 50.2 m to 22 m (see in Appendix fig. 7.7).

At the Innere Rimpfischwäng, the thickness changes were also substantial. Transects 13,15 and 17 (fig. 5.6) show similar thickness changes (fig. 5.6b).

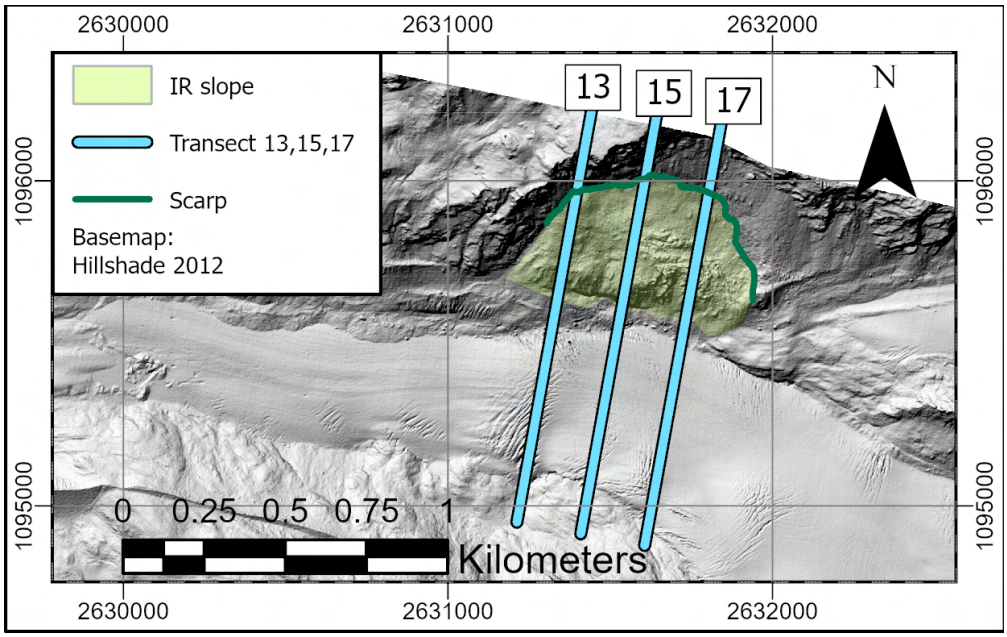

(a) Location of transects 13,15,17 for glacier thickness and IR Slope

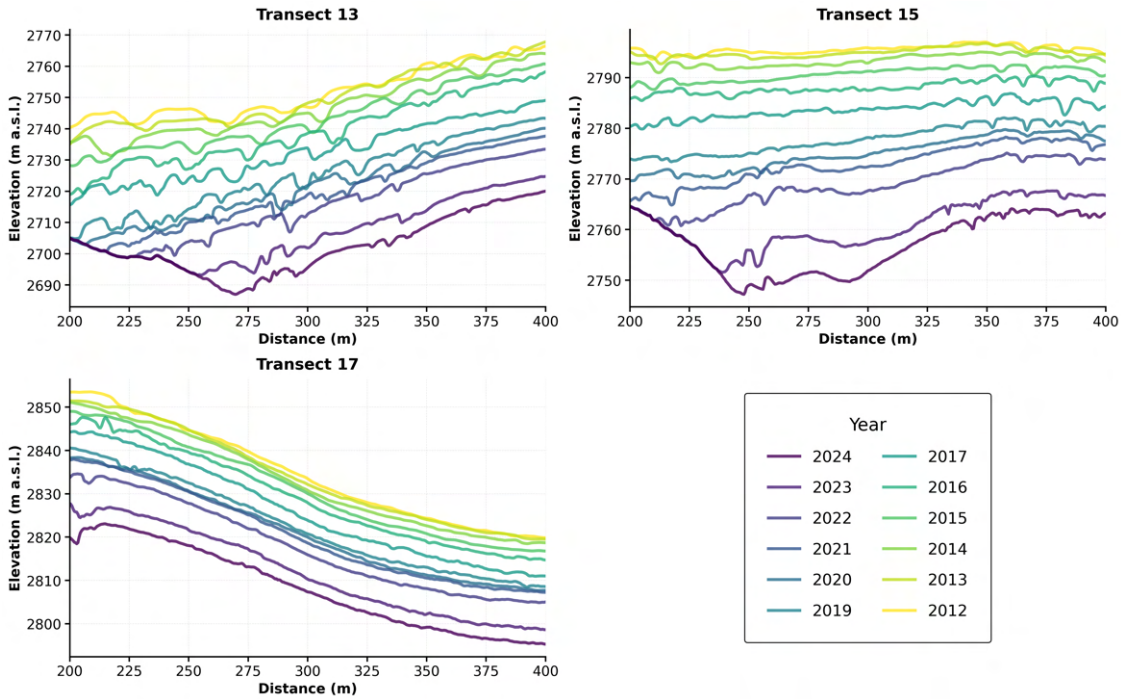

(b) Glacier thickness evolution 2012–2024 at the IR slope. The transects show the elevation at each year, ranging from 200–400 meters.

Figure 5.6: Transect show glacier thickness evolution over the study period at IR slope.

5.3 Innere Rimpfischwäng slope

5.3.1 Spatial analysis

The IR slope showed massive elevation changes during the analysed study period. In this section, all the changes will be shown in detail.

Through observation of the DOP imagery, a main scarp could be identified (fig. 5.7). Between 2017 and 2018, a band of lines covers almost all of the slope head. In later years, this line is less visible. Below these lines, strong elevation could be registered.

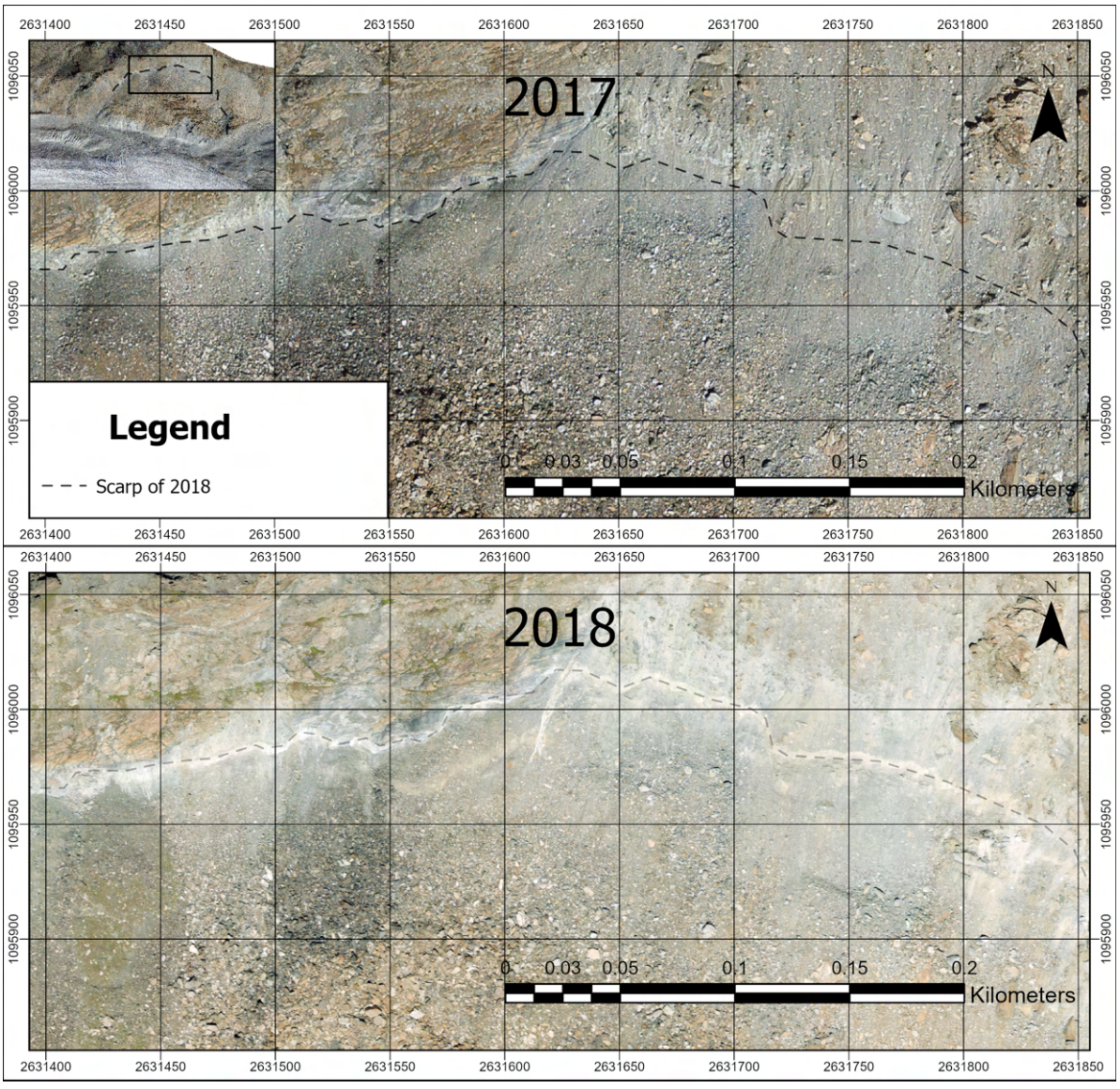

Figure 5.7: First identification of a main scarp at the IR slope.

Along this main scarp, the slope showed a depletion of material. This scarp confines the unstable material at the slope head. The lower boundary follows the slope toe from 2012, defining the extent of the unstable area. In later years, the main scarp vanished because it was filled by new rockfall deposits (seen in appendix fig. 7.5).

This main scarp allowed the estimation of the unstable area of the slope, which was approximately 225,528 $m^2 \pm 487$ m^2. The surface lowering is associated with downslope material transport. This volume was estimated at $932'283.8 \pm 29'042$ m^3 for the period 2012–2021. The DSM strips do not cover the full extent for the following years. The slope toe continued to advance along the entire front towards the glacier. Additionally, movement was visible within the moraine material, which may indicate that the slope is pushing the moraine forward.

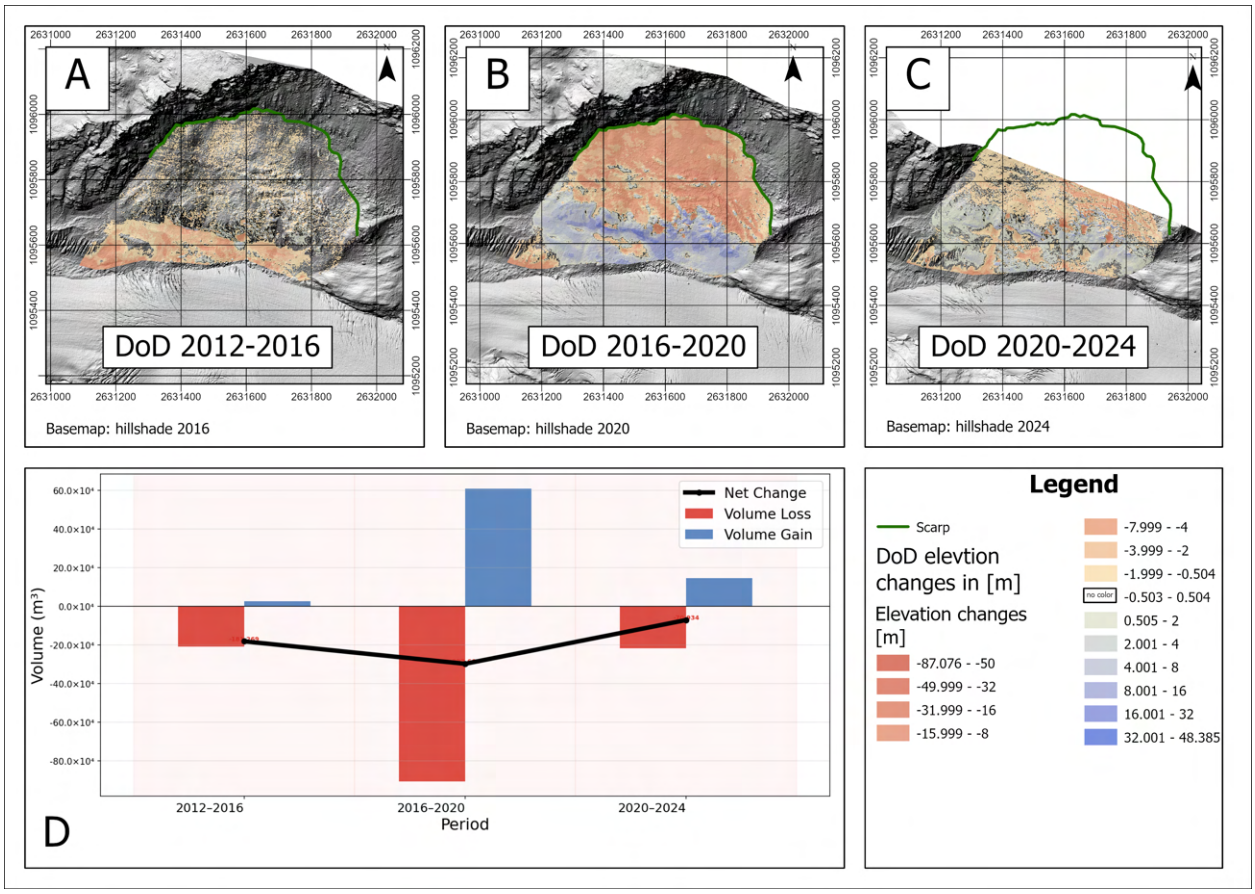

Figure 5.8: A: DoD 2012-2016, B: DoD 2016-2020, C: DoD 2020-2024, D: Volume changes in the slope and the moraine below the slope.

There is an imbalance between the volume which was lost (elevation decrease) and the volume which was gained (elevation increase) (fig. 5.8 D). In the moraine zone, glacier thinning (described earlier in section 5.2 ranging from 20 to 50m, strongly influenced the elevation). This was also evident in the period 2012–2016 (fig. 5.8 A), where the moraine showed

a distinct lower signal. This trend continued into later years but became less pronounced, as the accumulation of rockfall events increasingly obscured the lower signal (fig. 5.8 C).

In addition to elevation changes, boulder displacement helps to identify and verify surface changes and to estimate horizontal movement within the slope, as shown by the boulder tracking data (fig. 5.9). At the slope head and beyond the outer scarp, some boulders could not be tracked in later years (2022–2024), as the DOP image extent decreased over time, leaving these boulders outside the covered area.

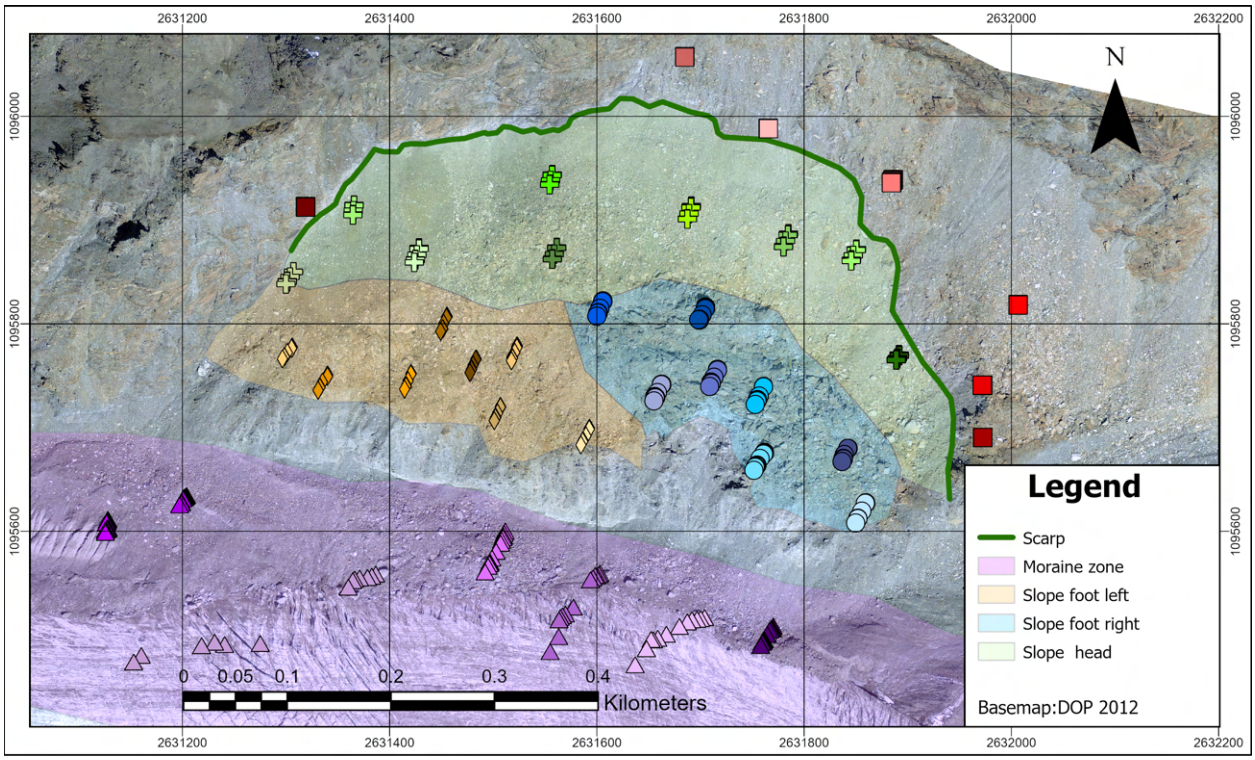

Figure 5.9: Location of each boulder at the IR slope. Outside scarp boulders did not show significant movement during the study period. Slope toe boulders could not be tracked due to frequent rockfall events.

5.3.2 Temporal analysis

Three major events affecting the entire slope body can be identified in fig. 5.10: the periods 2017–2018, 2018–2019 and 2023–2024. During these periods, activity within the slope was at its highest, with many boulders displaced by up to 9 metres between 2017–2018. In the years 2012–2017, slope movement was relatively low, as can also be seen in fig. 5.10 and fig. 7.6 (additional figures). Movements of only approximately 10 cm per year were recorded, which fall below the uncertainty levels of the DOP and DSM and are therefore not considered meaningful. It can be stated that the slope was more or less stable during this period.

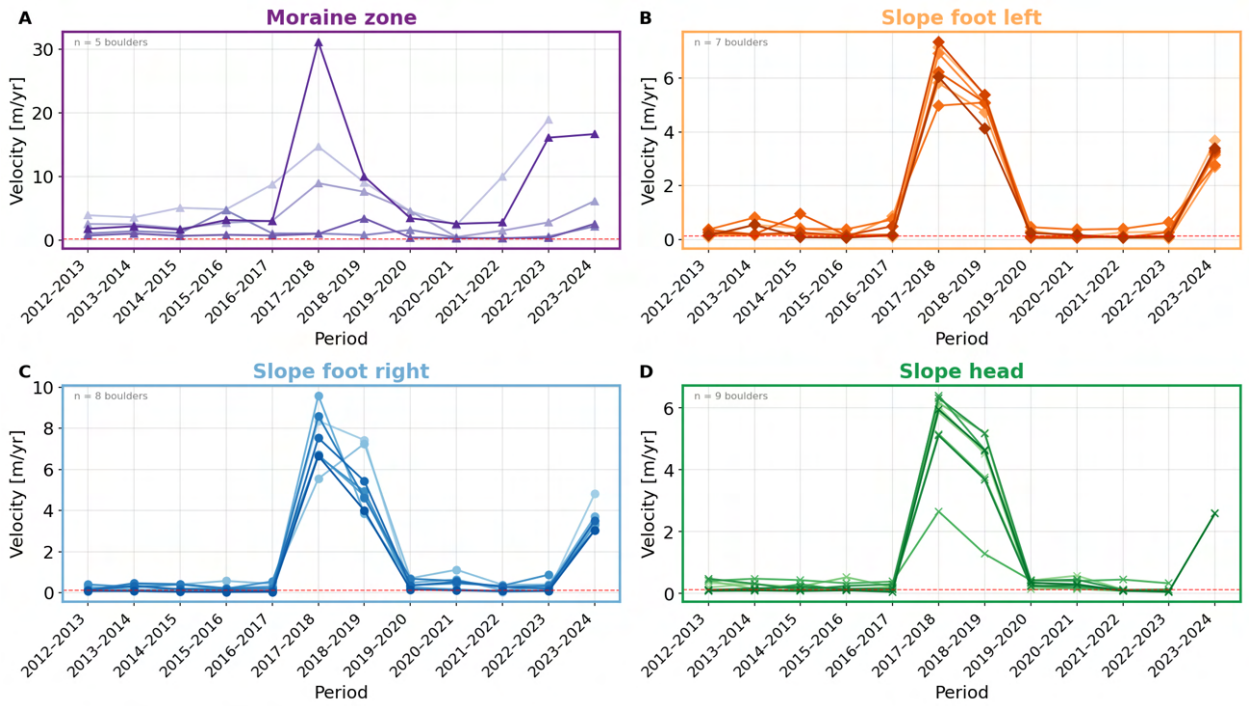

Figure 5.10: Velocity of the different topographic zones from 2012–2024.

This allowed to distinguish three phases of higher slope activity. When grouped, the right slope foot consistently showed the highest slope velocities, while the slope head showed the lowest velocities within the slope body. The boulders in the moraine zone did not follow this signal of higher slope activity (fig. 5.11).

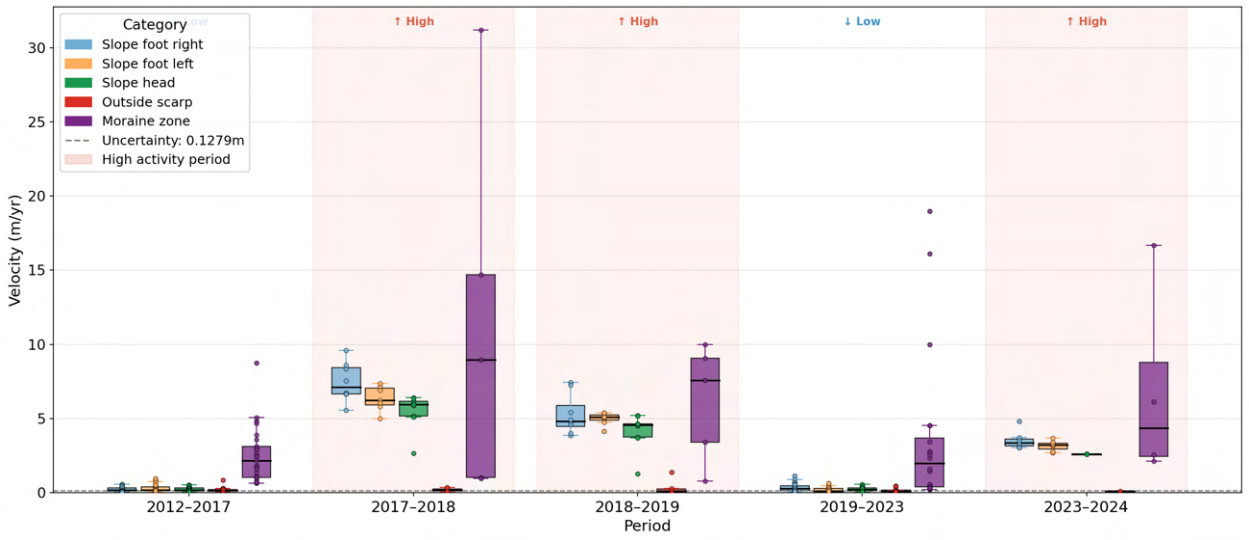

Figure 5.11: Velocities per category and grouped in low and high activity phases. Boulders outside the scrap and the slope body were used to validate movements of the slope body (compare fig. 5.9).

The movement trajectories within the slope shared a consistent direction, which indicated a single rupture surface (fig. 5.12). The steep slope angle continuously transported material further down slope. Boulders in the moraine zone that reached the glacier can be transported at a faster rate, as the glacier flow velocity was considerably greater than any of the observed slope movements.

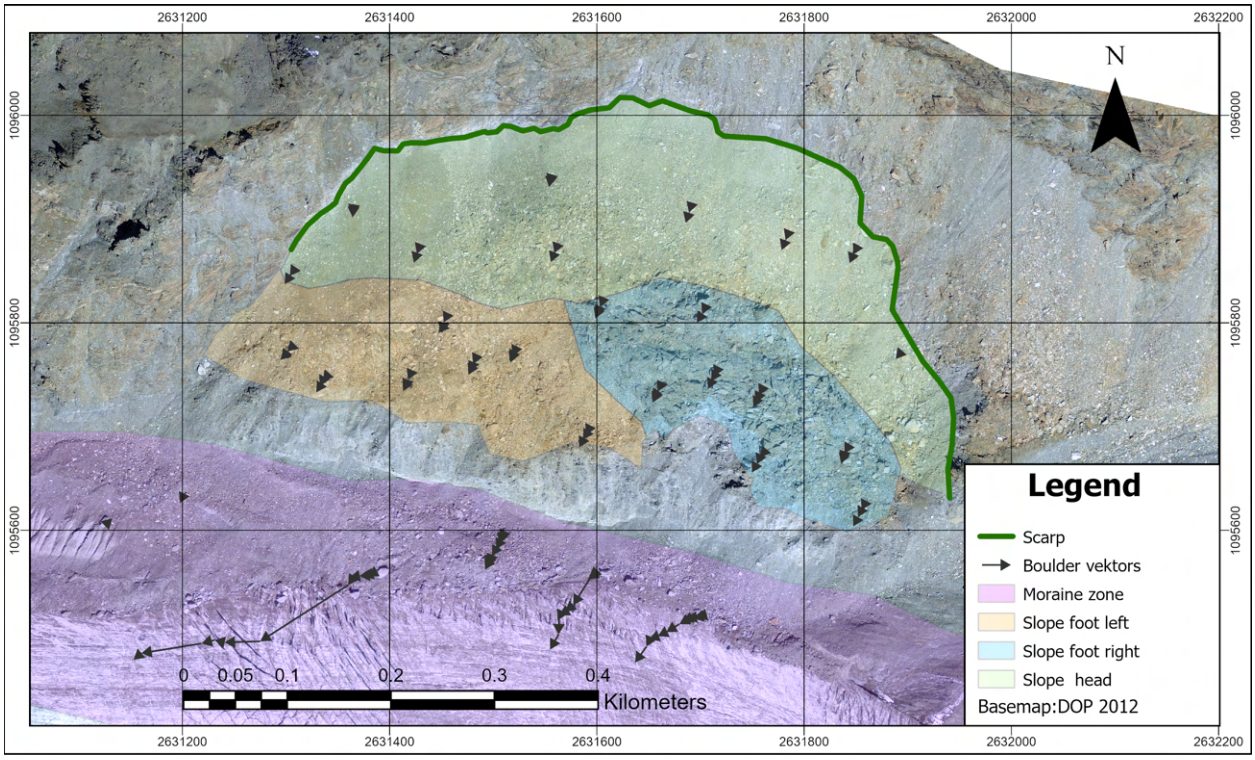

Figure 5.12: Velocity vector showing the direction of the movement per year.

In the period 2017–2019, lowering at the slope head and accumulation at the slope foot and toe were observed (fig. 5.13). Some larger boulders stand out from the dark blue zone at the slope head. The accumulation at the slope foot and toe could be attributed to the forward movement of the entire slope body towards the glacier rather than to a new relocation of material. Some partial rockfall events reached the moraine zone and the glacier, but the main change was caused by the uniform movement of the entire slope body.

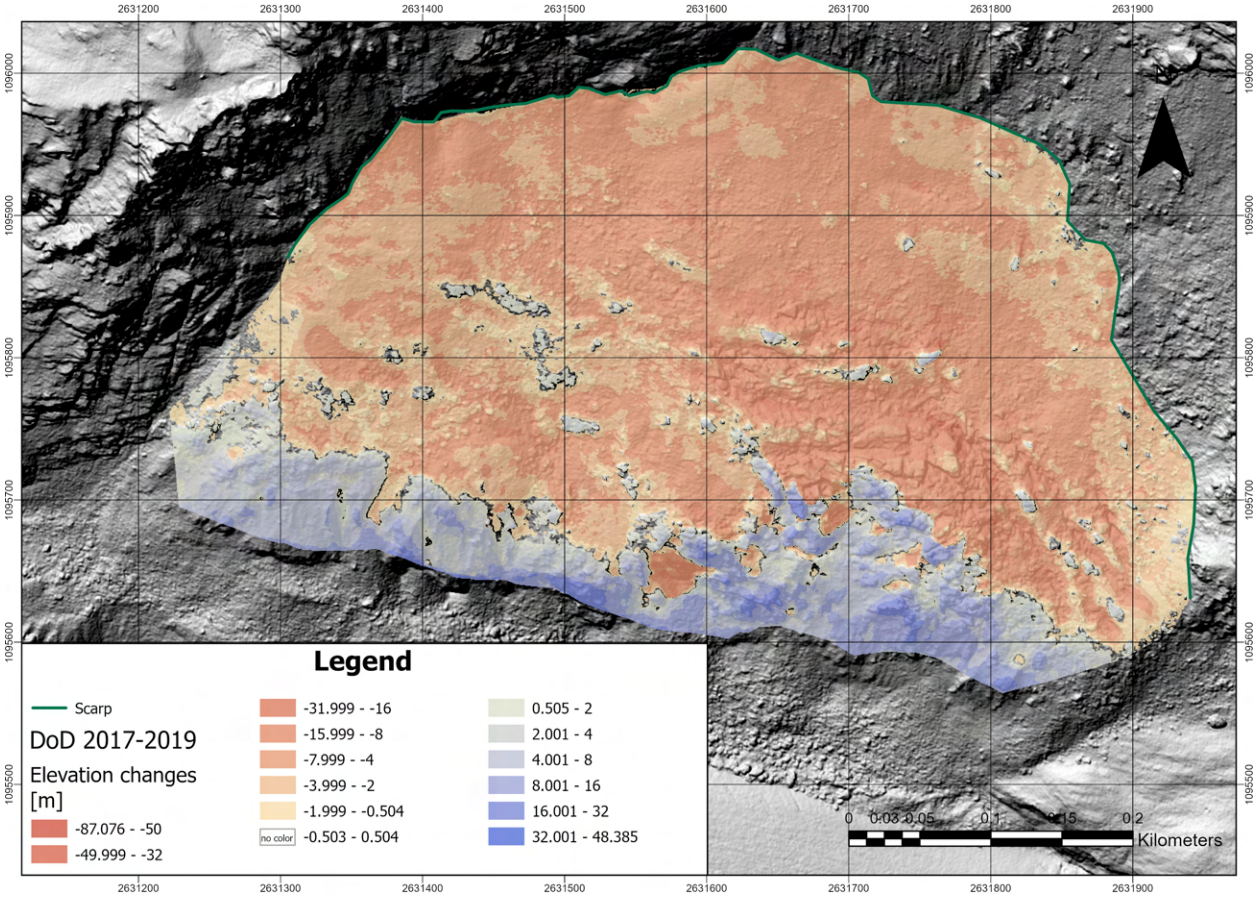

Figure 5.13: DoD (DEM of Difference) 2017–2019 of the Innere Rimpfischwäng (IR) slope. Reddish colours indicate surface lowering, bluish colours indicate surface elevation gain [m]. The green line delineates the main scarp of the slope.

In the following years, slope movement decreased rapidly, as also reflected in fig. 5.10 and fig. 7.6 (additional figures in the appendix). In the period 2019–2020, three distinct rockfall cones could be observed at the slope toe (fig. 5.14). The right side of the slope foot showed greater elevation changes than the left. This was where the block field was located. At the slope head were some small increases in material.

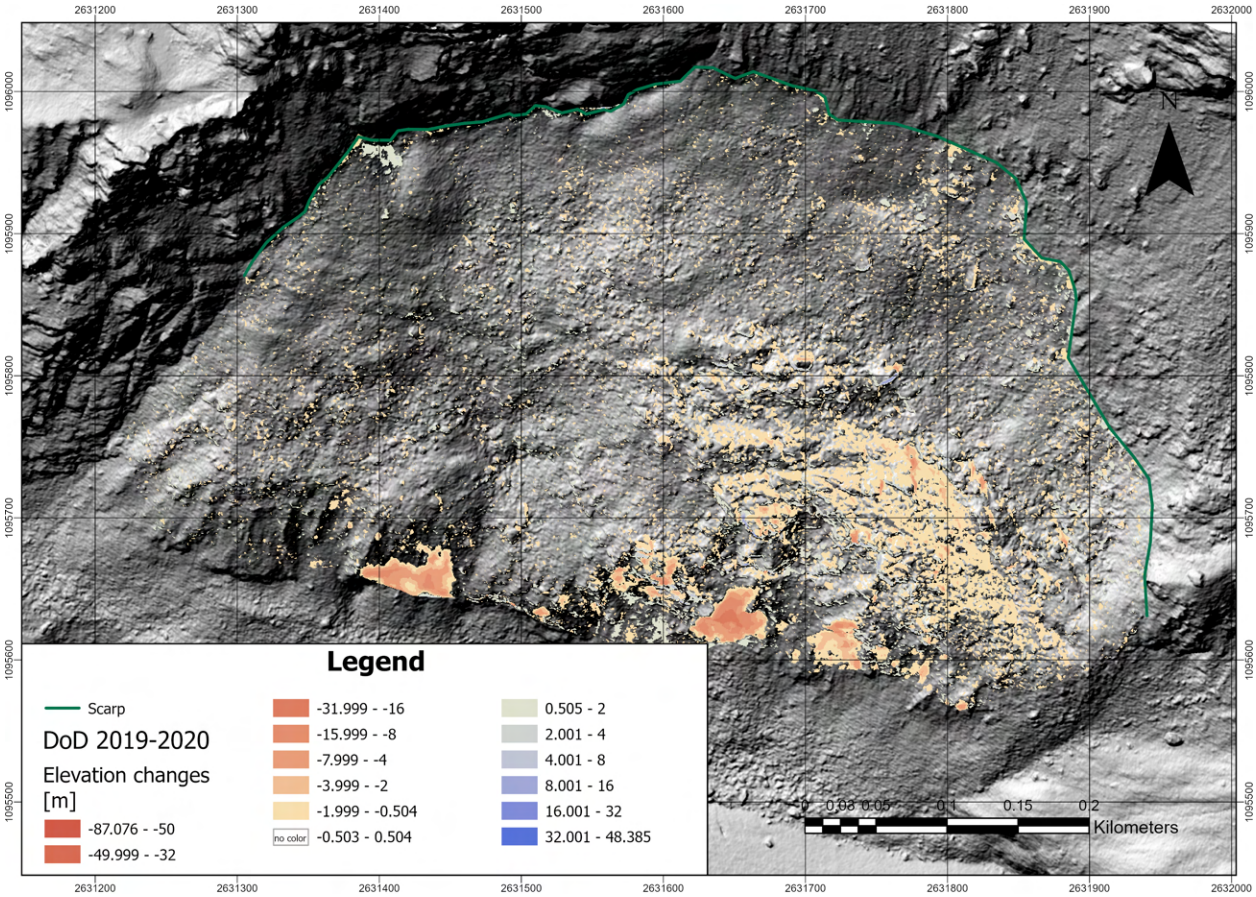

Figure 5.14: DoD (DEM of Difference) 2019–2020 of the Innere Rimpfischwäng (IR) slope. Reddish colours indicate surface lowering; bluish colours indicate surface elevation gain [m]. The green line delineates the main scarp of the slope.

In the period 2020–2021, small-scale rockfall events could be observed primarily at the slope toe, between the right and left slope foot (fig. 5.15). The right slope foot again showed minor elevation changes, but far less pronounced than in previous years. No elevation change could be observed at the left slope foot, further indicating that the right slope foot changes also occur independently of the left. This indicated less activity in the slope main body and just rockfall at the slope toe.

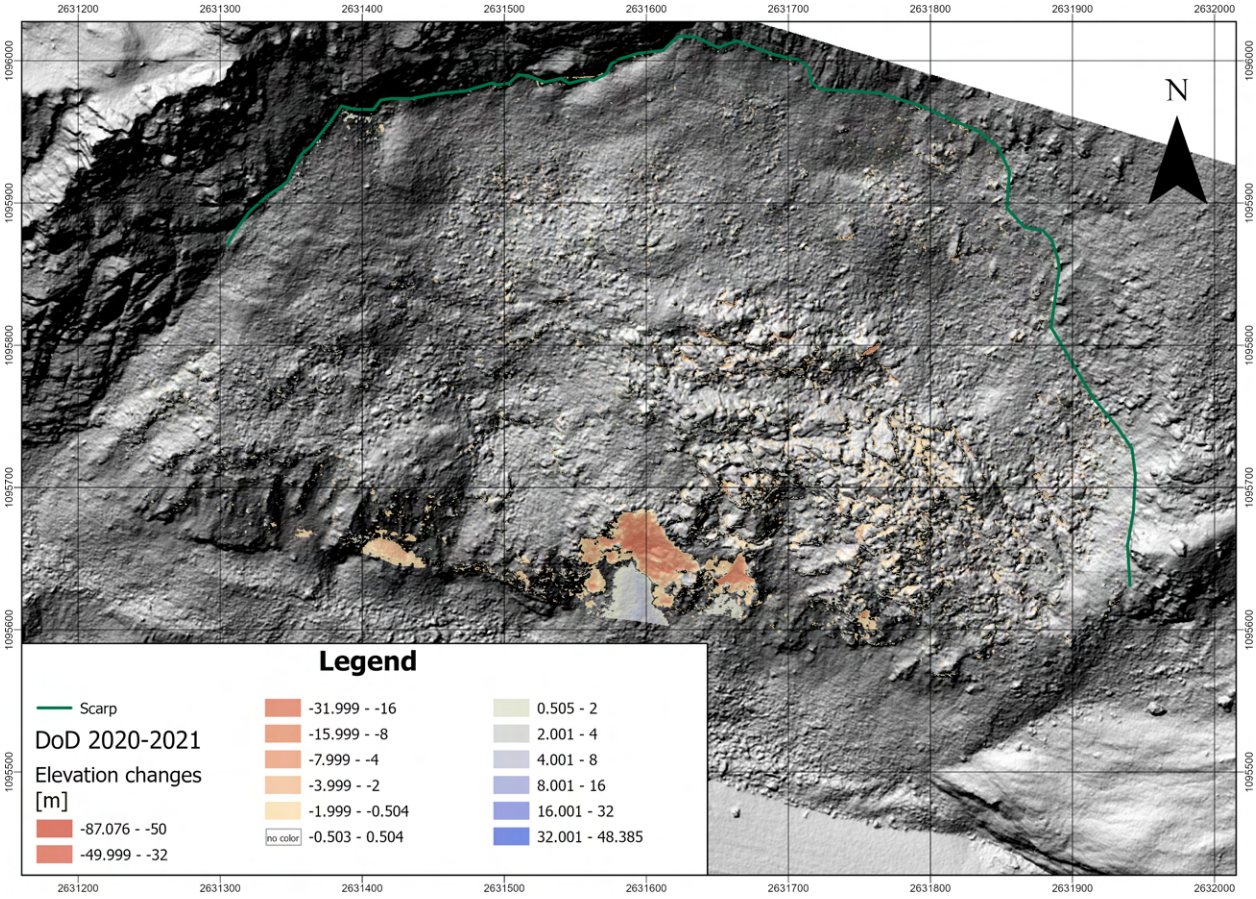

Figure 5.15: DoD (DEM of Difference) 2020–2021 of the Innere Rimpfischwäng (IR) slope. Reddish colours indicate surface lowering; bluish colours indicate surface elevation gain [m]. The green line delineates the main scarp of the slope.

In the period 2021–2023, the trend continues from fig. 5.14 and fig. 5.15, with almost no changes observed at the slope head and left slope foot. Rockfall activity at the toe was even less frequent, with only very minor changes visible at the right slope foot.

In the period 2023–2024, a similar pattern to that observed in 2017–2019 could be identified (fig. 5.16). All areas above the slope toe showed a negative elevation change, which corresponded to mass gain at the slope toe. However, the total volume change of this event was smaller than that of 2017–2019. Unfortunately, the image does not cover the whole slope. The slope toe had visible movement, a couple of meter at the beginning of the study period. Below the slope in the hillshade model, accumulation from the rockfall event can be seen.

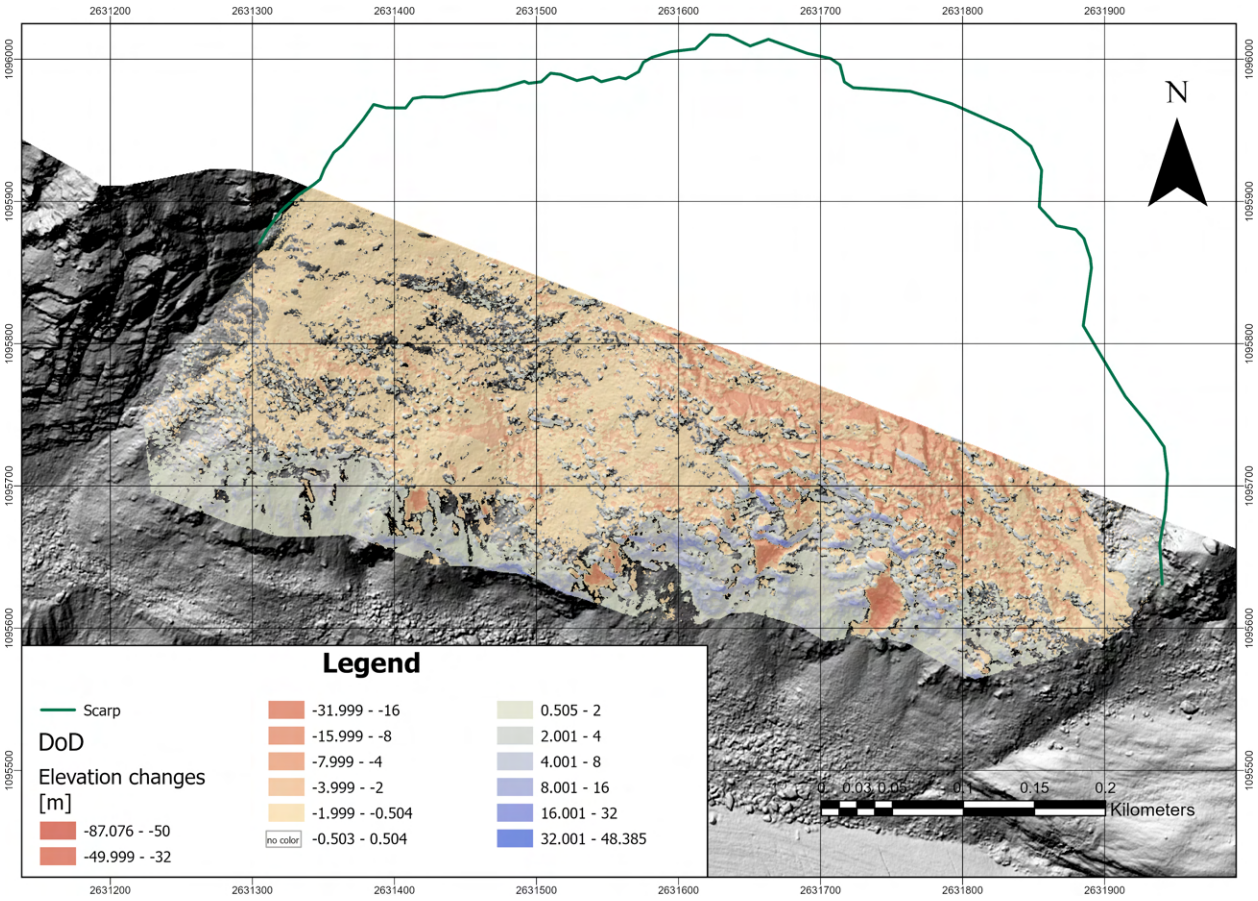

Figure 5.16: DoD (DEM of Difference) 2023–2024 of the Innere Rimpfischwäng (IR) slope. Reddish colours indicate surface lowering; bluish colours indicate surface elevation gain [m]. The green line delineates the main scarp of the slope.

5.4 Tripfen slope

The Tripfen slope is further downwards the valley. The slope is supported by steep moraines and nowadays a glacier lake is location at the proglacial zone of the Findel Glacier. A rock slide once breached the moraine and now reaches into the glacier lake.

5.4.1 Spatial analysis

At the Tripfen slope, the elevation changes were dominated by the melting of the glacier tongue. Another interesting feature is the active rockslide, which breached the moraine and is now located at the valley bottom (fig. 5.17).



Figure 5.17: Camera photo of the rockslide body in September 2025. Remnant glacier ice of the Findel Glacier is visible at right side of the rockslide body.

The volume of this rockslide was approximately 142,894 $\pm$ 4,223 m^3. This calculation assumed that the bedrock visible in (fig. 5.18 B/D) represents the slide horizon. The selection of the rockslide body area was based on the assumption that the brownish colouration represents the initial volume of the rockslide.

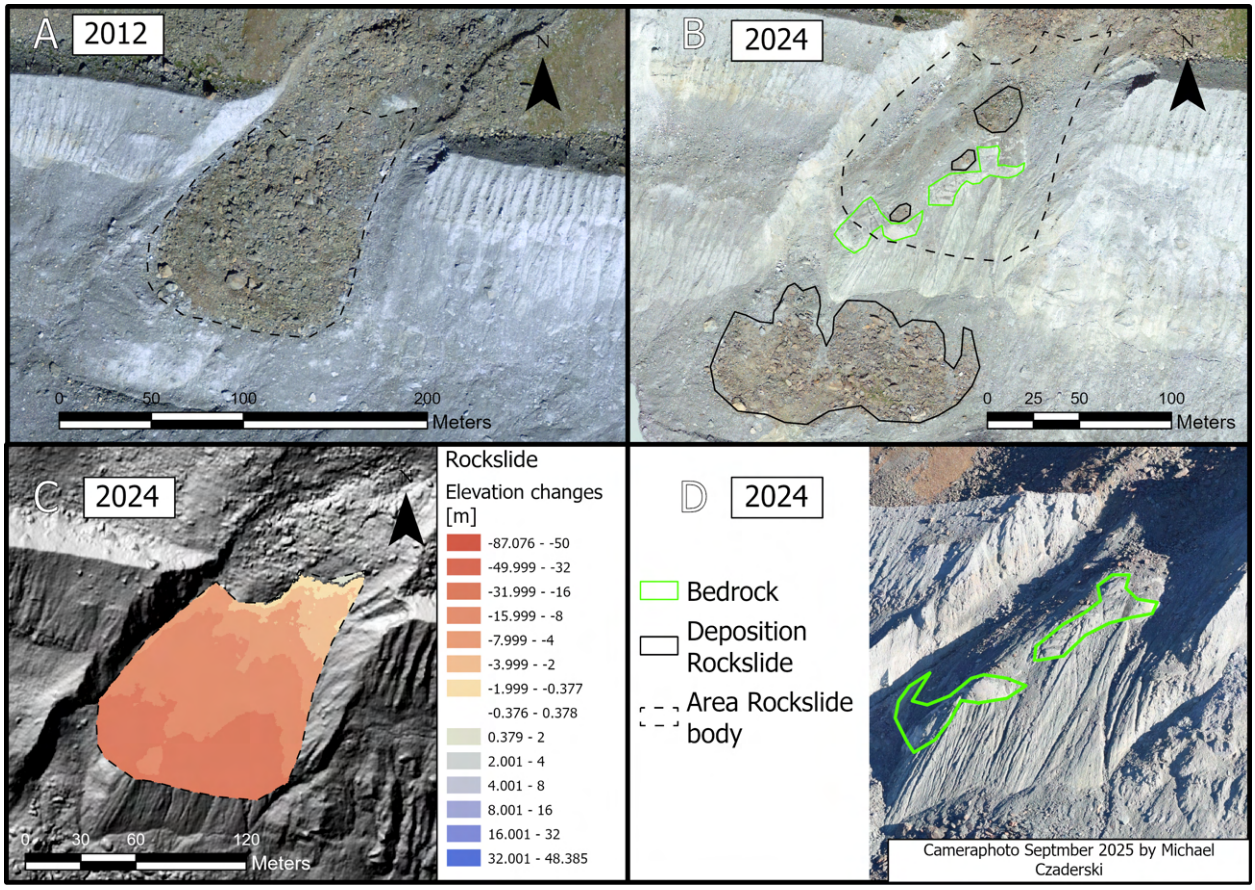

Figure 5.18: A: Rockslide Body in 2012, B: Rockslide body in 2024, C: DoD of the Rockslide Body. D: Aerial view of the Rockslide area and the exposed bedrock.

The rockslide's main body broke apart over the years. Nowadays, most of the material is located below the moraine, but other parts were deposited on the bedrock higher up the rockslide channel, as seen in fig. 5.18 B.

The rockslide originated from above the slope. In an early state around 2012, the rockslide reached the moraine. The moraine was not robust enough to withstand the rockslide, and therefore, the rockslide breached the moraine and pushed additional moraine material downward. A visible contrast in material was present in 2012, as fan-shaped material from the moraine walls could be identified. These three segments were all dragged down the slope. The moraine wall material covered the glacier and reduced melting. However, following the formation of the glacial lake, this material became eroded and entered the glacial-fluvial sediment flux. This can be seen across all transects and is visualised in fig. 5.19

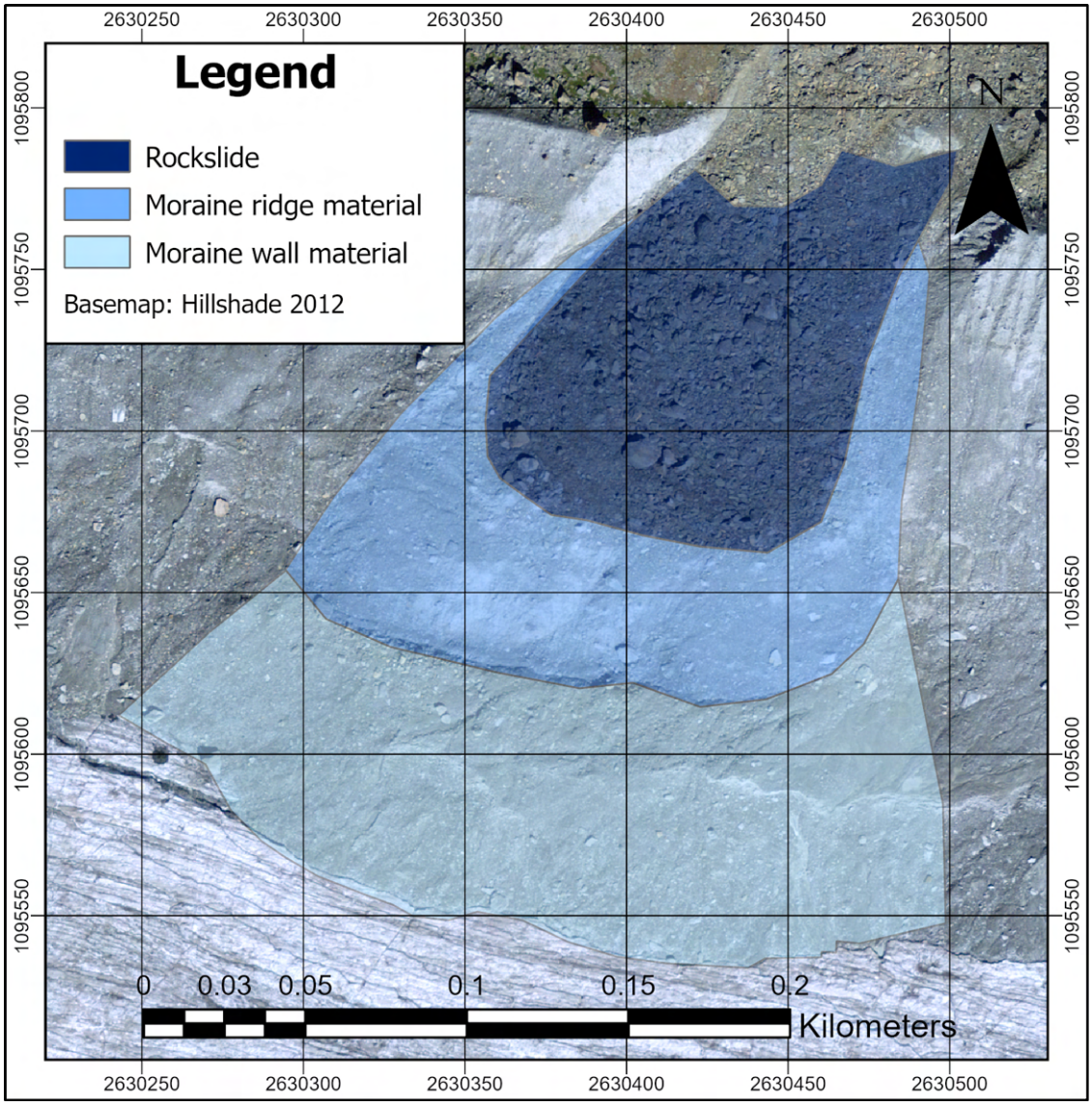

Figure 5.19: Different types of material of the rockslide body in the year 2012.

The grain size was vastly different from the rock slide body to the moraine material seen in fig. 5.19. The rockslide material consists of a mix of very large boulders and medium size boulder, whereas the moraine material looks more homogeneous. But even the moraine ridge and different types of grey show the origin of the material.

At the Tripfen slope, at the slope flank above the rockslide, a scarp which follows the whole rock wall could be found in the last year of the observation (fig. 5.20).

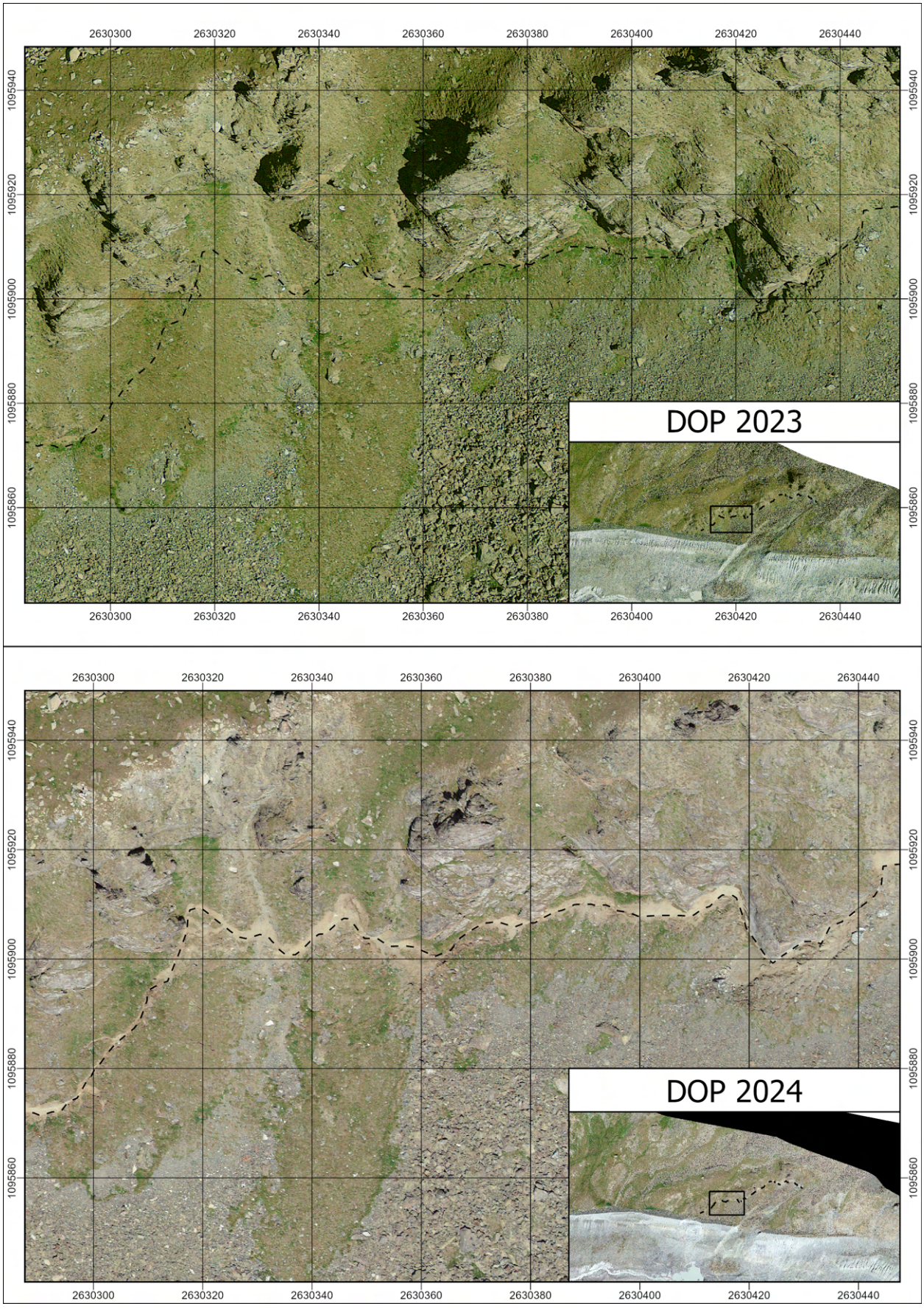

Figure 5.20: First identification of a scarp at the Tripfen slope in 2024.

The DSM reflects the strong elevation change at this site, which is also visible in the large elevation changes in the DoD 2023–2024 (fig. 5.21). Around the scarp, the elevation decreased, and an accumulation of material in the release area was observed. Additionally, the melt-out of dead ice within the rockslide area was also visible. On the bottom right side, a collapse of an ice dome or glacier gate also led to a large change in elevation. In blue, the partial collapse of the lateral moraine was observed.

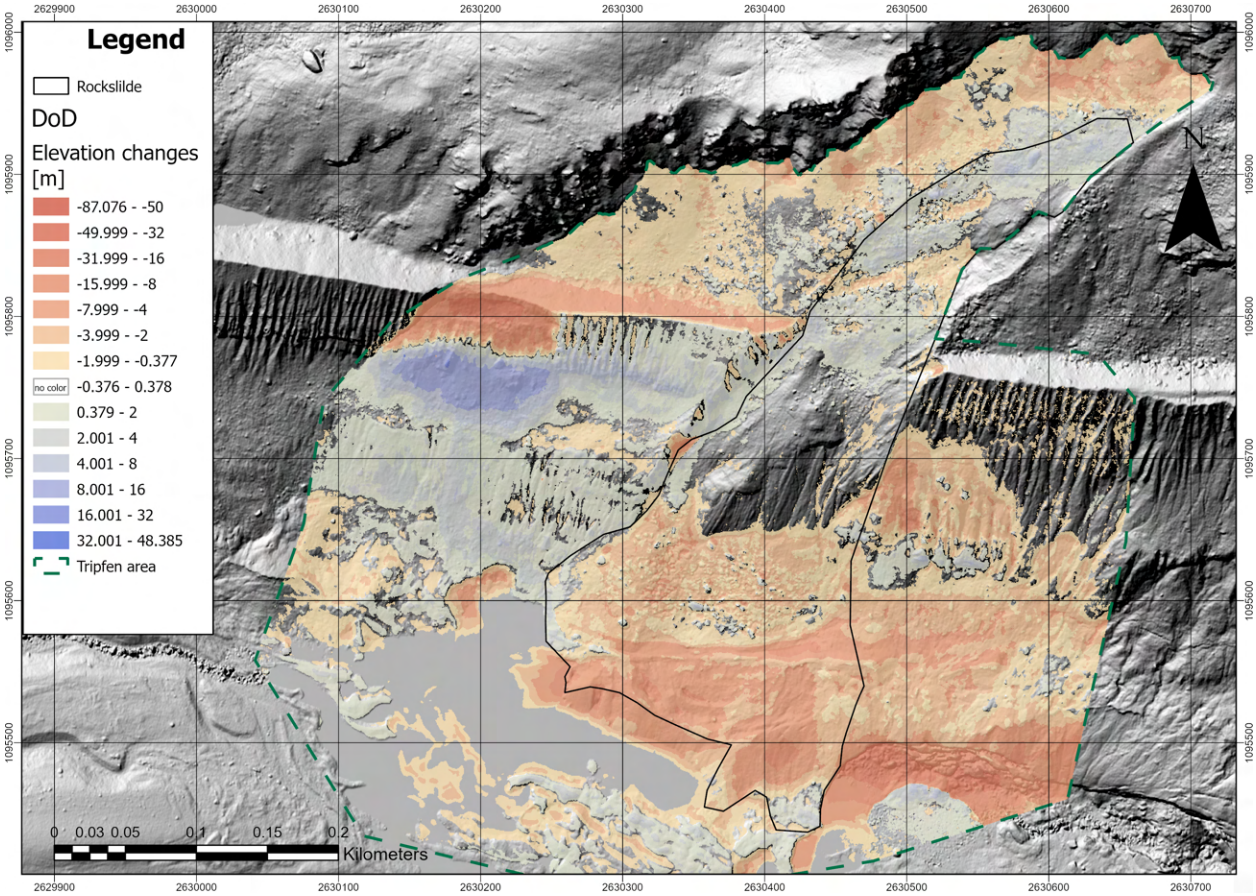

Figure 5.21: DoD (DEM of Difference) 2017–2019 of the Tripfen slope. Reddish colours indicate surface lowering; bluish colours indicate surface elevation gain [m]. Rockslide extent of the year 2024.

5.4.2 Temporal changes

The rockslide body glided on the glacier, where it expanded its front. With the glacier retreat, the main body moved to the valley bottom. In 2021, the rockslide reached its maximum extent (see fig. 5.22). Following this, the formation of the proglacial lake began to erode the rockslide mound, and after that year, the mound progressively decreased in size.

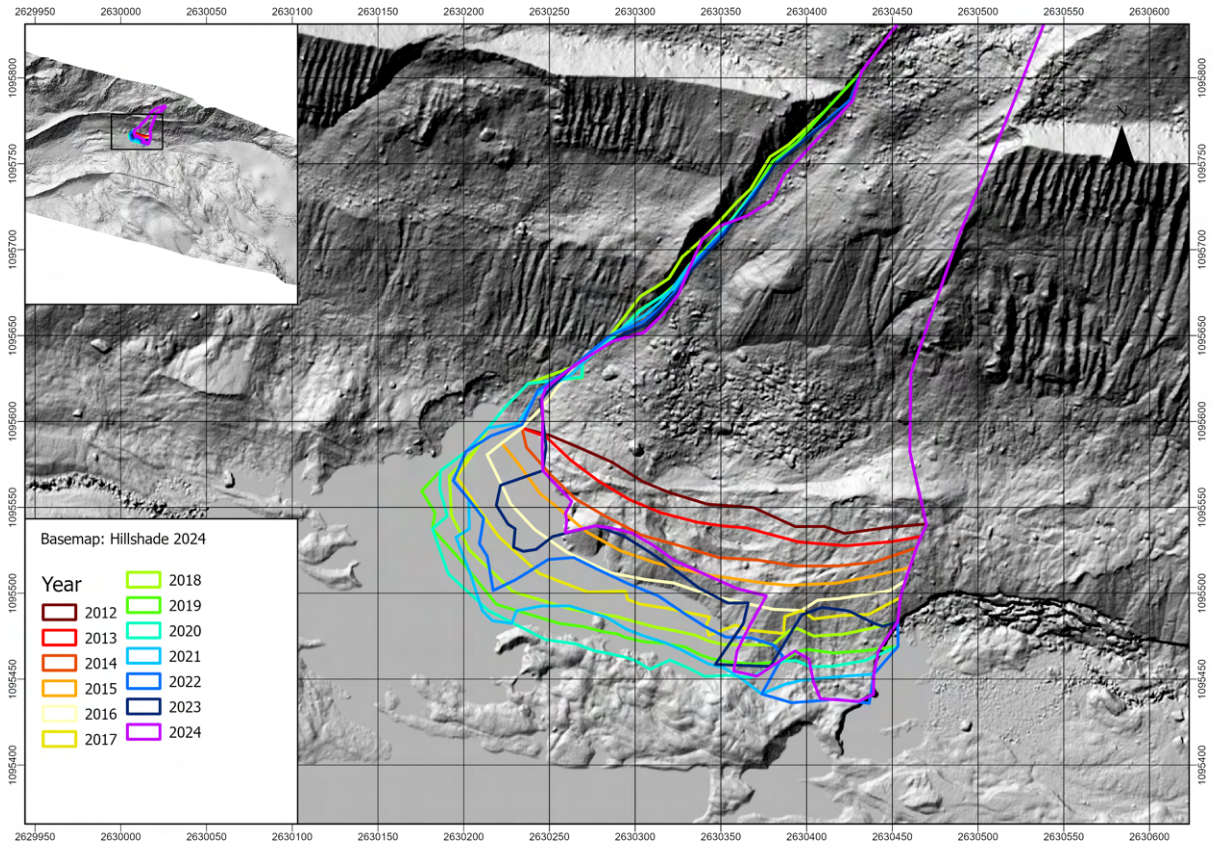

Figure 5.22: Rockslide body over the study period shown in different colors.

The rockslide acted as a strong thermal insulator and reduced the melting of ice beneath the rockslide. This explains why ice is still present below and around the rockslide, even though the glacier tongue has retreated by approximately 50 metres. The ice can be observed in the DOP imagery where the proglacial lake and the rockslide meet, as visible across all transects.

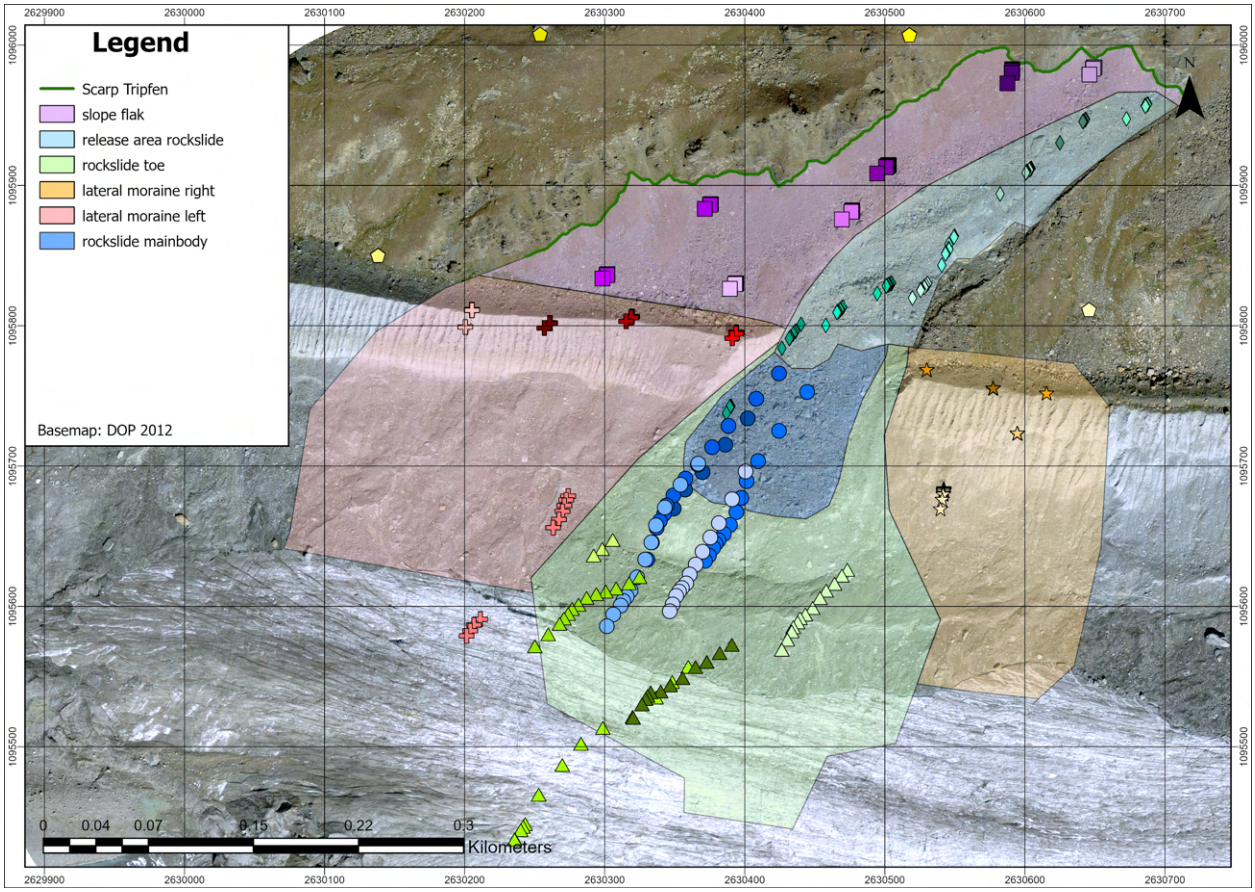

Figure 5.23: Selection of boulders at the Tripfen slope. The boulder represents the movement pattern of the five topographic features.

Figure 5.23 shows the selection of the boulders. The section of the categories was made by clear topographic features like the moraine and the rockslide body. Figure 5.24 shows that most acceleration happens at the same time, which is a good indicator that they are indeed one topographic unit.

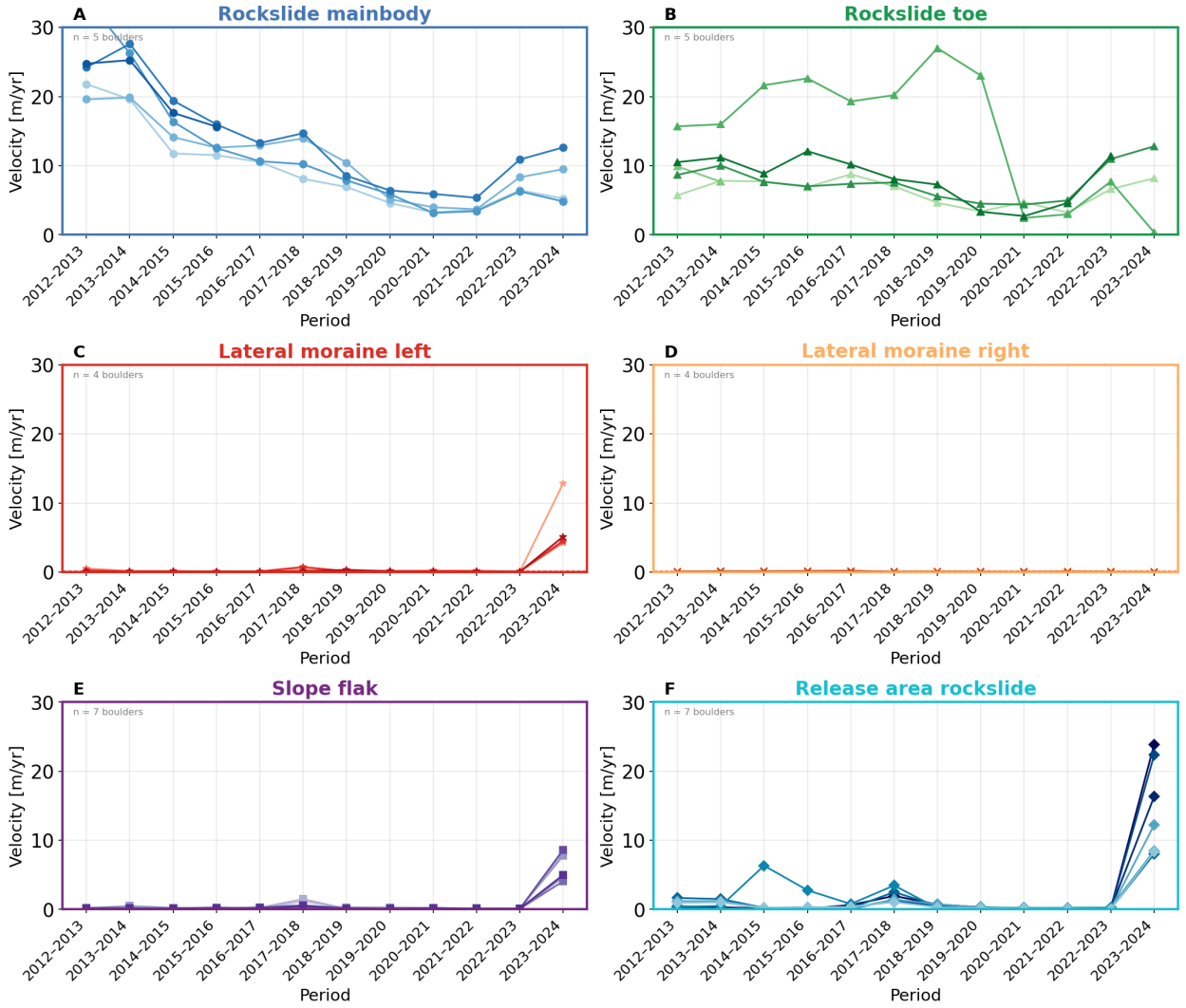

Figure 5.24: Velocity of picked boulder in the diffrent categories shown in fig. 5.23.

When isolating each category, the rockslide main body shows a decreasing movement trend as it reaches a lower gravitational potential (fig. 5.24). The rockslide toe also shows a similar decreasing displacement trend like the rockslide main body. The other zones remain rather stable throughout the majority of the study period. The left and right moraines remain fairly stable until the left moraine collapsed in the period 2023–2024. This may be connected to the acceleration of the slope above the left lateral moraine (fig. 5.24 D/E). The release area of the rockslide (fig. 5.26 B) shows lower velocities than the adjacent slope flank throughout the entire time series. However, in the period 2023–2024, the velocities of all boulders above the moraine become almost equal. At the slope flank, a scarp appears and transports a large amount of material downwards fig. 5.21.

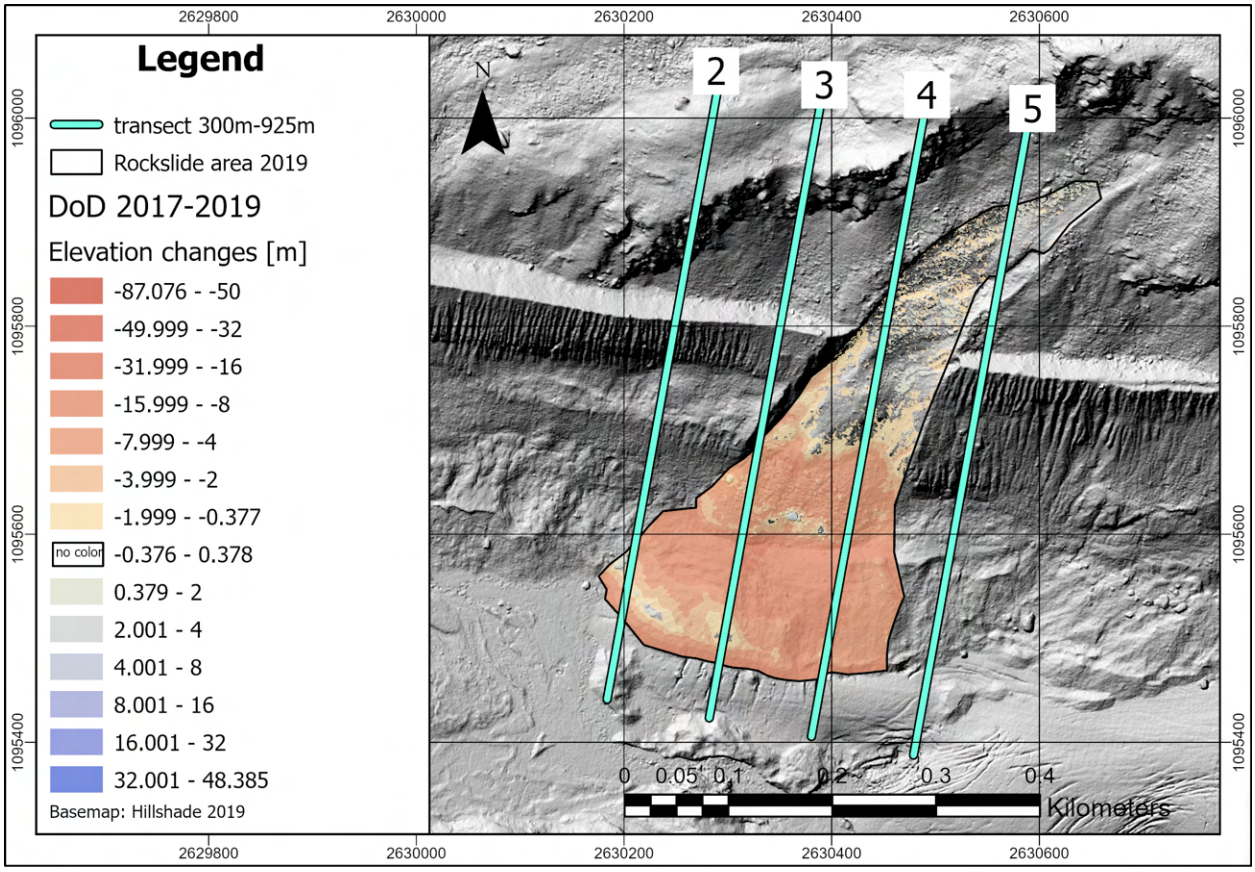

(a) DoD of the rockslide from 2017 to 2019 and the transect 2-5.

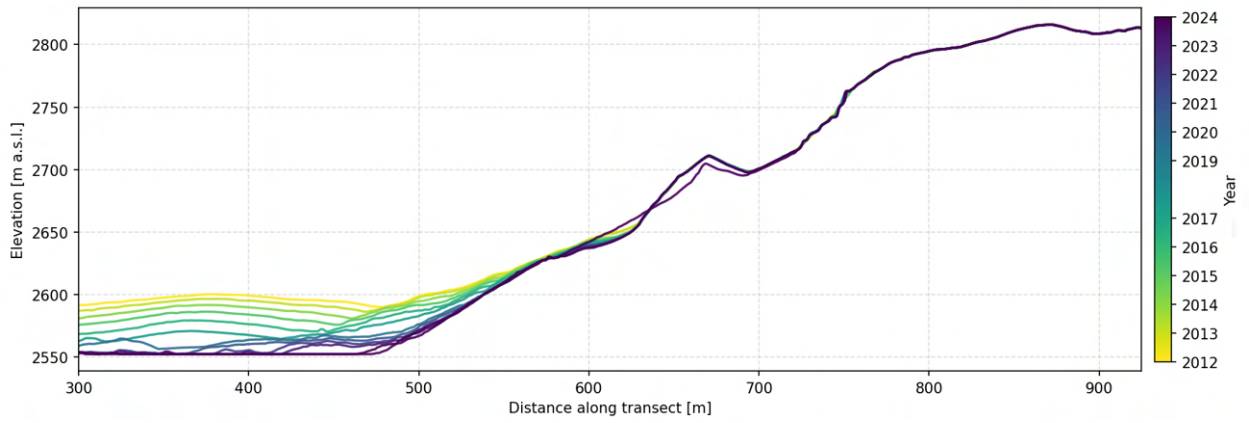

(b) Transect 2 showing the collapse of the moraine in 2023-2024. (Only 300-925 meters of the original transects are relevant for the Tripfen slope.)

Figure 5.25: Overview of all transects at the Tripfen slope and profile 2, where the moraine collapsed in the year 2024 is visible.

This partial collapse of the moraine and the accumulation of material from the walls of the moraine can also be observed in the DSM section 5.4.2. In earlier periods, the moraine showed fractures in the fine material below the moraine walls.

The highest movement velocities were observed at the mobile rockslide body (fig. 5.26). The release area of the rockslide was likely in a periglacial environment (compare fig. 5.3). Periglacial surfaces can develop solifluction or creep in soil through freeze-thaw cycles. This is consistent with the more constant movement pattern observed in this area compared to other areas outside the rockslide in the period 2012-2019. During the period 2019–2023, the movement was almost zero. Notably, boulders near the rupture line moved more slowly than those in the release area of the rockslide. The acceleration observed in 2023–2024 was therefore likely caused by the formation of the rupture line (compare to fig. 5.20).

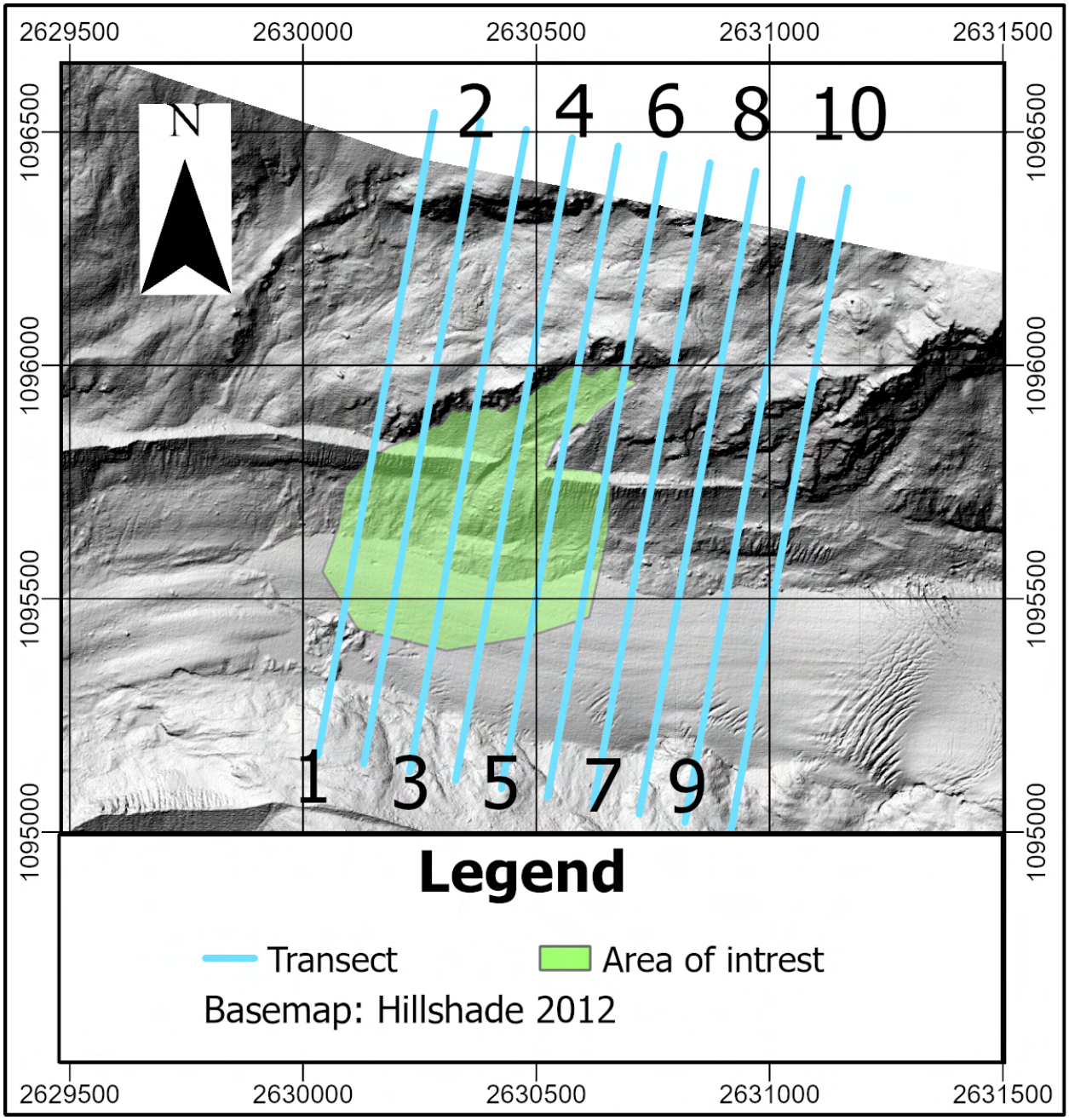

Figure 5.26: Trajectories and displacement vectors of the boulders at Tripfen slope. Color sheme show more dark red color for higher velocities.

Discussion

6.1 Quantifying changes in high alpine environments

The results showed that over the 12-year study period, significant changes at the glacier and in the glacier's forefield were observed. The floodplain showed multiple active streams, channel reworking and sediment transport. Glacial streams formed new sediment banks, and a proglacial lake with a varying extent could be observed. This process is part of the glacio-fluvial process domain (fig. 5.1) . The steep moraines of Findel Glaciers showed imprints of gully erosion. In the glacial domain, there is evidence of ice-melt within the moraine. Outside of the margins of the Findel Glacier, the most common process domains were periglacial and gravitational. Features of this process domain in the study area include rockfall cones and slopes with unconsolidated rocks. Within these rock deposits, rock glaciers can be found. These findings are in line with the previous geomorphological map of Alexander Ruff (2015). His study extends from 2005 to 2014. In the forefield on both sides, the moraines were found to be unstable. On the one side, he concluded that there was groundwater or lake water pushing through the moraine. A process that was ongoing until 2021. However, in general, in the lower part of the glacier and the forefield, no new mass movements appeared. The orographic left side of the Findel Glacier exhibited greater elevation changes than the right one, due to the presence of freshly exposed bedrock and generally less steep terrain. Within the glacier forefield, elevation changes were less pronounced compared to the adjacent slopes. The Findel Glacier shrank drastically during the 12-year study period, with ice thickness losses of up to 50 meters and a length reduction of approximately 1.5 km. The Findel Glacier had an average annual mass balance of -0.43 (m w.e.yr^{-1}); and compared to the mean of all central Alps glaciers of -1.06 ± 0.04 (m w.e.yr^{-1}) the rate is lower (Zemp et al., 2025). The reason for this might be its high elevation area and the thickness changes. This result is similar to the trend which is found for all Swiss glaciers (GLAMOS, 2026), where 5-7 meters per year was measured. These findings show evidence of climate change and the effects which global warming has on glaciers (Huss et al., 2017; Linsbauer et al., 2025; Zemp et al., 2025)

6.1.1 Subsurface ice

The values of the volume estimation underlay uncertainty about the ice content in the moraine and the slopes. It is difficult to estimate the volume balance since the boundary

between the glacier and the moraine material is unclear. Besides glacier thinning, subsurface ice melt also negatively affects the mass balance. It is common for talus slopes to contain ice at the toe, ice lenses, and ice-cored moraines (Lukas et al., 2012; Shroder, 2013). Boulder falls and toppling from further upslope add to the uncertainty about the elevation changes (comparefig. 3.6 used for the calculation). This is especially relevant at the slope toe, where numerous rockfall events were observed. The addition of material from upslope is considered negligible, since none of the DOP images showed significant accumulation of material at the slope head.

The subsurface ice melt is likely to be observed in the moraine zone during the period 2012–2016 (fig. 5.8 A). In later years, this signal is still visible, but numerous rockfall events increasingly influence the surface elevation through accumulation of material at the slope toe (fig. 5.8 B, C). It is also possible that subsurface ice is present in the slope above the slope toe. Since the strongest elevation decrease over the entire study period is observed on the right side of the slope toe, even during years of relatively low movement. However, there are no signs of water discharge at the slope toe. If subsurface ice melting would occur, water would typically darken the moraine material which was shown by Alexander Ruff (2015) at lower elevation at the moraines (seen in Appendix fig. 7.13). This was not observed in the collected DOP imagery. However, this ice melt process may also be seasonal and therefore not observable at the time of image acquisition, but would be expected in late summer. As Langston et al. (2011) showed in their study on the internal structure of alpine proglacial moraines, ice content is highly variable, and the groundwater flow or meltwater system within a moraine is complex, depending on the morphology of the slope and the material composition. It is therefore possible that meltwater does not emerge at the slope surface and is therefore not observable, even if melting is indeed occurring.

The presence of ice is considered likely, as Gärtner-Roer et al. (2022) showed during glacier advance phases. Glaciers can push the permafrost body up. This process potentially could form rock glaciers and moraine complexes with ice content. Their study examined the Gruben glacier and the periglacial environments, where the accumulation of debris also contributed to the insulation of the ice, leading to the persistence of ice-rich debris in proglacial areas and the margins of the glacier. At the Findel Glacier, this scenario is possible since the glacier experienced multiple advance periods (e.g. LIA, early 1920s, global dimming in 1980 fig. 3.2). However, the last time the glacier had reached the currently active slope foot was during the Little Ice Age (LIA). It therefore remains unknown how much ice is stored within the slope. In steep alpine rock slopes, permafrost can reach considerable depths (Hasler et al., 2012), implying a potential presence of ice in considerable depths.

With this in mind, most of the unexplained negative mass balance at the slope can be attributed to glacier ice melt. However, the negative mass balance pattern did not follow the Findel Glacier mass balance changes. The period 2016–2020 showed the highest net loss in the slope mass balance, whereas the glacier showed its highest mass balance changes in

2020–2024. The Findel Glacier mass balance reflects changes over the entire glacier surface, which may vary strongly in local ice thickness, particularly where the glacier is covered by debris. This may explain the discrepancy between ice melt in the moraine zone and the overall glacier mass balance changes. Ice stored within moraines should respond more slowly to warm years, as it is less exposed to meteorological factors than bare glacier ice.

In summary, subsurface ice is likely present, but no clear surface indicators of active melting processes were observed. The ice content may therefore be lower than expected. In many other studies, where ice content was high, traces of water were visible at rock faces or in debris (Walter et al., 2020; Huggel et al., 2010; Fischer et al., 2010).

6.1.2 Hazard potential

The two study slopes, which were shown to be unstable, were dominated by processes of the gravitational and periglacial domains, respectively. The estimation calculated via the DoD yielded a displaced volume of $932\,283.8 \pm 29\,042$ m^3 for the Innere Rimpfischwäng slope and $142\,894 \pm 4\,223$ m^3 for the Tripfen slope. Compared to recent events such as Blatten last year or Piz Scerscen, which contain 6.4 million cubic meters and 8-9 million cubic meters (Daniel Farinotti et al., 2025), respectively, it is rather small. However, it could potentially start a cascade of events, such as liquefaction of the slope material due to melting of glacier ice during a collapse. Hence, it might lead to a very dangerous hazard scenario. In the case of Blatten, the rock mass only reached the village as fast and destructively because of its high water content (Daniel Farinotti et al., 2025). The same is true for the IR slope: in the unlikely case that the rock masses would deposit on the glacier and lead to a collapse, the mixture could as well reach much further distances than without the water content. A key difference the Findel Glacier is not situated on steep topography as the Birch glacier. However, the area remains dangerous through glacial lake outburst flood (GLOF), a dangerous hazard in high mountainous environments (Taylor et al., 2023). The Tripfen rockslide does not pose any threat to the surrounding area since it has almost settled at the valley floor, and the presence of ice is minimal compared to the glacier above. The IR slope is close to the mountain fall and therefore needs to be monitored carefully. Compared to rockfall inventories reported in the literature, the estimated displaced volume falls within the range of large but documented mass movement events. Dussauge et al. (2003) compiled rockfall volumes spanning several orders of magnitude, reaching up to 10^9 m^3. The volume estimated in this study is therefore considered plausible within this context.

6.1.3 Mass movement dynamics

A very different acceleration dynamic was identified. At the IR slope, major acceleration phases were observed in 2017–2019 and 2023–2024, while the Tripfen slope showed a con-

tinuous decrease in movement until the final years of the study period. Fu et al. (2024) analysed landslides in Three Gorges Reservoir (China). The landslide also showed episodic movement dynamics. Compared to IR, slope morphology is different, and they found more steady-creep dynamics than acceleration phases and stable states. Through measurements with high temporal resolution, they could attribute their episodic movement to either rainfall events or water level changes in the reservoir (Fu et al., 2024). Which is very diffrente to setting found at Findel Glacier. A study by Notti et al. (2021) in the Ligurian Alps looks at a deep-seated landslide. They could attribute the episodic dynamics of the landslide to changes in the groundwater table and rainfall events. The temporal resolution of our feature tracking is not sufficient to find similar things as well. The reliability of the feature tracing was assessed through control measurements. They confirm the reliability of the findings and the accuracy of the feature tracking results presented in this study. At the Tripfen slope (fig. 6.1b), only one boulder located in the periglacial zone was slowly moving, which is likely due to ice present in this block field. Therefore, the boulder was also mapped as part of a rock glacier (see fig. 5.3). To confirm this, in-situ measurements are needed. At the IR slope (fig. 6.1a), boulders in the slope crown above the scarp were selected. The bedrock itself was never tracked, but appeared very stable in the DOP imagery. Some boulders exceeded the uncertainty range and were therefore truly in motion, undermining the idea that small-scale rockfalls or boulder displacements occur over the years. For example, Boulder 32 is located at the slope crown (see fig. 6.1a). It is a large boulder situated in fine material, which could gradually reduce the support beneath the boulder. However, it does not follow the movement pattern of the slope body, even though its highest velocity occurred between 2018 and 2019. However, the boulder showed an additional velocity peak in 2015–2016. Overall, it exhibited higher velocities during periods of low activity in the main slope body; it appeared to be driven by an independent process (physical erosion, rain mobilisation, frost-related processes). It would be interesting to observe how the boulders at the slope crown evolved over the last three years, but the DOP image extent no longer covers this area.

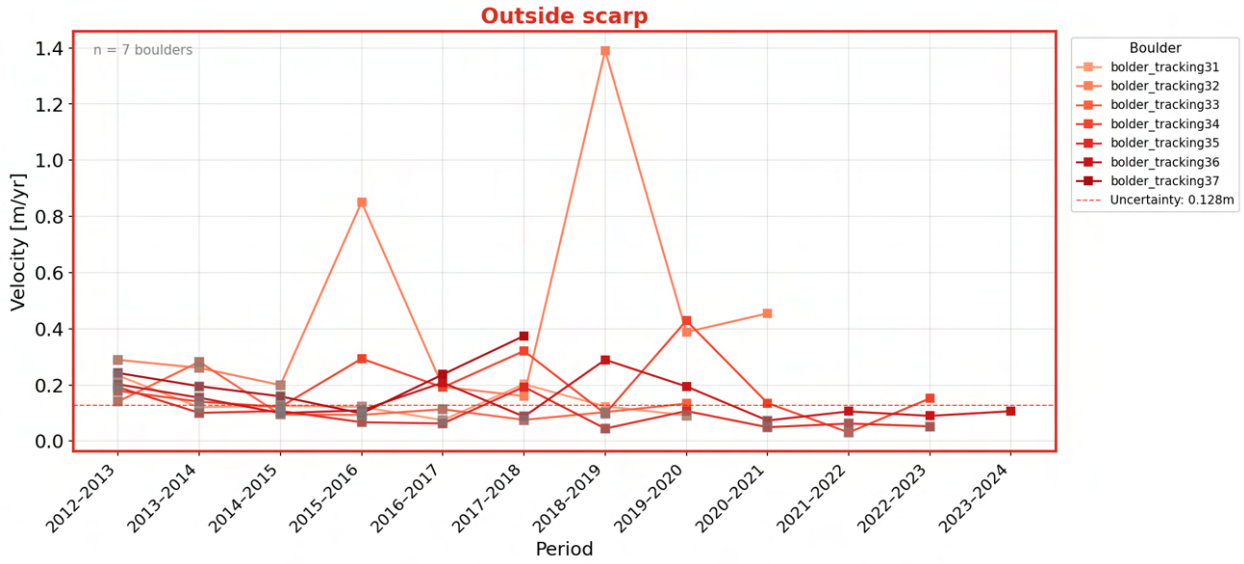

(a) Boulder velocities of the seven control boulders located outside the IR scarp over the study period 2012–2024. Boulders in the upper slope area fall outside the orthophoto coverage and are therefore absent from 2021 onwards.

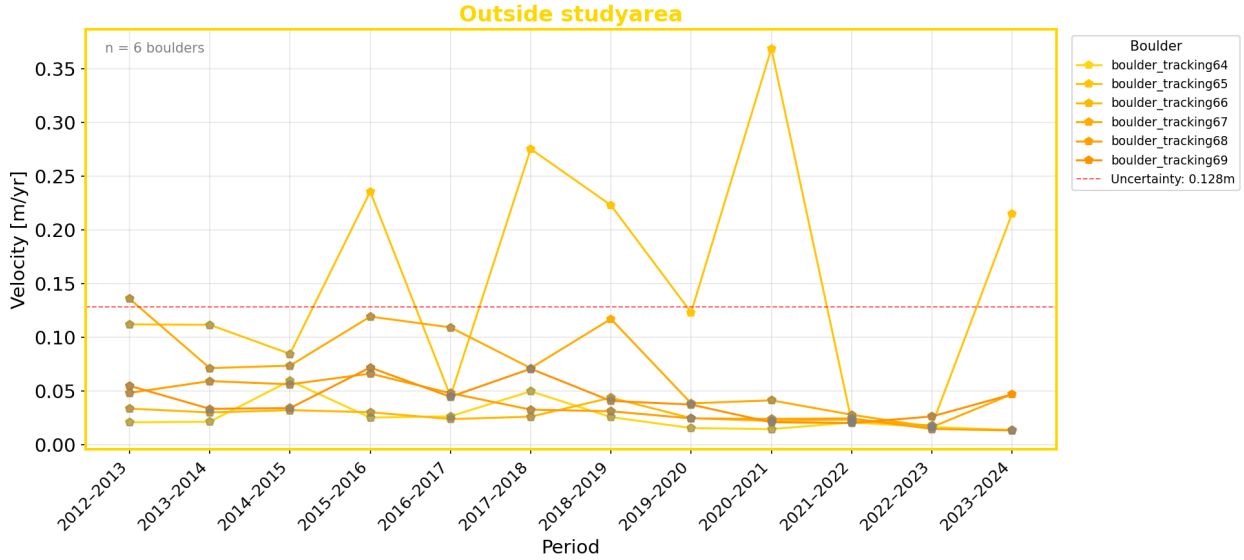

(b) Boulder velocities of the six control boulders located outside the Tripfen slope over the study period 2012–2024.

Figure 6.1: Control points for Tripfen and Innere Rimpfischwäng slopes.

These control measurements support the velocity assessment, underlining that we indeed observed phases of acceleration and deceleration at the IR slope.

Regarding the methodology of point tracking, human uncertainty was introduced during the picking process. When pixels showed no visible movement, the point was placed as close as possible to the previous position, which is why zero velocity is never recorded, even though in most cases the movement is undetectable or effectively zero. The true velocity may

therefore be lower than the depicted values since the picking added artificial displacement. In some cases, boulders began to rotate, meaning the same point could no longer be picked reliably or was less representative of the actual ground motion. However, this uncertainty was never formally quantified since no science-based approach was available to estimate it. Since these errors are rather small, they should hence be accounted for with the implementation of a minimal detection level.

Another aspect that is only poorly accounted for is the boulder size. Large boulders have greater inertia but also greater gravitational potential. These two effects are assumed to largely counteract each other, though this has not been formally verified. For some boulders, the actual size is unknown without field measurements, though it could be estimated. This effect is not commonly addressed in boulder tracking studies (Dewez et al., 2010; Knight et al., 2023). It should be noted that Knight et al. (2023) investigated boulder movement dependent on wave energy, which is not directly applicable to this context. But they also just measured the displacement as a proxy for wave power. It can be stated that larger boulders have greater momentum when in motion (Shroder, 2013), but since these are not rockfall events, this cannot be directly applied. This, therefore, remains a residual uncertainty of the method, although its impact on the velocity estimates is considered minimal.

6.2 Drivers of slope instability

In this thesis, possible drivers of mass movement, such as Geology, permafrost and glacier retreat, and meteorological conditions, were analysed. Based on these assessments of factors and patterns, a mass movement type can be estimated.

6.2.1 Geology

The many studies highlight the importance of geology in slope stability (Stead and Wolter, 2015; Agliardi et al., 2001; Notti et al., 2021). Especially the presence of discontinuities and transition zones between different rock lithologies is important for the stability of the rock body (Agliardi et al., 2001; Stead and Wolter, 2015). At the two study sites, this discontinuity of different lithologies is present. At the Tripfen slope, a transition from quaternary moraine material to eclogite-amphibolite is present. At the IR slope, another transition from eclogite-amphibolite to serpentinite bedrock is present. These transitions can be seen in fig. 6.2 and are likely to lower the slope stability of these two slopes.

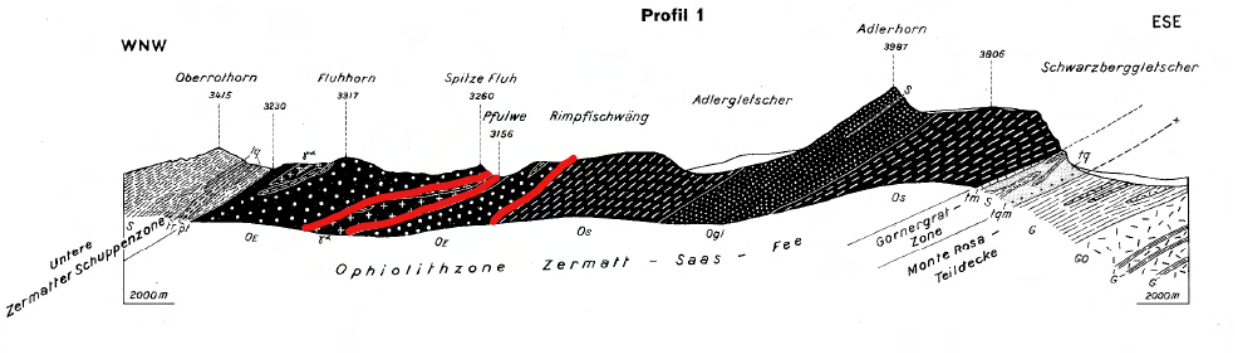

Figure 6.2: Geological cross-section along profile 1 as indicated in fig. 3.9. The profile extends from WNW (Oberrothorn) to ESE (Schwarzberggletscher), crossing the Ophiolith zone Zermatt–Saas–Fee. Red lines highlight the lithological transition zones relevant for the IR and Tripfen slopes. This zone is also known as the Zermatt-Saas ophiolite zone (ZSZ). Figure adapted from Bearth (1953).

On aerial images, serpentinite appears more disintegrated than eclogite (see fig. 6.3). This is associated with lower surface rock mass quality (Hoek et al., 2000), and therefore, this geological setting could represent a preconditioning factor that makes slope stability more susceptible to failure. The serpentinite formation could act as the rupture surface below the moving mass. However, this cannot be verified from the Geological Atlas of Switzerland alone. In-situ measurements are needed to confirm the subsurface geometry and lithology of the slope.



Figure 6.3: Serpentinite looks more disintegrated (red) than the eclogite (orange) rock formation

For the Tripfen slope, the development of the new scarp may follow a similar mechanism to the IR slope. The key difference is that the Quaternary moraine material forms the moving mass on top of what is presumably the eclogite bedrock. There is also a bigger lithological difference between a metamorphic rock structure and a weaker rock structure, like the Quaternary moraine material. In summary, the lithological transition follows the scarp on both slopes. This indicates that the geology plays an important role in the stability of both slopes. Slope instability is facilitated due to the structural characteristics of the geological formation.

6.2.2 Permafrost thawing

There is a high likelihood that permafrost is present at the IR slope (seen in the purplish colours of fig. 6.4), particularly in the slope crown where the main scarp is located and where extensive permafrost is likely.

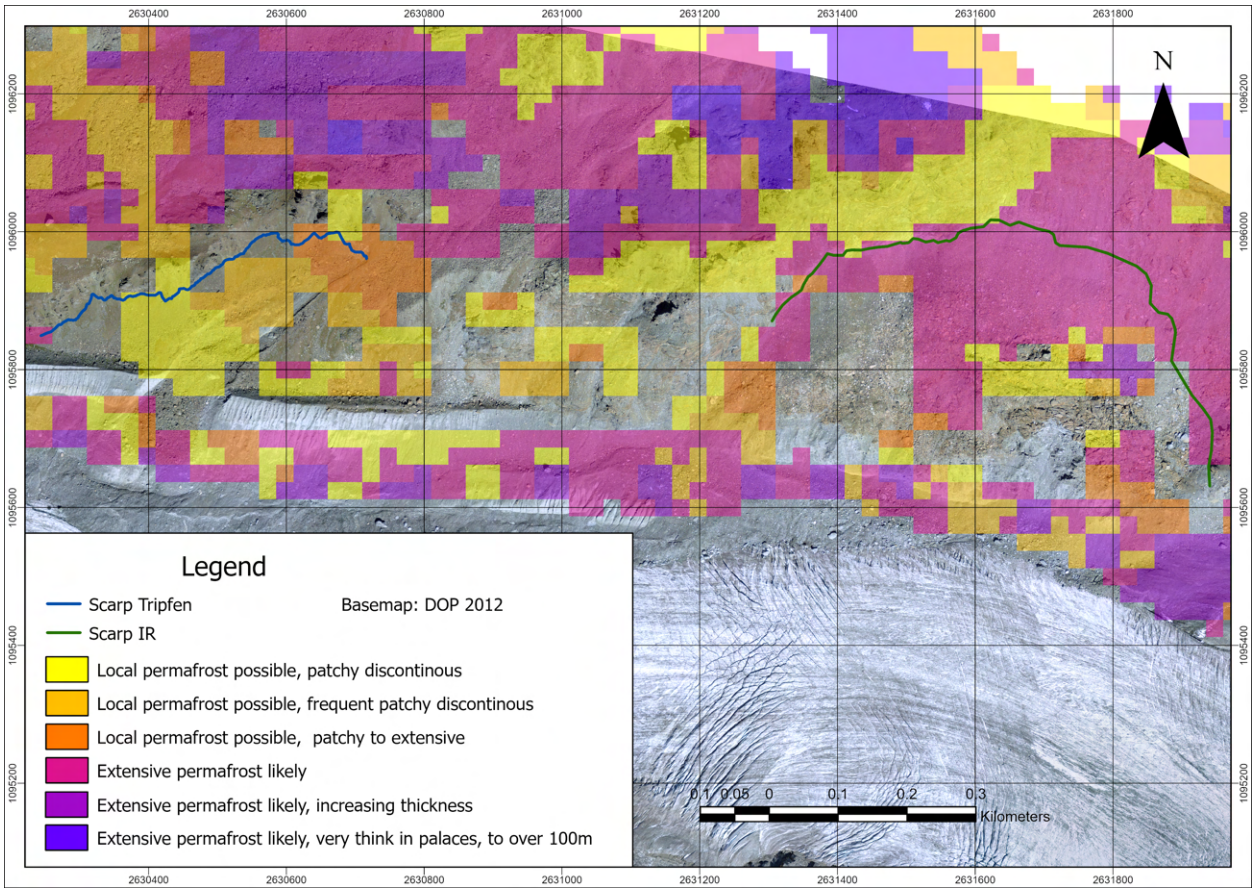

Figure 6.4: BAFU Permafrost distribution map created by Gruber, S et al. (2006). The map illustrates possible ground conditions at the study slopes (open available from BAFU (2011)).

At the right slope foot, snow may persist longer than at other parts of the slope, allowing water to penetrate deeper into the slope body later into the season than at the left side.

Which would affect the groundwater table or deeper permafrost ice to thaw or warm. A further permafrost map from SLF fig. 6.5, which also considers sediment and site conditions related to snow transport, indicates that the rock glaciers contain ice-rich permafrost. It is therefore also possible that the slope foot contains areas of ice-rich permafrost.

At the Tripfen slope, permafrost distribution is very sparse, with only the uppermost part of the slope showing any possibility of permafrost presence (fig. 6.5). The rock glaciers above the slope likely have ice-rich cores. However, since the Tripfen slope is located at lower elevations, temperature conditions are unlikely to favour year-round frozen conditions.

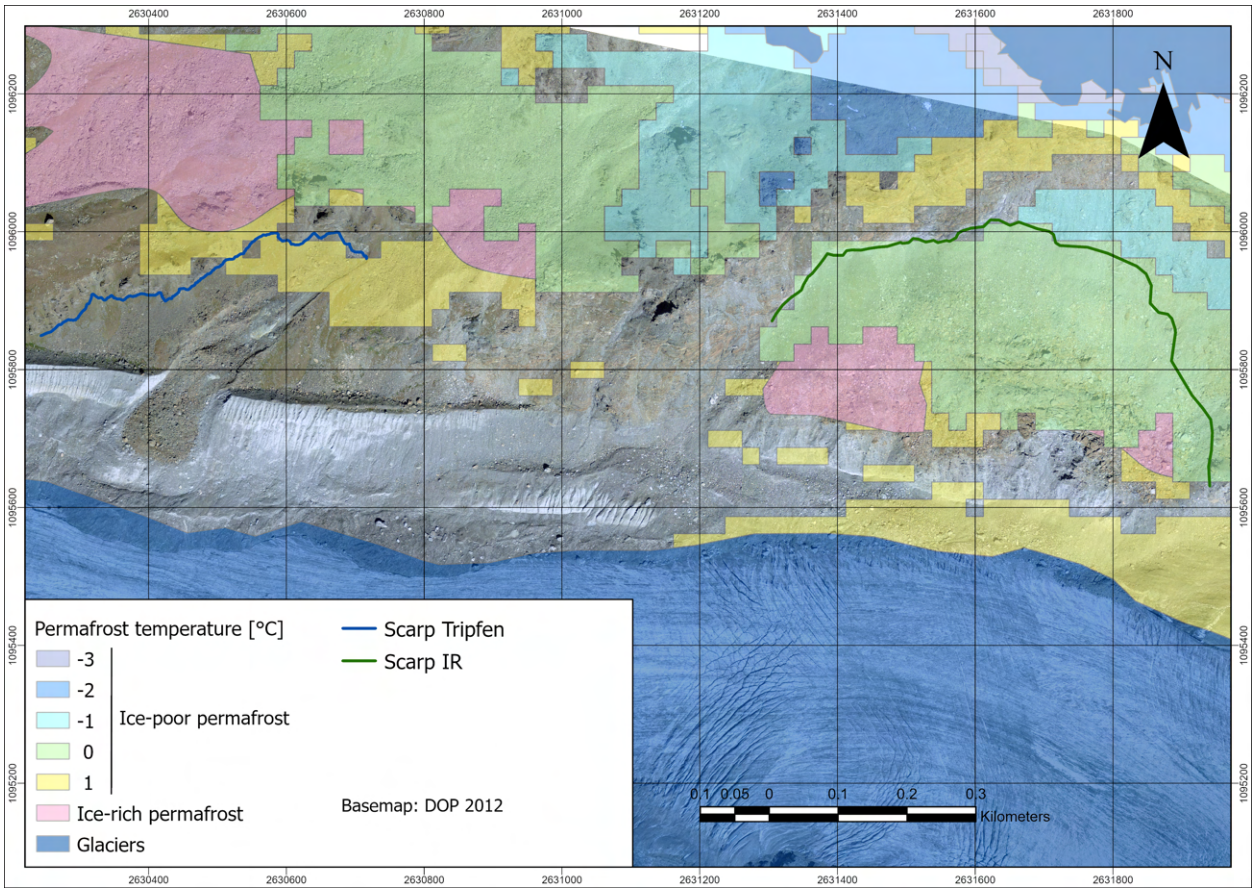

Figure 6.5: SLF Permafrost distribution map for ice-rich and ice-poor permafrost map created by Kenner et al. (2019). The map illustrates possible ground conditions at the study slopes (open available from Robert Kenner (2019).

Both maps indicate that permafrost is very likely present at least at the IR slope and therefore has an effect on slope stability. Thawing permafrost conditions could have weakened slope stability over time, as many studies showed (Davies et al., 2001; Huggel et al., 2012; Krautblatter et al., 2013). The shear strength of frozen rock is lower than that of unfrozen rock. Krautblatter et al. (2013) have shown that rock joints exhibit up to 15% less friction when frozen. This reduction in frictional resistance decreases the overall resisting forces within the slope, making permafrost-affected slopes more susceptible to failure. A

study by Kunz and Kneisel (2020) showed that the presence of ice-rich permafrost is associated with a continuous movement pattern. In their study, they looked at a moraine complex containing massive ice cores and rock glaciers in the Turtmann Valley and Lötschental. Using electrical resistivity tomography (ERT), they characterised the ice content of these two geomorphological features. Their study showed that the thrust moraine complex had a massive ice core body, compared to rock glaciers, which contained less ice but were more heterogeneous in rock material composition. Additionally, the thrust moraine complex showed strong seasonal variability in movement and melting, compared to rock glaciers, which showed a more continuous movement pattern (Kunz and Kneisel, 2020). It is unlikely that the study site contains a thrust moraine complex, but the presence of ice-rich permafrost is possible, as shown in fig. 6.5. Therefore, in addition to mass movement processes, permafrost creep could contribute to the movement of the slope, even though it is below the detection threshold of the imagery. Furthermore, the seasonal signal of the movement cannot be distinguished in this study since the dataset consists of annual images. In summary, permafrost can have a strong influence on the movement and instability of the slope. However, the full extent of permafrost and its effect on slope movement cannot be determined from the available data.

6.2.3 Glacier debuttressing

Another possible driver is a substantial decrease in ice thickness. The Findel Glacier lost less ice between 1864 and 1970 (fig. 6.6) compared to modern times, where approximately 25–50 metres of ice thickness was lost over the time span of 100 years. It must be noted that during this period, the glacier experienced phases of both advance and retreat (compare to fig. 3.3). The elevation estimates are most likely an underestimation of the ice thickness, as they rely solely on extrapolations from older maps without elevation values. Since at the time of the first documentation of glaciers, the Dufour map (1864), the ice reached the slope toe but never the upper parts of the slope. The Adler glacier contributed significantly to the shaping of the slope over a long period and brought debris from the Rimpfischwängi ridge.

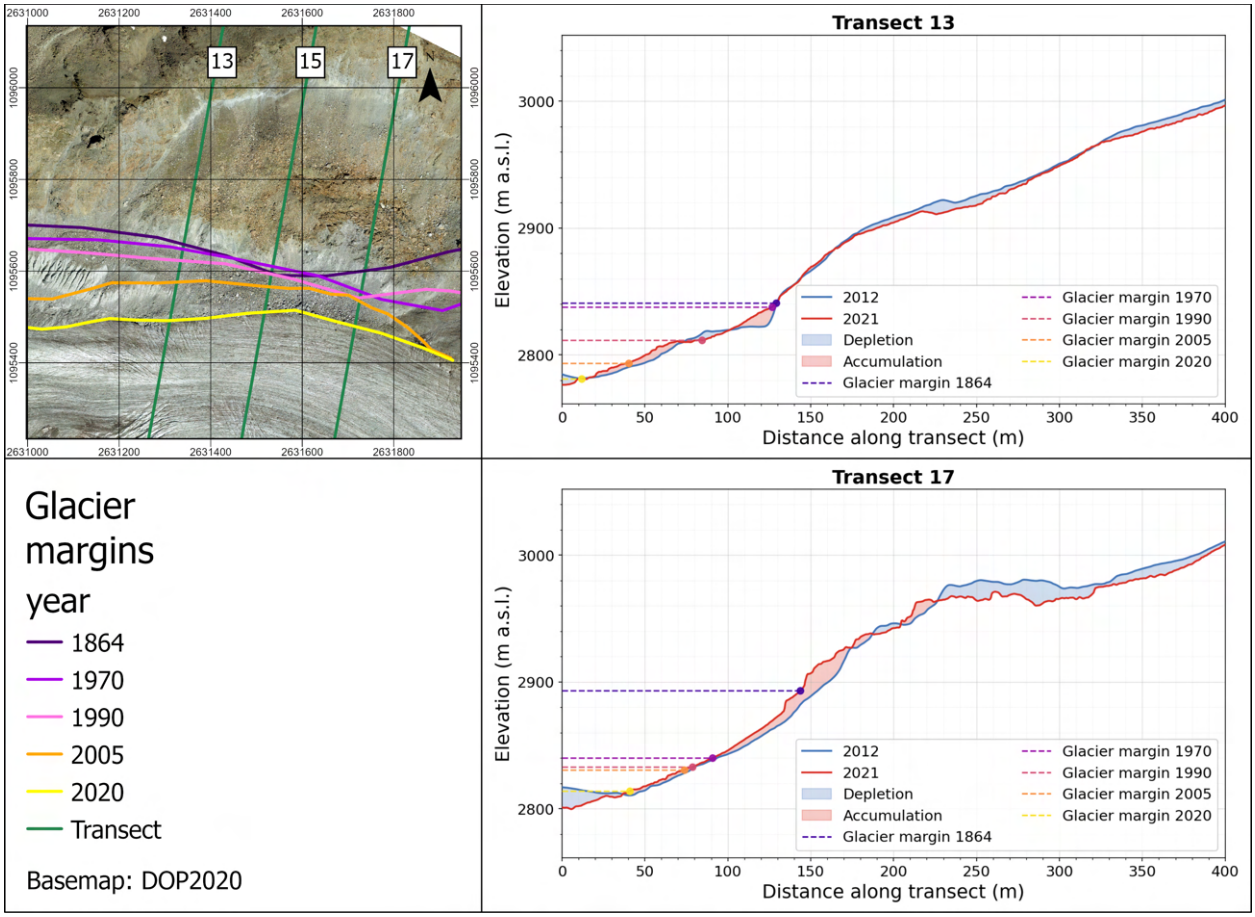

Figure 6.6: Evolution of glacier margins between 1864 and 2020 for transects 13 and 17 showing the lateral support loss.

Therefore, the glacier ice could have provided support for the slope, particularly at the right slope foot, where the glacier surface was even higher. Since the Adler glacier has retreated, the support from the right side of the slope has been reduced, and slope adjustments were visible in the imagery. However, the glacier ice may also have acted as a dam, providing lateral confinement to the slope material. With the retreat of the glacier, this confinement was lost, and the slope material could adjust into the newly available space. This damming effect is also described by Grämiger et al. (2017). In their study, fracture and damage processes were identified as effective mechanisms of slope destabilisation. However, since their study assessed this process on bedrock, and the IR slope is not one coherent body of bedrock, this process is expected to be less pronounced.

As some studies mention (e.g. Curry (1999); Ballantyne (2002)), the transition from a glacial to a paraglacial landscape for debris-mantled slopes, which is the case for the IR slope, takes 50–200 years. The IR slope is still predominantly influenced by glacial processes, even though the glacier no longer reaches the slope directly. Slope adjustment to debuttressing and glacial recession is therefore still ongoing and difficult to quantify. Changes in the slope hydrology, this means changes in the groundwater level, seasonal recharge and long-term

hydromechanical effects (altering effective stresses in rock joints), are very likely to affect the slope stability. These factors are known to be very effective drivers of slope instability (Grämiger et al., 2020).

Glacial debuttressing therefore has an effect on the slope, but likely not through the direct loss of mechanical support, but rather through changes in the groundwater table and the exposure of previously glacier-damaged sediment.

6.2.4 Meteorological conditions

The direct effects of temperature and precipitation are often found as triggers of landslides (Ravanel and Deline, 2011; Huggel et al., 2012; Fu et al., 2024). In the fig. 6.7, the slope velocities and the respective temperature (Gornergrad station) and precipitation (Findelbach) values are shown. The annual mean temperature (corrected to IR slope) between 2012 and 2024 varied between -2°C and 0.5°C, with strong seasonal oscillations (additional figures-fig. 7.10). Annual precipitation over the image acquisition period varied between 600 and 1000 mm (fig. 6.7 D), with high seasonal variability and no clear pattern of distinguishing a wet season (seen in appendix fig. 7.11). The study period was also drier than the WMO reference period by 143 mm. In 2013 and 2014, when the Findel Glacier had a positive mass balance, precipitation exceeded the reference value. The following nine years were substantially drier. During the study period, temperatures were overall higher than the climatic mean temperature (fig. 6.7 C). No strong correlation between slope movement and these meteorological measures was identified (seen in appendix fig. 7.12).

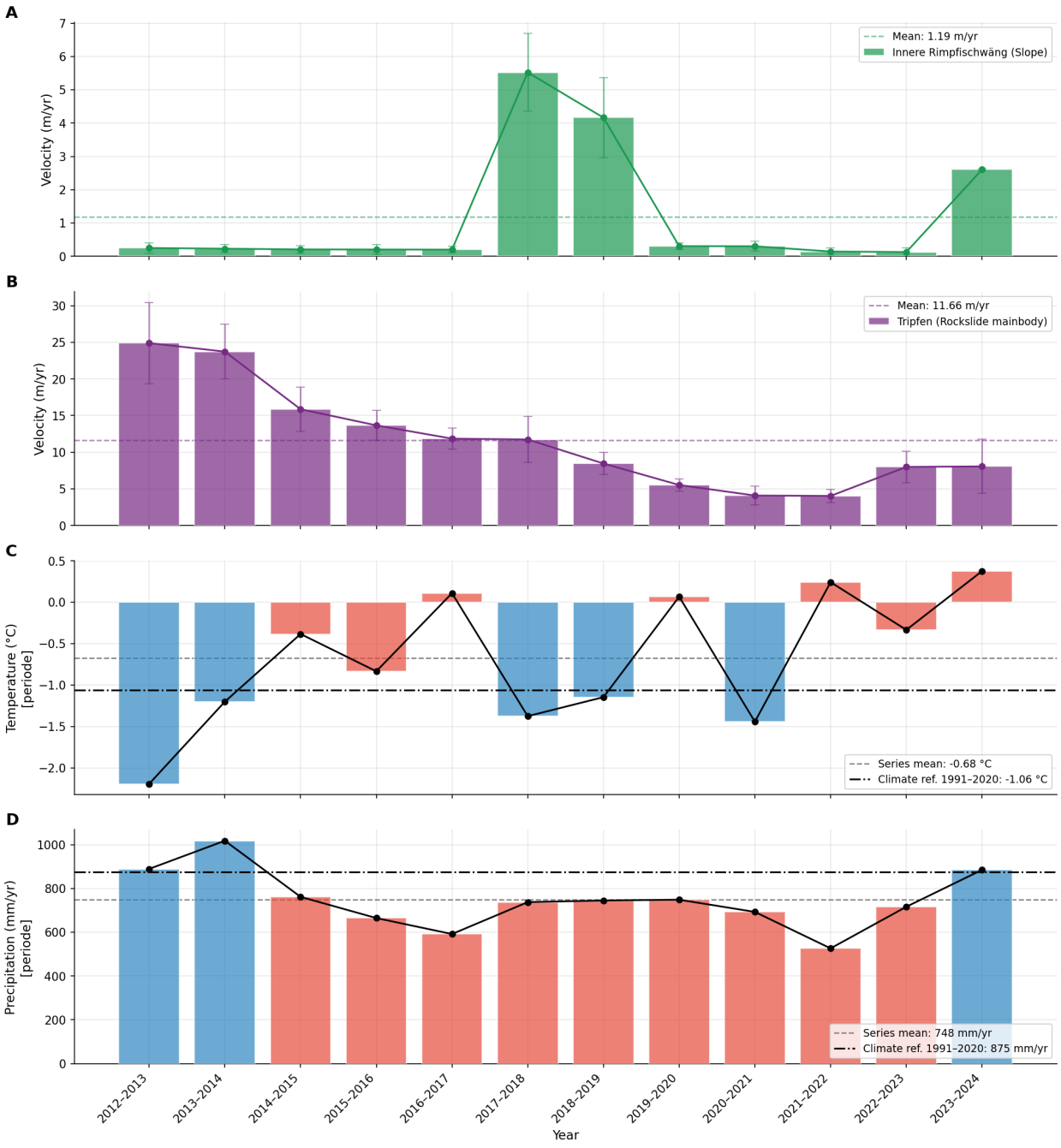

Figure 6.7: A: IR mean slope movement, B: Tripfen rockslide movement, C: Mean temperature over study period and WMO climate reference (1996-2020), D: Mean precipitation at Findelbach station over the study period and WMO climate reference (1990-2020)

However, as some studies from Ravanel and Deline (2011) found, heat waves can cause more frequent rockfall. These events are below the temporal resolution of DSM and DOP images. However, in 2017 and 2018, Valais experienced three heatwaves. The summer of 2018 was extremely hot and dry from July to August (MeteoSchweiz, 2017, 2018). 2024 was also a very warm year with the second hottest August, where new heat records could be registered all around Switzerland (MeteoSchweiz, 2024). However, to the average summer

climate, these years are not outliers in the warming climate (see fig. 6.8). Although no significant correlation between summer temperature and slope velocity was identified, it cannot be excluded that short-term heat wave events triggered individual movement phases. However, since heat waves also occurred during years of low slope activity, they are unlikely to be the primary driver of the observed acceleration phases.

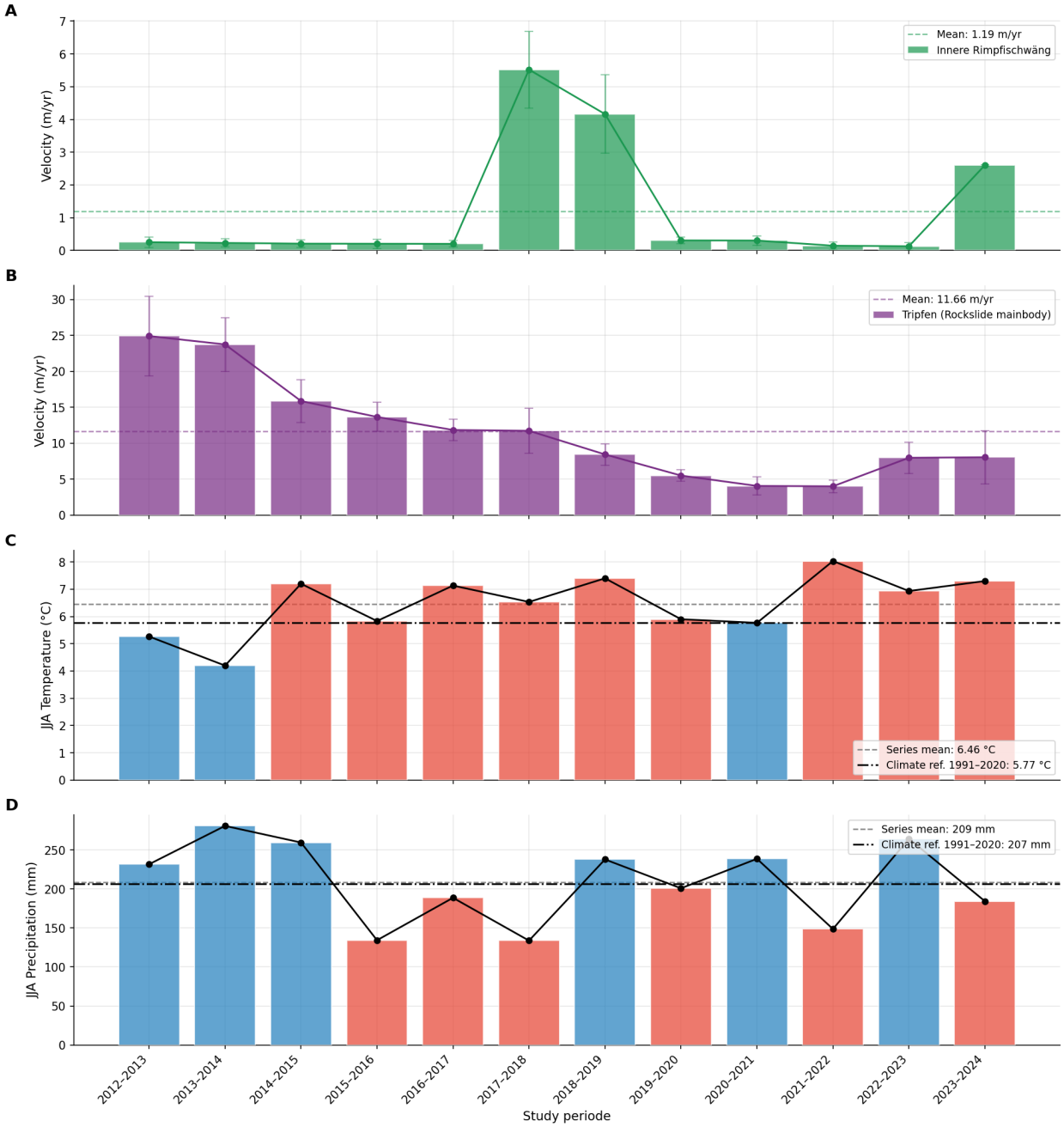

Figure 6.8: A: IR mean slope movement, B: Tripfen rockslide movement, C: Mean summer temperature (JJA) over study period and WMO climate reference (1996-2020), D: Mean summer precipitation at Findelbach station over the study period and WMO climate reference (1990-2020)

The Tripfen rockslide shows a uniform movement pattern and is therefore unlikely to be influenced by meteorological conditions. As gravitation and ice melt contribute more to the movement than the temperature and precipitation. The slope flank slump movement occurred in 2023–2024, which was after the major movements of 2017–2019 at the IR slope. It is therefore very unlikely that the two instabilities are coupled to the same meteorological conditions.

The measurements of precipitation and temperature cannot explain the movement pattern. This makes meteorological conditions a very unlikely driver for these two slopes. However, if we had in situ measurements and more temporal resolution of the aerial images, this driver could be assessed with more certainty.

Even though the two sites are located close to each other, the geology and permafrost settings differ. Glacier retreat is likely to affect only the IR slope directly. Therefore, meteorological variables are the only factors that affect both slopes equally. Based on the results of this study, no common pattern of controlling variables could be identified that influenced both slopes in the same way.

6.2.5 Classification of mass movements

The Tripfen slope showed characteristics of a planar rock slide (Hungr et al., 2014; Varnes, 1978) based on the results gathered section 3.2.2 and is likely to move along a clay-rich planar horizon (see fig. 6.9). The planar rockslide showed a higher movement rate at the beginning and a slowing down when settling at the valley bottom. Unlike classic planar rockslides, which typically fail as rapid, coherent collapses, the Tripfen rockslide is comparatively slow. One key difference from a classic planar rockslide is that the rock mass is not one coherent body. It consists of many smaller boulders of the same rock type (section 2.3.2.2), which may explain why it is relatively slow compared to other mass movements.

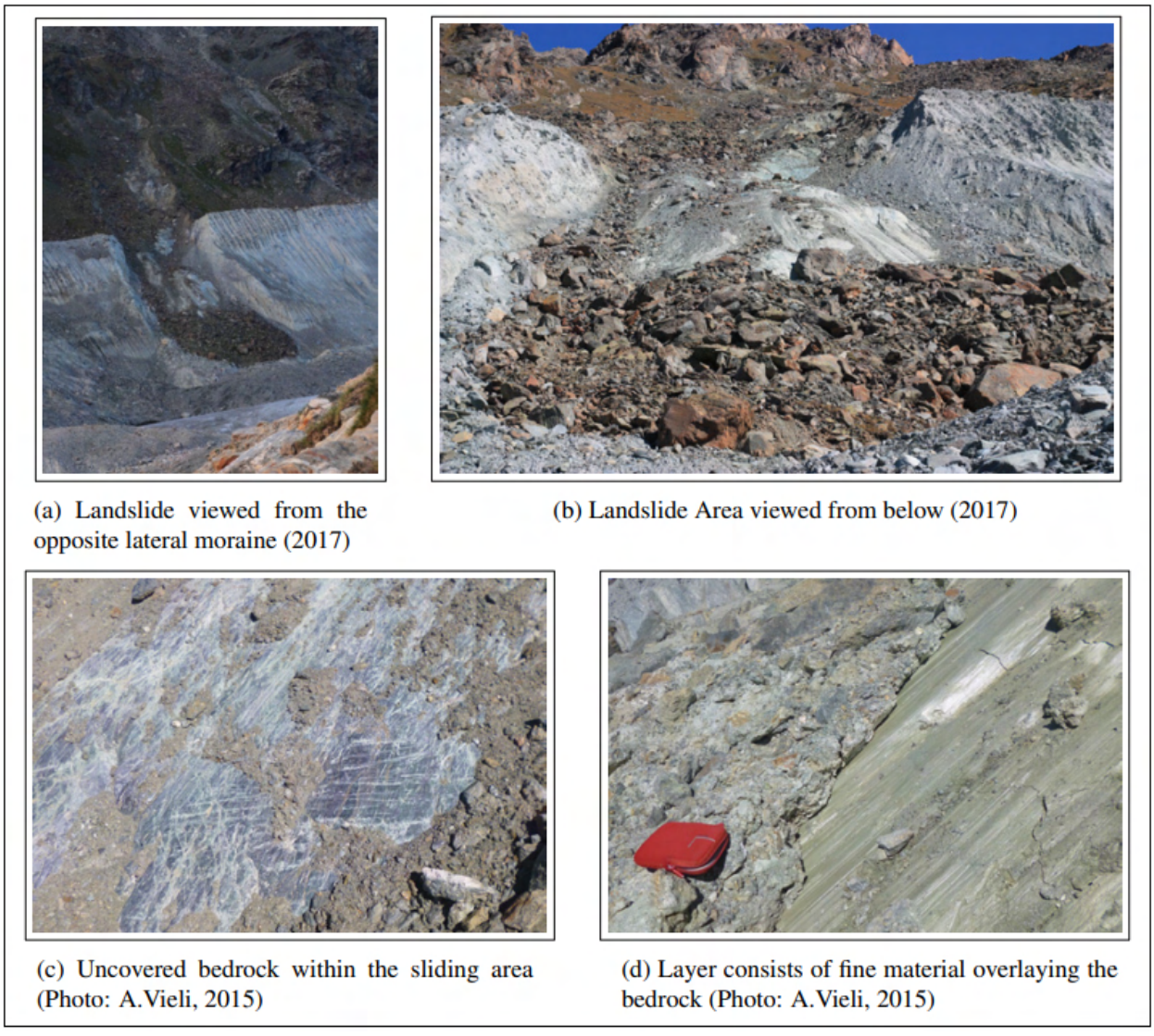

(a) Landslide viewed from the opposite lateral moraine (2017)

(b) Landslide Area viewed from below (2017)

(c) Uncovered bedrock within the sliding area (Photo: A.Vieli, 2015)

(d) Layer consists of fine material overlaying the bedrock (Photo: A.Vieli, 2015)

Figure 6.9: In-situ photos (a, b) of the site at different times during field study of Christine Schärer (2018). c/d show possible clay horizons.

The Tripfen rockslide was studied previously by Christine Schärer (2018). The Rockslide, which started around the years 2005–2009, resulted in the breach of the moraine in the following years. The initial rockslide area was consistent with the release area identified in this study. There was no conclusion drawn about the trigger of the initial rockslide by Christine Schärer (2018). As it can be seen on the Swisstopo SWISSIMAGE Zeitreise between 2008 and 2009 (swisstopo, 2026), a scarp was visible at approximately the same location (fig. 6.10). This could indicate that the slope flank scarp initially triggered the rockslide.

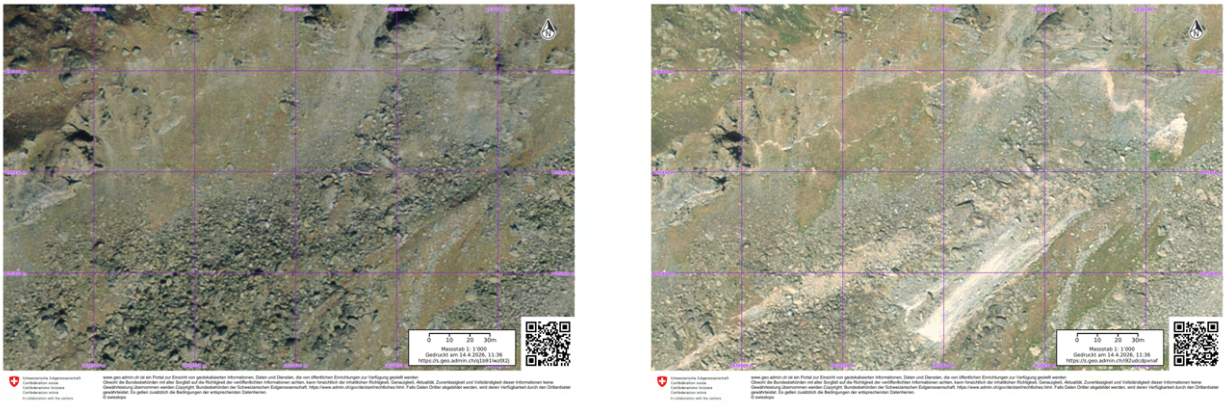

(a) Tripfen slope flank and release area in 2006

(b) Tripfen slope flank and release area in 2009

Figure 6.10: Tripfen slope flank and release area in 2006 and 2009.

In the Swisstopo SWISSIMAGE Zeitreise (swisstopo, 2026), the scarp of the IR slope was also visible before the study period. The first signs of the scarp were visible in the imagery from 1990. In the image from 1999, the scarp seems to expand along the slope crown and below the steep rock walls on the left hand side. Over the following 18 years, it did not appear very pronounced, though there are data gaps of 4–7 years between the SWISSIMAGE orthophotos. The rupture line became clearly visible again in 2018, when acceleration of the entire slope took place.

At the IR slope, it is more complicated to estimate the type of mass movement. There are indications for three different scenarios (fig. 6.11).

Other than at the Tripfen slope, it is unknown where the rupture surface is. Depending on the depth of the rupture surface, the mass movement category changes. The first scenario is a shallow rockslide. This would mean the rupture surface would be only 2–4 metres deep, and the material transported downwards would accumulate at the lower part from material above. Based on the DoD, it is rather unlikely that this is the case since the movement pattern seems to be affecting the whole slope at the same time. This would imply that the whole slope moves along a deep rupture surface. This is what the second scenario depicts: a rotational rockslide. where the entire rock body rotates along the rupture surface. However, it does not look like a coherent rock mass as the classification described by Hungr et al.

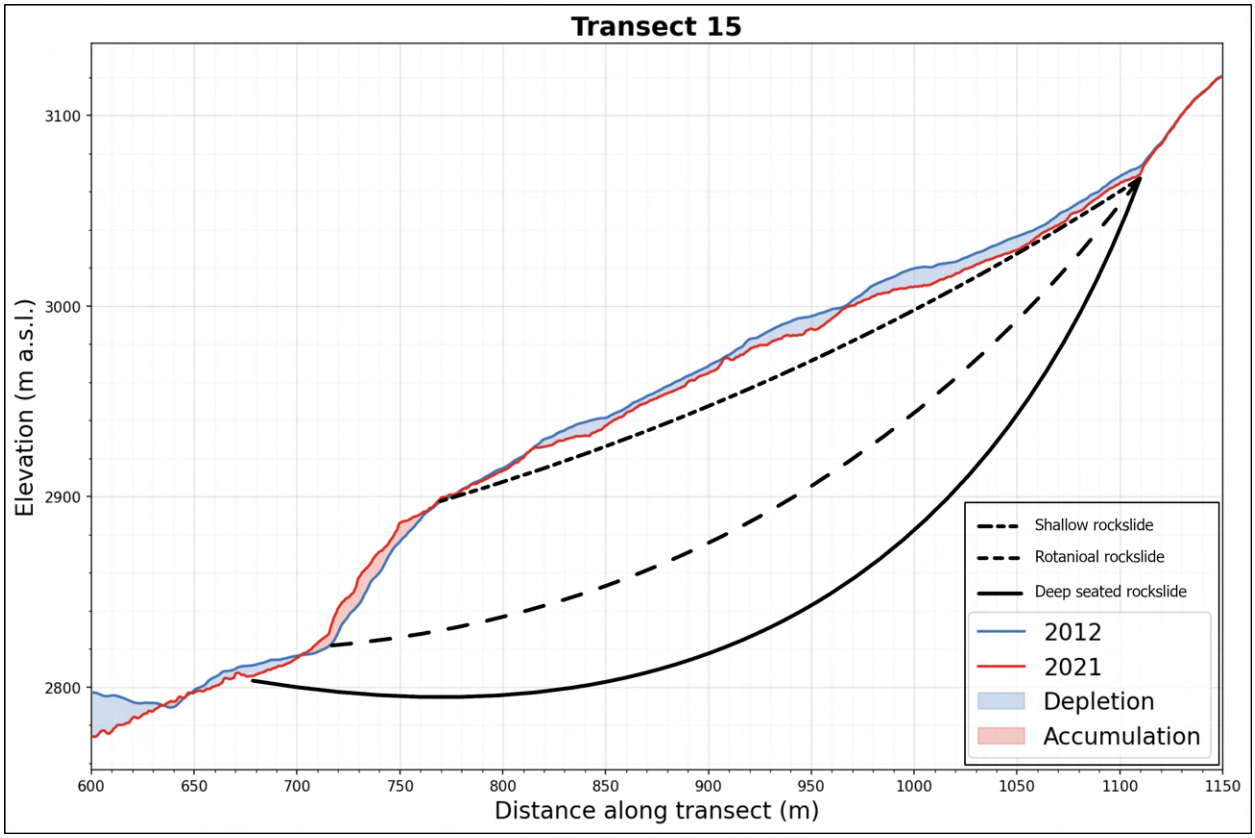

Figure 6.11: Three possible mass movement scenarios at the IR slope.

(2014); Sousa et al. (2021). The estimated rupture surface toe is located approximately where the slope toe meets the moraine (fig. 6.11). Some features are very similar to this scenario, such as the slope foot advancing forward over time. The third scenario is a more deep-seated rockslide /slope deformation, where the moving body is considerably larger than in the other two scenarios. The elevation gain observed in the moraine zone would support this scenario, where the deep-seated rockslide would uplift the finer moraine material (compare to fig. 5.8). Without in-situ measurements, all three scenarios are theoretically possible. But there are numerous studies (Notti et al., 2021; Pánek and Klimeš, 2016) which found similar feature found as here. These deep-seated landslides, slope deformations, rockslide are common in high alpine environments.

6.3 Limitations and outlook

The most significant limitation is the lack of temporal resolution of the aerial images. Therefore, it is not possible to link single meteorological events to the mass movements. Which are typically the triggers for the processes (Allen and Huggel, 2013; Fischer et al., 2010; McColl, 2012; Hsieh et al., 2016). Higher temporal resolution imagery combined with GPS monitoring of individual boulders would allow direct measurement of movement rates and help identify meteorological triggers more reliably than the indirect approach applied here. In-situ measurements would further address the remaining open questions regarding subsurface conditions. Electrical resistivity tomography (ERT) could characterise the distribution of subsurface ice and permafrost, while ground temperature measurements would provide insight into the thermal regime of the slope and state of permafrost and provide an indication of how close the slope is to new acceleration or if the slope in more settlement phase. These additional measurements could provide new insight on the potential rupture surface and the geological setting below the debris-mantled slope. Hence, a more robust assessment of the rupture surface geometry and the role of permafrost as a preparatory factor is possible.

Other factors operate on different timescales and therefore remain difficult to assess. Without in-situ measurements, it is not possible to test hypotheses regarding the role of permafrost and debuttressing. Many studies have shown that these processes nonetheless have an effect on slope stability (Cossart et al., 2007; Fischer et al., 2006; Huggel et al., 2010). Each slope has a different history, and some are still in the process of adjusting to the Little Ice Age (LIA) (Cossart et al., 2007; Fischer et al., 2006). That's why these effects can not be measured on these short time scales.

There is also the uncertainty of the co-registration. The code could be improved, resulting in more accurate estimates of the elevation changes. There are shifts visible in the DSM that are unlikely to be of natural origin. For example, in the overview fig. 7.8, an increase in material is visible on the left side of the slope foot and on the right side of the slope head. However, no signs of increased rockfall or material accumulation were observed in the DOP imagery. This slope was not masked out since only the glacier was expected to show large changes. With an updated mask excluding this slope, the DoD analysis would be less affected by co-registration artefacts. In general, errors of this kind are common in steep terrain (Hugonnet et al., 2022; Romain Hugonnet et al., 2020; Leigh et al., 2009). Additional iterations of co-registration, or the application of more advanced co-registration methods, would likely improve the data quality. The method to quantify the uncertainty level was based on a fixed multiplier applied to the mean slope angle. However, this approach underestimates the error in steep terrain and overestimates it in flat terrain. Overall this would make the estimation of the volume more precise and would eliminated the noise in steep parts which are artificial.

For some geomorphological processes, such as soil creep and permafrost creep, the signal is below the detection range of the uncertainty threshold. Movement rates of these processes within the Swiss Alps are typically around the values of 0.8–1.6 cm yr^{-1} (Matsuoka, 2001; Dikau et al., 2019). This means that any solifluction or creep activity at the study site cannot be detected or quantified with the methods applied in this study. Also, some chemical erosion processes and many frost-related processes ca not be directly measured or shown in the data.

The Tripfen slope is expected to decrease in movement over the coming years as the rockslide continues to settle at the valley floor. The IR slope, however, should be monitored with great caution as mention before, as the large volume of unstable material could be mobilised towards the glacier in the event of a slope collapse, potentially posing a hazard to the Zermatt region. More broadly, understanding how debris-mantled slopes evolve following glacier retreat provides valuable insights into landscape transition and natural hazard management in alpine valleys under ongoing climate change.

Conclusion

This thesis shows that with multi-temporal DSMs, orthophotos and feature tracking, as well as open available data, the geomorphological conditions in high mountain environments can be assessed and provide information about the state of transition of glacial to paraglacial landscapes. This information can support hazard assessment in the future. The 12-year study period (2012- 2024) at Findel Glacier illustrates the complexity of mass movement processes in high mountain environments. In addition to the massive glacier retreat and thickness changes at the tongue, up to 50 m, the proglacial forefield also undergoes active reworking by fluvial and glacial processes. The moraine shows gully erosion and, at some places, lowering of the moraine surface, indicating subsurface ice melt. Changes are not limited to the glacier boundaries but extend beyond the glacier margins, where gravitational and periglacial processes dominate. Common features are small rock glaciers and rockfall debris. The Innere Rimpfischwäng and Tripfen slopes were examined in detail and reveal fundamentally different dynamics. The Innere Rimpfischwäng slope has three distinct phases of acceleration with peak velocities of up to 9 m yr^{-1} during 2017–2019 and 2023–2024 and an estimated displacement volume of $932\,283.8 \pm 29\,042$ m^3 over the study period. By contrast, the Tripfen rockslide ($142\,894 \pm 4\,223$ m^3) shows a continuous deceleration as the rockslide body reaches the valley floor. The rockslide body buried part of the glacier which now has retreated further upwards and is no longer connected with the ice beneath the rockslide body. The dead ice melt, the proglacial lake formation and a partial moraine collapse which is potentially linked to a scarp appearing in 2023–2024 further characterise the ongoing landscape adjustment at the Tripfen slope.

Analysis of the meteorological data revealed no significant correlation with slope velocities, temperature and precipitation. Glacier debuttressing is unlikely to be the driver since the thinning proceeded at a relatively constant rate compared to the episodic acceleration phases observed. However, changes in the groundwater table and the time lag effect could influence the slope stability. The geological setting is favourable for instability at both slopes with their discontinuities of lithologies, as well as the presence of permafrost, and with that, the high likelihood of thawing conditions, may act as a preparatory factor. The results further highlight that attributing mass movement to specific controlling factors remains challenging when relying solely on remote sensing data, as in-situ measurements are needed to constrain subsurface conditions such as rupture surface depth and permafrost extent and temperature. No similar pattern was found in the mass movement dynamics or geomorphological features

of the two slopes. This leads to the conclusion that each slope responds individually to a combination of preconditioning and triggering factors. Therefore, generalisations across sites, even within the same catchment, are difficult. At the Tripfen slope, the primary mass movement is a planar rockslide (Hungr et al., 2014) that breached the lateral moraine. The Innere Rimpfischwäng slope is most likely a deep-seated gravitational slope deformation. The unknown depth of the rupture surface prevents a final classification and further in-situ investigation would be needed to confirm it.

These findings underline the highly individual ways of glacial landscape transitions. A continuous close monitoring is essential to better understand and mitigate natural hazards in high mountain environments under ongoing climate change.

References

Abermann, J., Fischer, A., Lambrecht, A., and Geist, T. (2010). On the potential of very high-resolution repeat DEMs in glacial and periglacial environments. *The Cryosphere*, 4(1):53–65.

Agliardi, F., Crosta, G., and Zanchi, A. (2001). Structural constraints on deep-seated slope deformation kinematics. *Engineering Geology*, 59(1):83–102.

Alexander Ruff (2015). Spatio-temporal quanti cation of geomorphological processes in the recently deglaciated area surrounding the Findelengletscher. Master's thesis, Zurich, Zurich.

Allen, S. and Huggel, C. (2013). Extremely warm temperatures as a potential cause of recent high mountain rockfall. *Global and Planetary Change*, 107:59–69.

Ambrosi, C. and Crosta, G. B. (2011). Valley shape influence on deformation mechanisms of rock slopes. In Jaboyedoff, M., editor, *Slope Tectonics*, volume 351, page 0. The Geological Society of London.

BAFU (2011). Hinweiskarte der potenziellen Permafrostverbreitung.

Bajni, G., Camera, C. A. S., and Apuani, T. (2021). Deciphering meteorological influencing factors for Alpine rockfalls: A case study in Aosta Valley. *Landslides*, 18(10):3279–3298.

Ballantyne, C. K. (2002). Paraglacial geomorphology. *Quaternary Science Reviews*, 21(18):1935–2017.

Bearth (1953). Geologischer Atlas der Schweiz 1:25'000.

Benn, Douglas and Evans, and JA, D. (2014). *Glaciers and Glaciation*. Routledge.

Bhuyan, K., Rana, K., Ferrer, J. V., Cotton, F., Ozturk, U., Catani, F., and Malik, N. (2024). Landslide topology uncovers failure movements. *Nature Communications*, 15(1):2633.

Bollmann, E., Sailer, R., Briese, C., Stötter, J., and Fritzmann, P. (2011). Potential of airborne laser scanning for geomorphologic feature and process detection and quantifications in high alpine mountains. *Zeitschrift für Geomorphologie, Supplementary Issues*, pages 83–104.

Bucher, K., Weisenberger, T. B., Weber, S., Klemm, O., and Corfu, F. (2020). The Theodul Glacier Unit, a slab of pre-Alpine rocks in the Alpine meta-ophiolite of Zermatt-Saas, Western Alps. *Swiss Journal of Geosciences*, 113(1):1.

Bundesamt für Landestopografie swisstopo (2024). swissALTI3D Das hoch aufgelöste Terrainmodell der Schweiz.

Bundesamt für Umwelt BAFU (2024). Geologischer Atlas der Schweiz 1:25'000 Pixel. https://www.swisstopo.admin.ch/de/geologischer-atlas-der-schweiz-1-25000-pixel.

Carrivick, J. L. and Heckmann, T. (2017). Short-term geomorphological evolution of proglacial systems. *Geomorphology*, 287:3–28.

Chandler, B. M. P., Lovell, H., Boston, C. M., Lukas, S., Barr, I. D., Benediktsson, Í. Ö., Benn, D. I., Clark, C. D., Darvill, C. M., Evans, D. J. A., Ewertowski, M. W., Loibl, D., Margold, M., Otto, J.-C., Roberts, D. H., Stokes, C. R., Storrar, R. D., and Stroeven, A. P. (2018). Glacial geomorphological mapping: A review of approaches and frameworks for best practice. *Earth-Science Reviews*, 185:806–846.

Christine Schärer (2018). Evolution of a moraine-breaching landslide in the recently deglaciated area of the Findelengletscher. Master's thesis, Zürich.

Church, M., Stock, R. F., and Ryder, J. M. (1979). Contemporary Sedimentary Environments on Baffin Island, N. W. T., Canada: Debris Slope Accumulations. *Arctic and Alpine Research*, 11(4):371–401.

Church, MICHAEL. and Ryder, J. M. (1972). Paraglacial Sedimentation: A Consideration of Fluvial Processes Conditioned by Glaciation. *GSA Bulletin*, 83(10):3059–3072.

Cossart, E. and Fort, M. (2008). Sediment release and storage in early deglaciated areas: Towards an application of the exhaustion model from the case of Massif des Écrins (French Alps) since the Little Ice Age. *Norsk Geografisk Tidsskrift - Norwegian Journal of Geography*, 62(2):115–131.

Cossart, E. E., Braucher, R., Fort, M., Bourles, D., and Carcaillet, J. (2007). The consequences of glacial debuttressing in deglaciated areas: Evidence from field data and cosmogenic datings. *Geomorphology*, 95(1-2):3–26.

Crosta, G. B., Frattini, P., and Agliardi, F. (2013). Deep seated gravitational slope deformations in the European Alps. *Tectonophysics*, 605:13–33.

Curry, A. M. (1999). Paraglacial modification of slope form. *Earth Surface Processes and Landforms*, 24(13):1213–1228.

D'Amato, J., Hantz, D., Guerin, A., Jaboyedoff, M., Baillet, L., and Mariscal, A. (2016). Influence of meteorological factors on rockfall occurrence in a middle mountain limestone cliff. *Natural Hazards and Earth System Sciences*, 16(3):719–735.

Daniel Farinotti, Matthias Huss, Mylène Jacquemart, Mauro Werder, Reto Knutti, Sonia Seneviratne, Robert Kenner, Jeanette Nötzli, Marcia Phillips, Olivier Glagliardini, and Thomas Schuler (2025). Fact sheet for the now-collapsed Birchgletscher, Switzerland. Birchgletscher Fact sheet, ETH.

Davies, M. C. R., Hamza, O., and Harris, C. (2001). The effect of rise in mean annual temperature on the stability of rock slopes containing ice-filled discontinuities. *Permafrost and Periglacial Processes*, 12(1):137–144.

Dewez, T., Nachbaur, A., Mathon, C., Sedan, O., Kobayashi, H., Rivière, C., Berger, F., and Garets, E. D. (2010). OFAI: 3D block tracking in a real-size rockfall experiment on a weathered volcanic rocks slope of Tahiti, French Polynesia.

Dikau, R., Eibisch, K., Eichel, J., Meßenzehl, K., and Schlummer-Held, M. (2019). *Geomorphologie*. Springer, Berlin, Heidelberg.

Dobinski, W. (2011). Permafrost. *Earth-Science Reviews*, 108(3):158–169.

Douglas I. Benn and David J.A. Evans (2010). *Glacier and Glacition*. Hodder Education.

Dussauge, C., Grasso, J.-R., and Helmstetter, A. (2003). Statistical analysis of rockfall volume distributions: Implications for rockfall dynamics. *Journal of Geophysical Research: Solid Earth*, 108(B6).

Esri (2025). Desktop GIS Software | Mapping Analytics | ArcGIS Pro. Esri.

Esri (2026a). Mosaic (Data Management)—ArcGIS Pro | Documentation. https://pro.arcgis.com/en/pro-app/3.4/tool-reference/data-management/mosaic.htm.

Esri (2026b). Resample (Data Management)—ArcGIS Pro | Documentation. https://pro.arcgis.com/en/pro-app/3.4/tool-reference/data-management/resample.htm.

Fischer, L., Amann, F., Moore, J. R., and Huggel, C. (2010). Assessment of periglacial slope stability for the 1988 Tschierva rock avalanche (Piz Morteratsch, Switzerland). *Engineering Geology*, 116(1):32–43.

Fischer, L. and Huggel, C. (2008). Methodical design for stability assessments of permafrost-affected high-mountain rock walls. In *9th International Conference on Permafrost*, pages 439–444.

Fischer, L., Kääb, A., Huggel, C., and Noetzli, J. (2006). Geology, glacier retreat and permafrost degradation as controlling factors of slope instabilities in a high-mountain rock wall: The Monte Rosa east face. *Natural Hazards and Earth System Sciences*, 6(5):761–772.

Florian Meyer (2025). What ETH Zurich glacier researchers know about the collapse of the Birch Glacier. https://ethz.ch/en/news-and-events/eth-news/news/2025/05/what-eth-glacier-researchers-know-about-the-collapse-of-the-birchgletscher-glacier.html.

French, H. M. (2017). *The Periglacial Environment*. John Wiley & Sons.

Fu, Z., Li, D.-Q., Wang, S., Zhang, L., and Du, W. (2024). Causes of episodic movement of the Baijiabao landslide based on multiple-time scale analysis. *Landslides*, 21(5):1069–1082.

Garankina, E. V., Lobkov, V. A., Shorkunov, I. G., and Belyaev, V. R. (2022). Identifying relict periglacial features in watershed landscape and deposits of Borisoglebsk Upland, Central European Russia. *Journal of the Geological Society*, 179(5):jgs2021–135.

Gärtner-Roer, I., Brunner, N., Delaloye, R., Haeberli, W., Kääb, A., and Thee, P. (2022). Glacier–permafrost relations in a high-mountain environment: 5 decades of kinematic monitoring at the Gruben site, Swiss Alps. *The Cryosphere*, 16(5):2083–2101.

Gautam, P., Kubota, T., Sapkota, L. M., and Shinohara, Y. (2021). Landslide susceptibility mapping with GIS in high mountain area of Nepal: A comparison of four methods. *Environmental Earth Sciences*, 80(9):359.

GLAMOS (2026). Schweizer Gletscher | Gletschermessnetz Schweiz GLAMOS. https://www.glamos.ch/.

Grämiger, L. M., Moore, J. R., Gischig, V. S., Ivy-Ochs, S., and Loew, S. (2017). Beyond debuttressing: Mechanics of paraglacial rock slope damage during repeat glacial cycles. *Journal of Geophysical Research: Earth Surface*, 122(4):1004–1036.

Grämiger, L. M., Moore, J. R., Gischig, V. S., Loew, S., Funk, M., and Limpach, P. (2020). Hydromechanical Rock Slope Damage During Late Pleistocene and Holocene Glacial Cycles in an Alpine Valley. *Journal of Geophysical Research: Earth Surface*, 125(8):e2019JF005494.

Gruber, S, Haeberli, W, Krummenacher, B., Keller, F, Mani, P., Hunziker, G., Hölzle, M., Vonder Mühll, D., Zimmermann, M., Keusen, H.-R., and Rätzo, H (2006). Erläuterungen zur Hinweiskarte der potentiellen Permafrostverbreitung in der Schweiz.

Haeberli, W., Hoelzle, M., Kääb, A., Keller, F., Vonder Mühll, D., and Wagner, S. (1998). Ten years after drilling through the permafrost of the active rock glacier murtèl, eastern swiss alps: answered questions and new perspectives. In *Proceedings of the Seventh International Conference on Permafrost*, volume 55. Université Laval, Québec Canada.

Hambrey, M. J. and Alean, J. C. (2016). *Colour Atlas of Glacial Phenomena*. CRC Press, Boca Raton.

Hasler, A., Gruber, S., and Beutel, J. (2012). Kinematics of steep bedrock permafrost. *Journal of Geophysical Research: Earth Surface*, 117(F1).

Hoek, E., Kaiser, P. K., and Bawden, W. F. (2000). *Support of Underground Excavations in Hard Rock*. CRC Press.

Höhle, J. and Höhle, M. (2009). Accuracy assessment of digital elevation models by means of robust statistical methods. *ISPRS Journal of Photogrammetry and Remote Sensing*, 64(4):398–406.

Hooke, R. (2011). J.G. Cogley and 10 others. 2011. Glossary of glacier mass balance and related terms. Prepared by the Working Group on Mass-balance Terminology and Methods of the International Association of Cryospheric Sciences (IACS). Paris, UNESCO–International Hydrological Programme. IACS. (IHP-VII Technical Documents in Hydrology No. 86, IACS Contribution No. 2.) 114pp., paperback. Available free from IHP Secretariat, UNESCO, Division of Water Sciences, 1 rue Miollis, 75732 Paris Cedex 15, France, or from ihp@unesco.org, and as free download from http://unesdoc.unesco.org/images/0019/001925/192525E.pdf. *Journal of Glaciology*, 57(206):1176–1176.

Hou, J., Zhang, P., Gao, N., Yan, W., and Yu, Q. (2025). Freeze–Thaw-Induced Degradation Mechanisms and Slope Stability of Filled Fractured Rock Masses in Cold Region Open-Pit Mines. *Applied Sciences*, 15(13):7429.

Hsieh, Y.-C., Chan, Y.-C., and Hu, J.-C. (2016). Digital Elevation Model Differencing and Error Estimation from Multiple Sources: A Case Study from the Meiyuan Shan Landslide in Taiwan. *Remote Sensing*, 8(3):199.

Huggel, C. (2015). *The High-Mountain Cryosphere*. Cambridge University Press.

Huggel, C., Clague, J. J., and Korup, O. (2012). Is climate change responsible for changing landslide activity in high mountains? *Earth Surface Processes and Landforms*, 37(1):77–91.

Huggel, C., Fischer, L., Schneider, D., and Haeberli, W. (2010). Research advances on climate-induced slope instability in glacier and permafrost high-mountain environments. *Geographica Helvetica*, 65(2):146–156.

Hugonnet, R., Brun, F., Berthier, E., Dehecq, A., Mannerfelt, E. S., Eckert, N., and Farinotti, D. (2022). Uncertainty Analysis of Digital Elevation Models by Spatial Inference From Stable Terrain. *IEEE Journal of Selected Topics in Applied Earth Observations and Remote Sensing*, 15:6456–6472.

Hungr, O., Leroueil, S., and Picarelli, L. (2014). The Varnes classification of landslide types, an update. *Landslides*, 11(2):167–194.

Huss, M., Bookhagen, B., Huggel, C., Jacobsen, D., Bradley, R., Clague, J., Vuille, M., Buytaert, W., Cayan, D., Greenwood, G., Mark, B., Milner, A., Weingartner, R., and Winder, M. (2017). Toward mountains without permanent snow and ice. *Earth's Future*, 5(5):418–435.

Institut für Schnee- und Lawinenforschung SLF (2025). Bergsturz, Steinschlag und Co.: FAQ und Dossier. https://www.slf.ch/de/naturgefahren/bergsturz-steinschlag-und-co-faq-und-dossier/.

International Permafrost Association (2026). What is Permafrost?

IPCC (2023). IPCC AR6: Climate Change 2023 —.

Kääb, A. (2002). Monitoring high-mountain terrain deformation from repeated air- and spaceborne optical data: Examples using digital aerial imagery and ASTER data. *ISPRS Journal of Photogrammetry and Remote Sensing*, 57(1):39–52.

Kenner, R., Noetzli, J., Hoelzle, M., Raetzo, H., and Phillips, M. (2019). Distinguishing ice-rich and ice-poor permafrost to map ground temperatures and ground ice occurrence in the Swiss Alps. *The Cryosphere*, 13(7):1925–1941.

Knight, J., Burningham, H., Griffiths, D., and Yao, Y. (2023). Coastal boulder movement on a rocky shoreline in northwest Ireland from repeat UAV surveys using Structure from Motion photogrammetry. *Geomorphology*, 440:108883.

Krautblatter, M., Funk, D., and Günzel, F. K. (2013). Why permafrost rocks become unstable: A rock–ice-mechanical model in time and space. *Earth Surface Processes and Landforms*, 38(8):876–887.

Kunz, J. and Kneisel, C. (2020). Glacier–Permafrost Interaction at a Thrust Moraine Complex in the Glacier Forefield Muragl, Swiss Alps. *Geosciences*, 10(6):205.

Laigle, D. and Bardou, E. (2022). Mass-Movement Types and Processes: Flow-Like Mass Movements, Debris Flows and Earth Flows. In Shroder, J. J. F., editor, *Treatise on Geomorphology 2nd Edition*, volume 5 of *Mass-Movement Geomorphology*, pages 61–84. Elsevier.

Langston, G., Bentley, L. R., Hayashi, M., McClymont, A., and Pidlisecky, A. (2011). Internal structure and hydrological functions of an alpine proglacial moraine. *Hydrological Processes*, 25(19):2967–2982.

Leica Geosystems AG (2025). Leica ADS100 Airborne Digital Sensor. https://leica-geosystems.com/de-ch/products/airborne-systems/imaging-sensors/leica-ads100-airborne-digital-sensor.

Leigh, C. L., Kidner, D. B., and Thomas, M. C. (2009). The Use of LiDAR in Digital Surface Modelling: Issues and Errors. *Transactions in GIS*, 13(4):345–361.

Linsbauer, A., Huss, M., Hodel, E., Bauder, A., and Barandun, M. (2025). Vanished glaciers of the Swiss Alps: An inventory-based assessment from 1973 to 2016. *Annals of Glaciology*, 66:e33.

Lukas, S., Graf, A., Coray, S., and Schlüchter, C. (2012). Genesis, stability and preservation potential of large lateral moraines of Alpine valley glaciers – towards a unifying theory based on Findelengletscher, Switzerland. *Quaternary Science Reviews*, 38:27–48.

Ma, J., Song, C., and Wang, Y. (2021). Spatially and Temporally Resolved Monitoring of Glacial Lake Changes in Alps During the Recent Two Decades. *Frontiers in Earth Science*, 9.

Martin Wild, Atsumu Ohmura, and Knut Makowski (2007). Impact of global dimming and brightening on global warming. https://agupubs.onlinelibrary.wiley.com/doi/full/10.1029/2006GL028031.

Masi, E. B., Segoni, S., and Tofani, V. (2021). Root Reinforcement in Slope Stability Models: A Review. *Geosciences*, 11(5):212.

Matsuoka, N. (2001). Solifluction rates, processes and landforms: A global review. *Earth-Science Reviews*, 55(1):107–134.

Matsuoka, N. and Murton, J. (2008). Frost weathering: Recent advances and future directions. *Permafrost and Periglacial Processes*, 19(2):195–210.

McColl, S., Davies, T., and McSaveney, M. (2010). Glacier retreat and rock-slope stability: Debunking debuttressing. *Geologically Active*, pages 467–474.

McColl, S. T. (2012). Paraglacial rock-slope stability. *Geomorphology*, 153–154:1–16.

McColl, S. T. and Draebing, D. (2019). Rock Slope Instability in the Proglacial Zone: State of the Art. In Heckmann, T. and Morche, D., editors, *Geomorphology of Proglacial Systems: Landform and Sediment Dynamics in Recently Deglaciated Alpine Landscapes*, pages 119–141. Springer International Publishing, Cham.

Mélanie Raymond, Matthias Wegmann, and Martin Funk (2003). lnventar gefãhrlicher Gletscher in der Schweiz.

MeteoSchweiz (2017). Klimabulletin Sommer 2017 - MeteoSchweiz. https://www.meteoschweiz.admin.ch/service-und-publikationen/publikationen/berichte-und-bulletins/2017/klimabulletin-sommer-2017.html.

MeteoSchweiz (2018). Klimabulletin Sommer 2018 - MeteoSchweiz. https://www.meteoschweiz.admin.ch/service-und-publikationen/publikationen/berichte-und-bulletins/2018/klimabulletin-sommer-2018.html.

MeteoSchweiz (2024). Klimabulletin Sommer 2024 - MeteoSchweiz. https://www.meteoschweiz.admin.ch/service-und-publikationen/publikationen/berichte-und-bulletins/2024/klimabulletin-sommer-2024.html.

MeteoSchweiz (2026). Automatische Niederschlagsstationen.

Michael Keller (2021). AI provides debris flow warnings. https://ethz.ch/en/news-and-events/eth-news/news/2021/03/ai-provides-debris-flow-warnings.html.

Mihail E. Popescu (2002). LANDSLIDE CAUSAL FACTORS AND LANDSLIDE REMEDIATIAL OPTIONS. *Illinois Institute of Technology, Chicago, USA*.

Miro (2025). Miro: Flowchart-Tool. https://miro.com/aq/paid-search/de/flowchart-tool.

Mölg, N., Huggel, C., Herold, T., Storck, F., Allen, S., Haeberli, W., Schaub, Y., and Odermatt, D. (2021). Inventory and evolution of glacial lakes since the Little Ice Age: Lessons from the case of Switzerland. *Earth Surface Processes and Landforms*, 46(13):2551–2564.

Noetzli, J. and Phillips, M. (2019). Mountain permafrost hydrology. *Hydro-CH2018 Project. Comissioned by the Federal Office for the Environment (FOEN), Bern, Switzerland*, 18.

Notti, D., Wrzesniak, A., Dematteis, N., Lollino, P., Fazio, N. L., Zucca, F., and Giordan, D. (2021). A multidisciplinary investigation of deep-seated landslide reactivation triggered by an extreme rainfall event: A case study of the Monesi di Mendatica landslide, Ligurian Alps. *Landslides*, 18(7):2341–2365.

Nuth, C. and Kääb, A. (2011). Co-registration and bias corrections of satellite elevation data sets for quantifying glacier thickness change. *The Cryosphere*, 5(1):271–290.

Oliva, M., Gómez-Ortiz, A., Palacios, D., Franch, F. S., Ramos, M., de Sanjosé-Blasco, J. J., Fernandes, M., Fernández-Fernández, J. M., Galindo-Zaldívar, J., García-Oteyza, J., González, L., Hauck, C., Martín-Díaz, J., Nofre, J., de Galdeano, C. S., and Tanarro-García, L. M. (2022). Ancient and Present-Day Periglacial Environments in the Sierra Nevada. In Zamora, R. and Oliva, M., editors, *The Landscape of the Sierra Nevada: A Unique Laboratory of Global Processes in Spain*, pages 115–128. Springer International Publishing, Cham.

Pánek, T. and Klimeš, J. (2016). Temporal behavior of deep-seated gravitational slope deformations: A review. *Earth-Science Reviews*, 156:14–38.

Pepin, N. C., Arnone, E., Gobiet, A., Haslinger, K., Kotlarski, S., Notarnicola, C., Palazzi, E., Seibert, P., Serafin, S., Schöner, W., Terzago, S., Thornton, J. M., Vuille, M., and Adler, C. (2022). Climate Changes and Their Elevational Patterns in the Mountains of the World. *Reviews of Geophysics*, 60(1):e2020RG000730.

PERMOS (2026). PERMOS Publikationen. https://www.permos.ch/de/.

Peter Höllrigl (2018). Bergsturz in Bondo - Was geschah am Piz Cengalo wirklich? https://www.srf.ch/wissen/natur-tiere/bergsturz-in-bondo-was-geschah-am-piz-cengalo-wirklich.

QGIS (2025). QGIS resources · QGIS Web Site. QGIS.

Rapp, A. (1960). Recent Development of Mountain Slopes in Kärkevagge and Surroundings, Northern Scandinavia. *Geografiska Annaler*, 42(2-3):65–200.

Ravanel, L. and Deline, P. (2011). Climate influence on rockfalls in high-Alpine steep rockwalls: The north side of the Aiguilles de Chamonix (Mont Blanc massif) since the end of the 'Little Ice Age'. *The Holocene*, 21(2):357–365.

Robert Kenner (2019). Permafrost- und Bodeneiskarte. https://www.slf.ch/de/services-und-produkte/permafrost-und-bodeneiskarte/.

Romain Hugonnet, Erik Mannerfelt, and Amaury Dehecq (2020). xDEM. https://xdem.readthedocs.io/en/stable/mission.html.

RStudio (2025). RStudio Desktop. Posit Software, PBC.

Scheffler, D., Hollstein, A., Diedrich, H., Segl, K., and Hostert, P. (2017). AROSICS: An Automated and Robust Open-Source Image Co-Registration Software for Multi-Sensor Satellite Data. *Remote Sensing*, 9(7):676.

Schiefer, E., Menounos, B., and Wheate, R. (2007). Recent volume loss of British Columbian glaciers, Canada. *Geophysical Research Letters*, 34(16).

Schumann, K., Gewolf, S., and Tackenberg, O. (2016). Factors affecting primary succession of glacier foreland vegetation in the European Alps. *Alpine Botany*, 126(2):105–117.

Shanmugam, G. and Wang, Y. (2015). The landslide problem. *Journal of Palaeogeography*, 4(2):109–166.

Shoab, M., Singh, V. K., and Ravibabu, M. V. (2022). High-Precise True Digital Orthoimage Generation and Accuracy Assessment based on UAV Images. *Journal of the Indian Society of Remote Sensing*, 50(4):613–622.

Shroder, J. (2013). *Treatise on Geomorphology*. Number Bd. 1-14. Elsevier Science.

SLF (2026). Schneehöhe | Schneekarten | White Risk.

Sousa, R., Jr, E., Chaminé, H., Sousa, L., and Karam, K. (2021). Risk assessment on landslides focused on the role of the water: Examples from model regions (Rio de Janeiro State and Hong Kong). *SN Applied Sciences*, 3:423.

Spyder Project Contributors (2009). Spyder: The Scientific Python Development Environment.

Stead, D. and Wolter, A. (2015). A critical review of rock slope failure mechanisms: The importance of structural geology. *Journal of Structural Geology*, 74:1–23.

Stoffel, M., Trappmann, D. G., Coullie, M. I., Ballesteros Cánovas, J. A., and Corona, C. (2024). Rockfall from an increasingly unstable mountain slope driven by climate warming. *Nature Geoscience*, 17(3):249–254.

swisstopo (2026). Karten der Schweiz - Schweizerische Eidgenossenschaft - map.geo.admin.ch. https://map.geo.admin.ch.

Tan, W., Li, Z., Li, Z., Sothy, E., Wu, S., and Guo, Q. (2025). Analysis of the Variation Characteristics of Rock Mechanical Parameters and Slope Stability Under Freeze-Thaw Cycles. *Applied Sciences*, 15(11):5898.

Taylor, C., Robinson, T. R., Dunning, S., Rachel Carr, J., and Westoby, M. (2023). Glacial lake outburst floods threaten millions globally. *Nature Communications*, 14(1):487.

Terzaghi, K., Robert F. Baker, and E. J. Yoder (1958). *Stability Analyses and Design of Control Methods*. Special Report. Highway Research Board.

U.S. Geological Survey (2021). What is a glacier? https://www.usgs.gov/faqs/what-a-glacier.

Van Niel, T. G., McVicar, T. R., Li, L., Gallant, J. C., and Yang, Q. (2008). The impact of misregistration on SRTM and DEM image differences. *Remote Sensing of Environment*, 112(5):2430–2442.

Varnes, D. (1978). SLOPE MOVEMENT TYPES AND PROCESSES. *Transportation Research Board Special Report*.

Vieira, G., Mora, C., and Faleh, A. (2017). New observations indicate the possible presence of permafrost in North Africa (Djebel Toubkal, High Atlas, Morocco). *The Cryosphere*, 11(4):1691–1705.

Walter, F., Amann, F., Kos, A., Kenner, R., Phillips, M., de Preux, A., Huss, M., Tognacca, C., Clinton, J., Diehl, T., and Bonanomi, Y. (2020). Direct observations of a three million cubic meter rock-slope collapse with almost immediate initiation of ensuing debris flows. *Geomorphology*, 351:106933.

WGMS (2025). World glacier monitoring service.

Windnagel, A., Hock, R., Maussion, F., Paul, F., Rastner, P., Raup, B., and Zemp, M. (2023). Which glaciers are the largest in the world? *Journal of Glaciology*, 69(274):301–310.

Yamamoto, N., Ishii, Y., Hirata, R., Tetsuka, S., and Yamada, T. (2023). Monitored transition from sagging to sliding during deep-seated gravitational slope deformation, Akatani-nishi, Japan. *Landslides*, 20(10):2243–2255.

Yan, M., Blaschke, T., Tang, H., Xiao, C., Sun, X., Zhang, D., and Fu, K. (2017). Using object-based analysis to derive surface complexity information for improved filtering of airborne laser scanning data. *Frontiers of Earth Science*, 11(1):11–19.

Yan, W. Y. (2023). Airborne Lidar Data Artifacts: What we know thus far. *IEEE Geoscience and Remote Sensing Magazine*, 11(3):21–45.

Yan, W. Y. and Shaker, A. (2018). Airborne LiDAR intensity banding: Cause and solution. *ISPRS Journal of Photogrammetry and Remote Sensing*, 142:301–310.

Yang, Y.-E. and Yu, T.-T. (2025). Volumetric estimation of landslide-induced terrain change using conditional GAN with multi-temporal DEMs and satellite imagery. *International Journal of Applied Earth Observation and Geoinformation*, 144:104864.

Zekollari, H., Huss, M., and Farinotti, D. (2019). Modelling the future evolution of glaciers in the European Alps under the EURO-CORDEX RCM ensemble. *The Cryosphere*, 13(4):1125–1146.

Zemp, M., Jakob, L., Dussaillant, I., Nussbaumer, S. U., Gourmelen, N., Dubber, S., A, G., Abdullahi, S., Andreassen, L. M., Berthier, E., Bhattacharya, A., Blazquez, A., Boehm Vock, L. F., Bolch, T., Box, J., Braun, M. H., Brun, F., Cicero, E., Colgan, W., Eckert, N., Farinotti, D., Florentine, C., Floricioiu, D., Gardner, A., Harig, C., Hassan, J., Hugonnet, R., Huss, M., Jóhannesson, T., Liang, C.-C. A., Ke, C.-Q., Khan, S. A., King, O., Kneib, M., Krieger, L., Maussion, F., Mattea, E., McNabb, R., Menounos, B., Miles, E., Moholdt, G., Nilsson, J., Pálsson, F., Pfeffer, J., Piermattei, L., Plummer, S., Richter, A., Sasgen, I., Schuster, L., Seehaus, T., Shen, X., Sommer, C., Sutterley, T., Treichler, D., Velicogna, I., Wouters, B., Zekollari, H., Zheng, W., and The GlaMBIE Team (2025). Community estimate of global glacier mass changes from 2000 to 2023. *Nature*, 639(8054):382–388.

Zhou, B., Zhang, Y., Wei, S., Wang, Z., Zhu, W., and Xue, Z. (2022). Slope Instability Analysis in Permafrost Regions by Shear Strength Parameters and Numerical Simulation. *Sustainability*, 14(15):9401.

Appendix

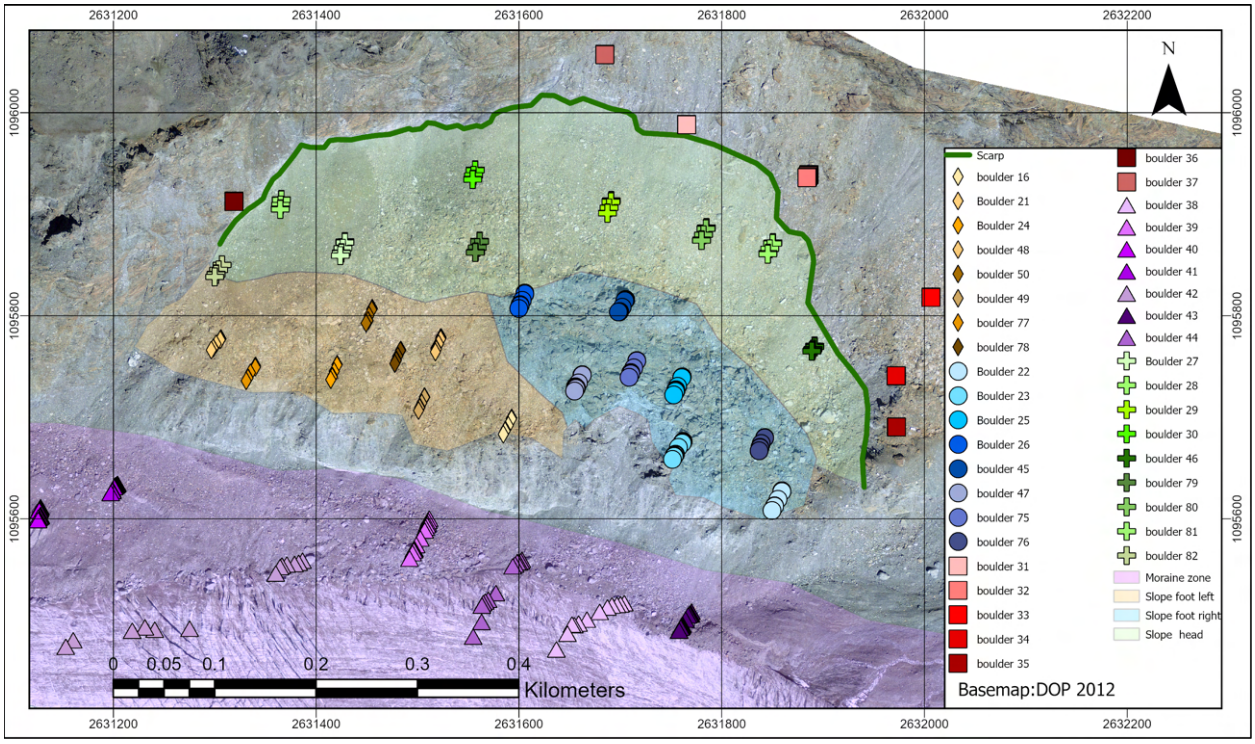

Figure 7.1: All picked boulders at the IR slope. Boulder symbols represent the slope topology.

Table 7.1: Overview of auxiliary datasets used in this study

ID	Variable	Product	Source	Reference
1	Permafrost	Raster	map.geo.admin.ch	(BAFU, 2011)
2	Precipitation	CSV	opendata.swiss	(MeteoSchweiz, 2026)
3	Temperature	CSV	opendata.swiss	(MeteoSchweiz, 2026)
4	Geology	Vector	geocat.ch	(Bundesamt für Umwelt BAFU, 2024)
5	Glacier changes	Excel	WGMS	(WGMS, 2025)
6	Glacier extent	Images	map.geo.admin	(Bundesamt für Landestopografie swisstopo, 2024)

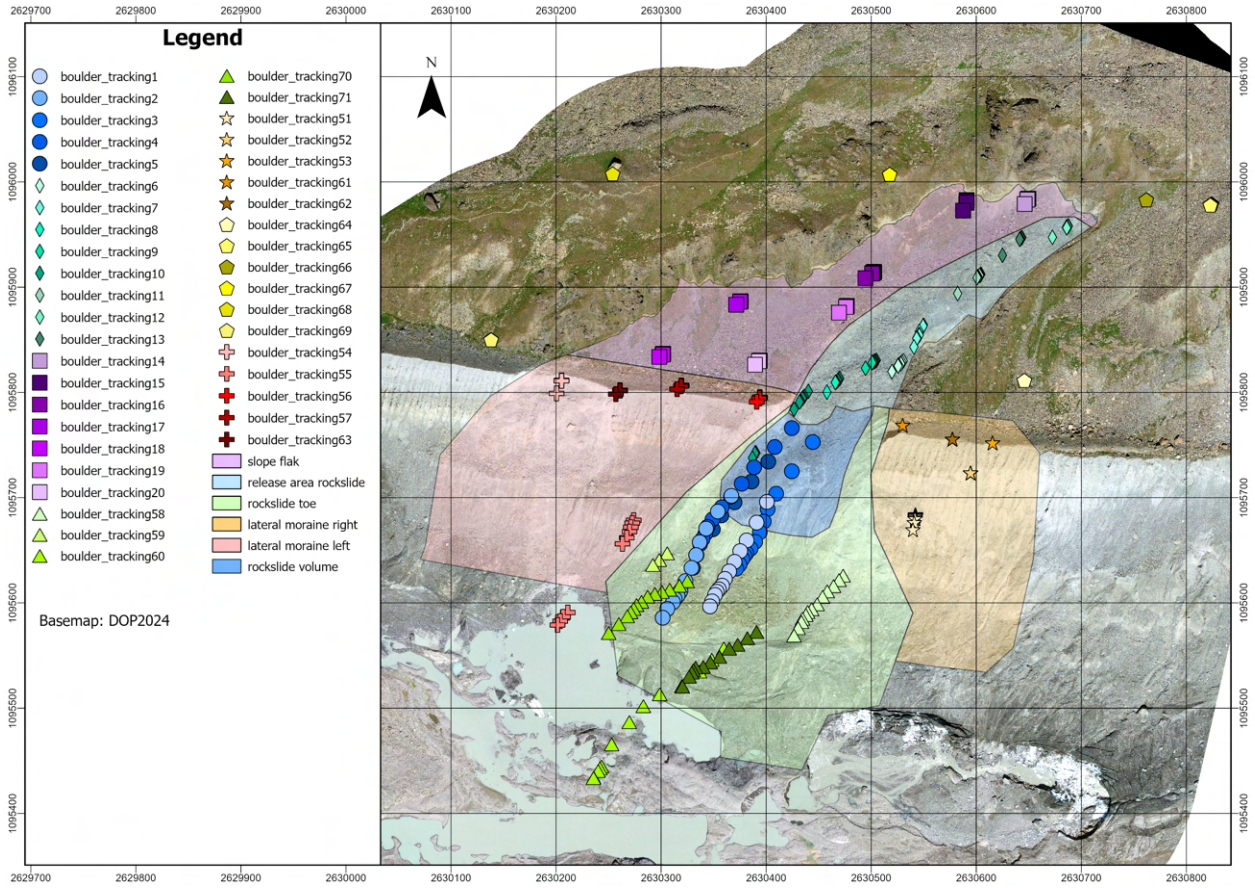

Figure 7.2: All picked boulders at the Tripfen slope. Boulder symbols represent the slope topology.

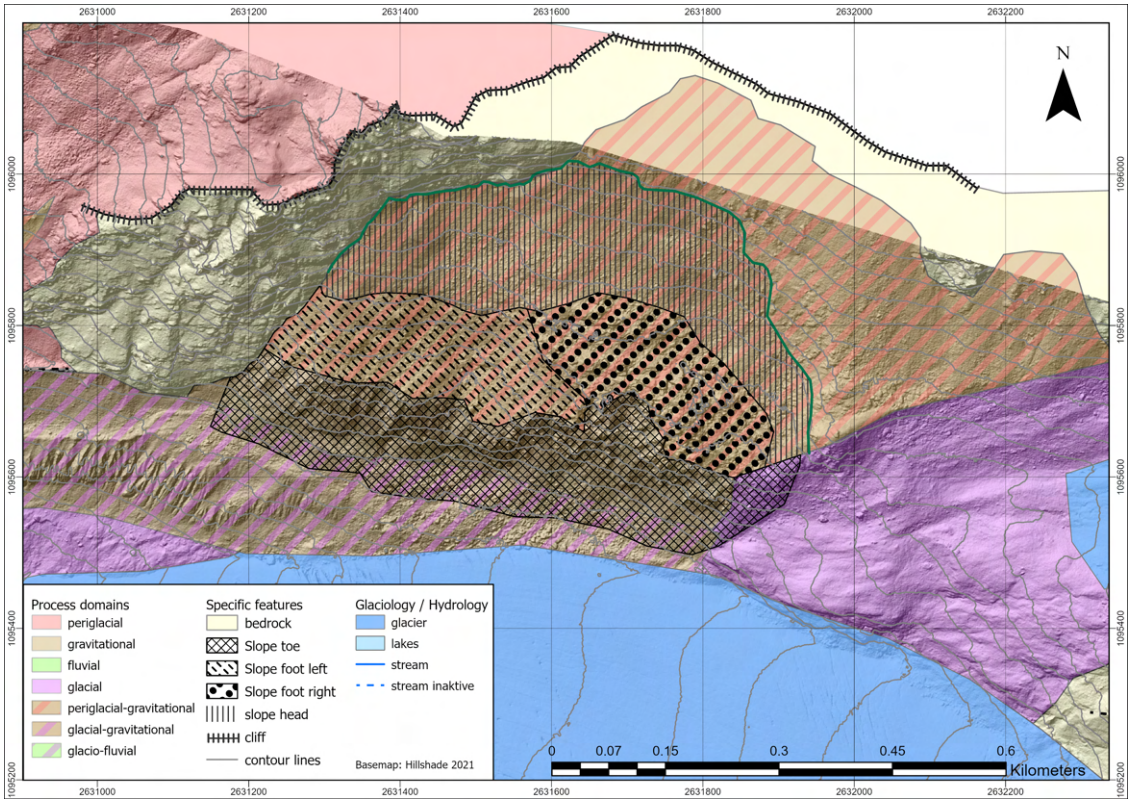

Figure 7.3: Innere Rimpfischwäng slope topology and the underlying process domains.

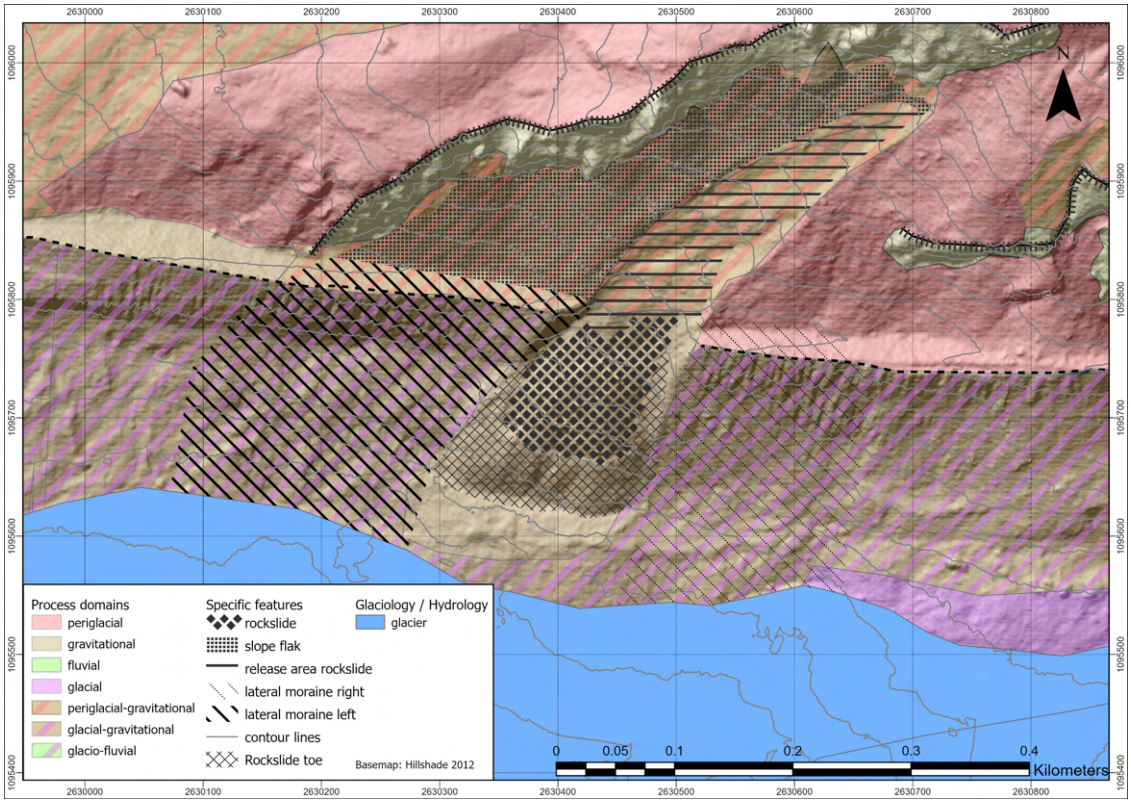

Figure 7.4: Tripfen slope topology and the underlying process domains.

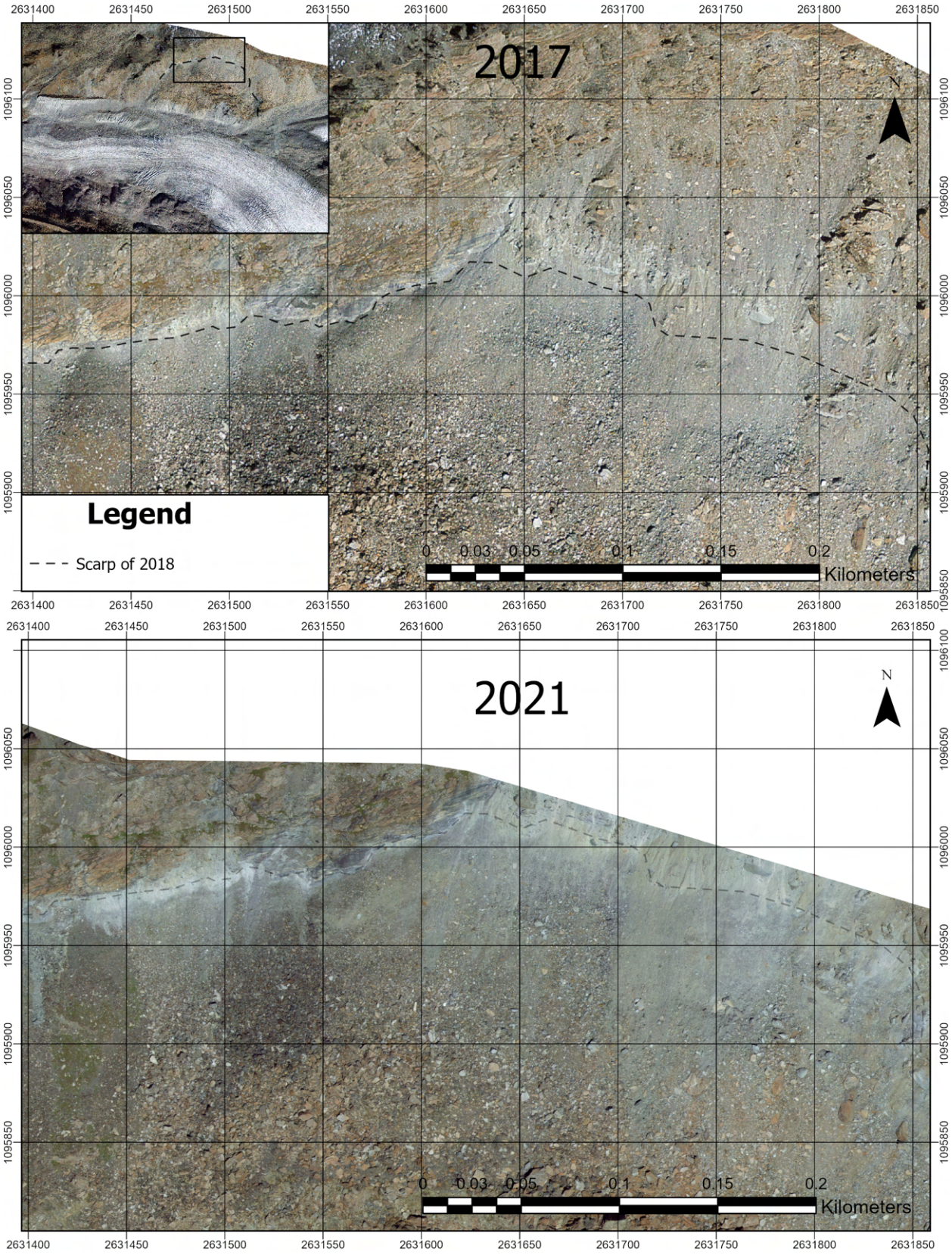

Figure 7.5: The main scarp filled with material in later years.

Year Pair	Depletion of material (m^3)	Accumulation material (m^3)
2012–2013	22’064	10’941
2013–2014	8’056	27’644
2014–2015	62’205	8’017
2015–2016	21’714	44’745
2016–2017	13’338	47’503
2017–2019	855’843	273’384
2019–2020	41’296	9’300
2020–2021	25’287	6’126

Table 7.2: Depletion and Accumulation of material in the unstable Area at IR slope. Material transported outside the area is not captured in the Accumulation material.

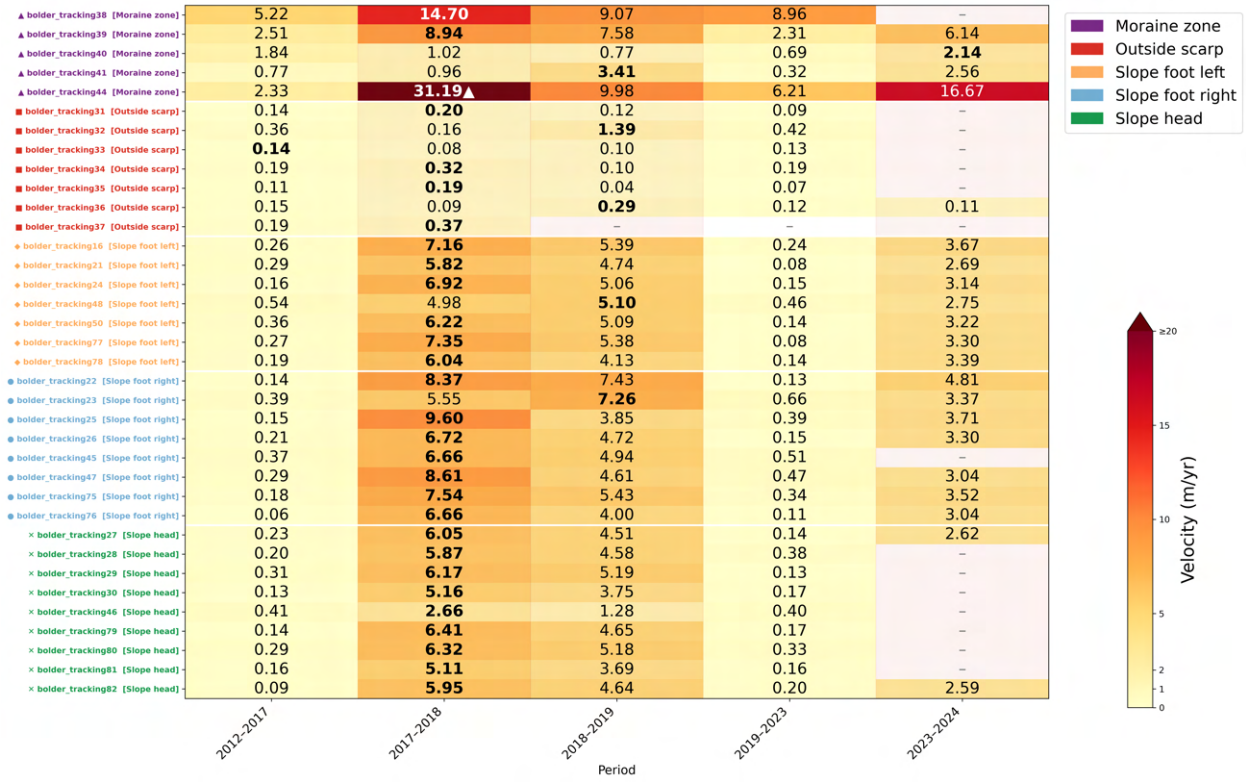

Figure 7.6: Velocity heatmap of each boulder picked at IR slope

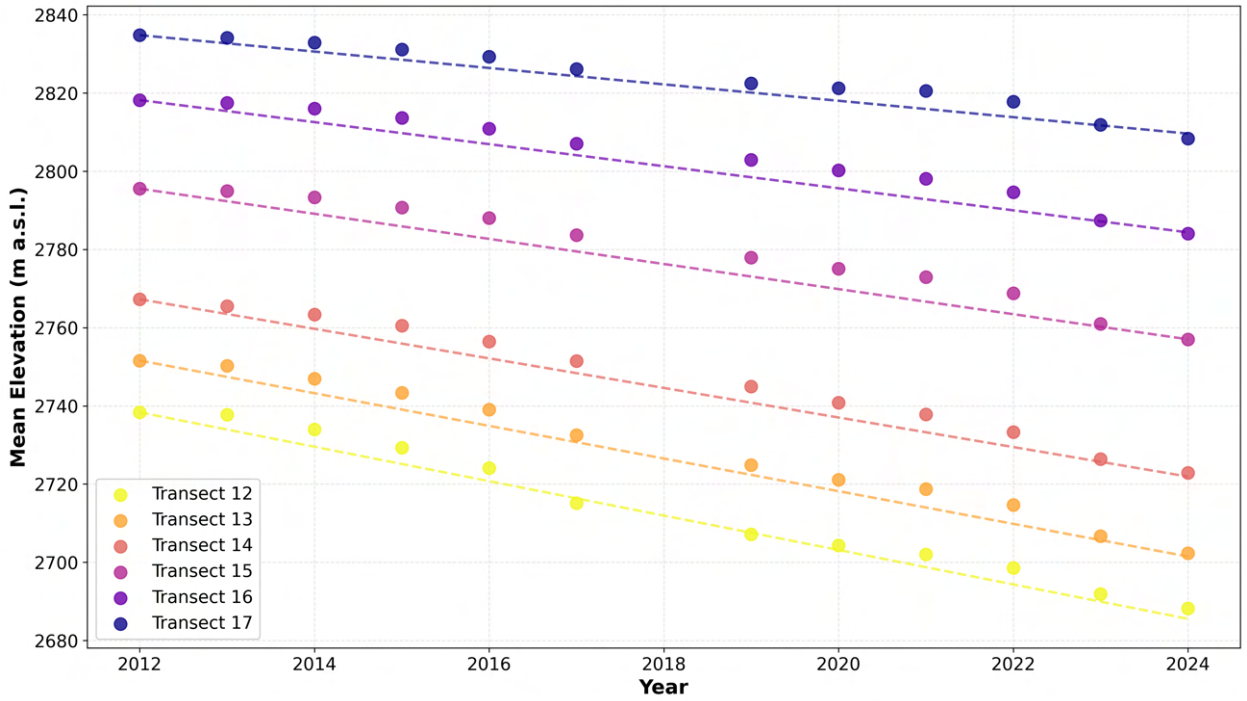

Figure 7.7: Mean elevation at each year for transect 12-17. The elevation represents only the mean elevation from the transect from 200 to 400 meters.

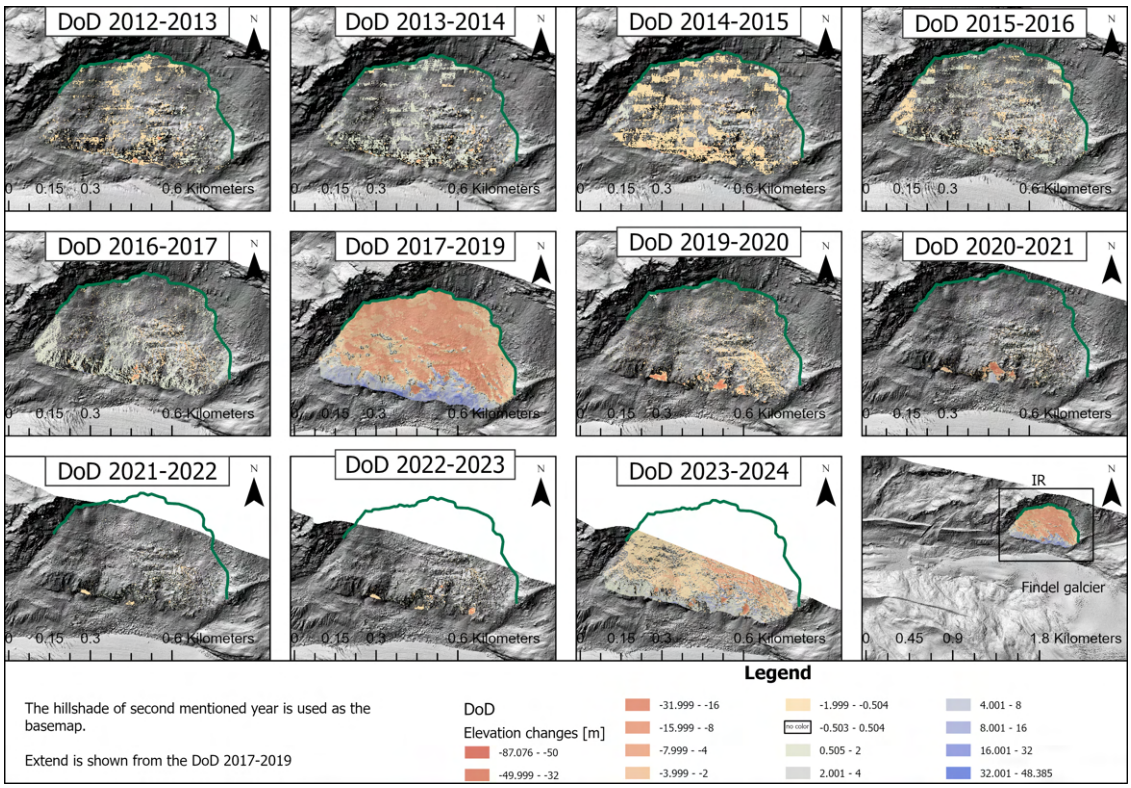

Figure 7.8: All DoD at IR over the study periode 2012–2024.

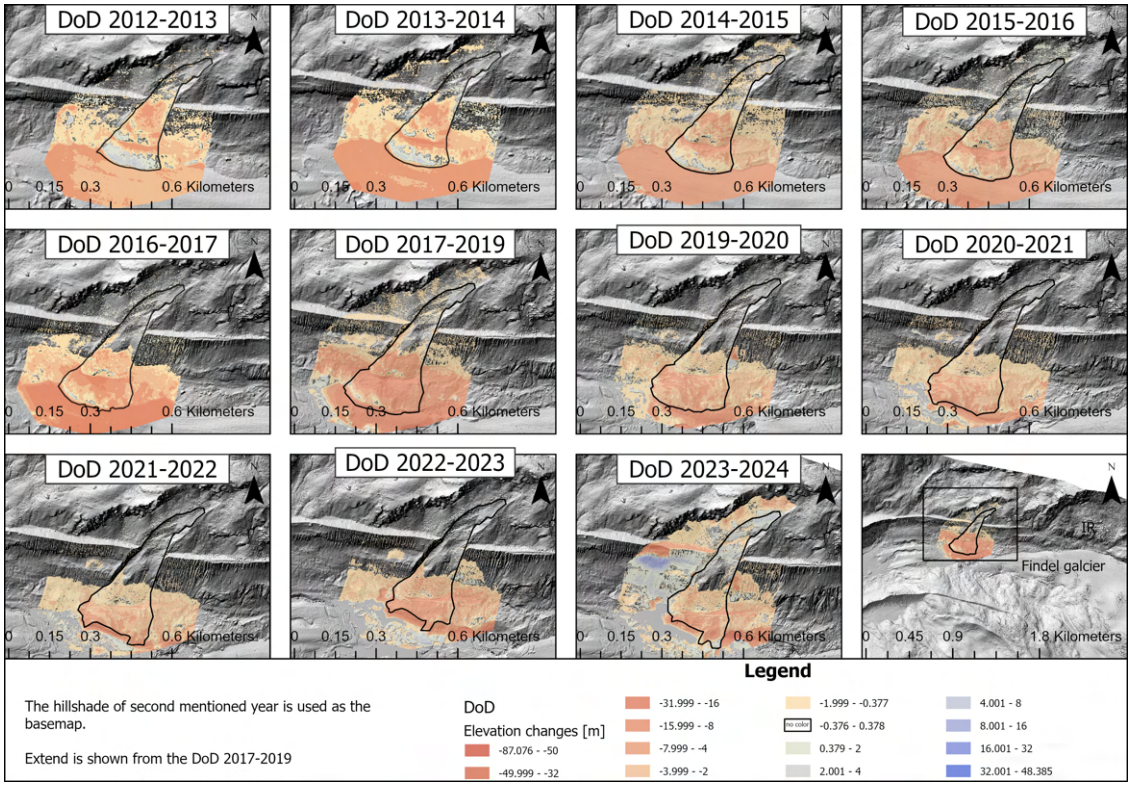

Figure 7.9: All DoD at Tripfen over the study period 2012–2024.

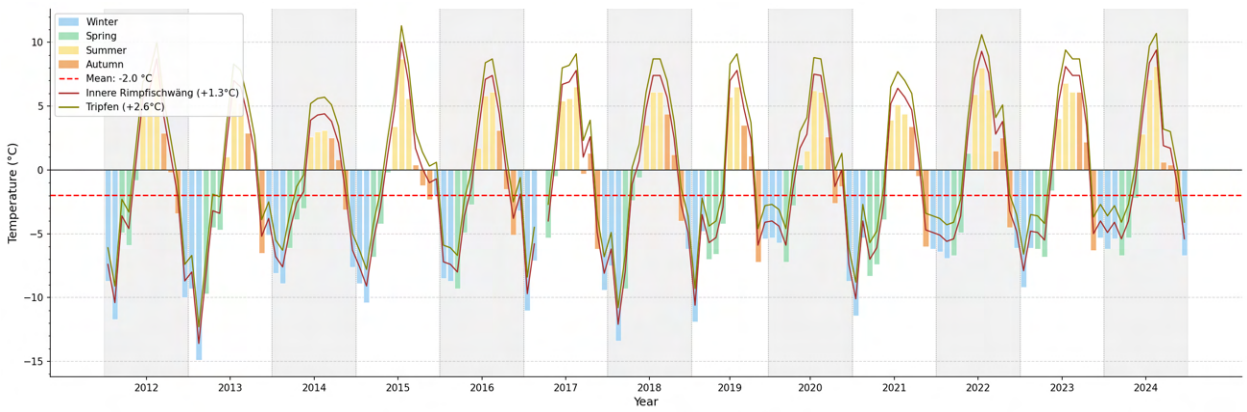

Figure 7.10: Monthly temperature at Gronergrad from 2012–2024 and estimate correction for the study sites.

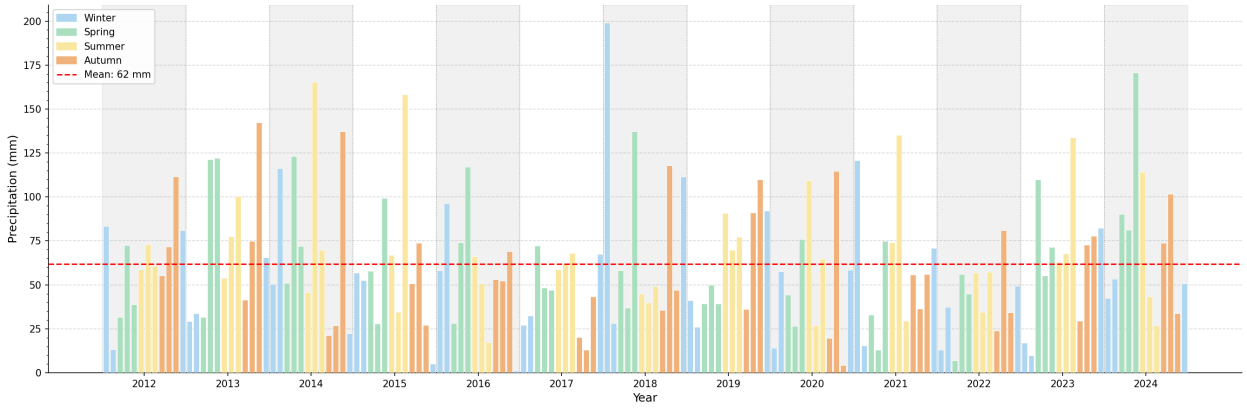

Figure 7.11: Precipitation over the study period at the Findelbach 2012–2024

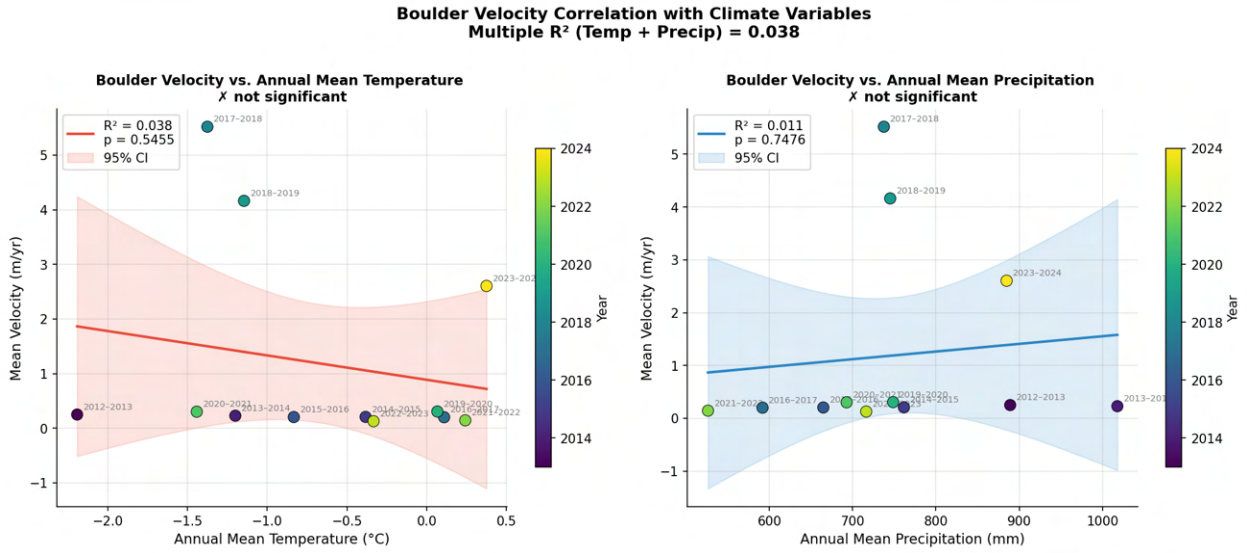

Figure 7.12: Correlation between velocity and Temperature and Precipitation



Figure 7.13: The green lines indicate wet areas (darker) where water is presumably pressing through the moraine from the river and tiny lakes at the same elevation on the other side of the moraine, at Findelengletscher (VS), Switzerland (Alexander Ruff, 2015)

Personal declaration

For this thesis, different artificial intelligence tools were used to assist during the code and writing phase. Claude AI (Sonnet 4.5) was use for coding, correct grammar and readability of sentences and sections (coherence and clarity of the text). DeepL and Grammarly were additionally used for grammar corrections. Overall, it did not affect the originality, technical content, or scientific contributions. This LaTeX template was created by authors Sophia Schlosser and Laurence Brandenberger. Which is freely available with the name IPZ Thesis Template (last updated December 2025).

I declare that the submitted thesis is written and created by me as independent work. All data and findings of other authors are cited and acknowledged in this thesis.

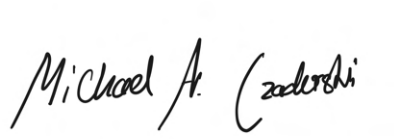

Zürich, 15.6.2026, Michael A. Czaderski-Forchmann